# Inhomogeneous Colloidal Mixtures: Segregation by Charge or Shape

Inaugural–Dissertation
zur
Erlangung des Doktorgrades der
Mathematisch-Naturwissenschaftlichen Fakultät
der Heinrich-Heine-Universität Düsseldorf

vorgelegt von

ANSGAR ESZTERMANN

aus Düsseldorf

Düsseldorf, Juni 2005

Gedruckt mit Genehmigung der
Mathematisch-Naturwissenschaftlichen Fakultät
der Heinrich-Heine-Universität Düsseldorf

Referent: Prof. Dr. H. Löwen
Koreferent: HS-Doz. Dr. M. Schmidt

Tag der mündlichen Prüfung: 30. Juni 2005

## Zusammenfassung

Die Erforschung von Kolloiden bietet ein weites Betätigungsfeld. Die vorliegende Arbeit konzentriert sich dabei auf zwei Aspekte der theoretischen Beschreibung mesoskopischer Teilchen. Zum einen werden ladungsstabilisierte Kolloide, die durch die sehr große Reichweite der Coulomb-Wechselwirkung charakterisiert sind, betrachtet. Auf der anderen Seite bietet das Modell der harten Wechselwirkung, bei dem die Teilchen nur bei Kontakt Kräfte aufeinander ausüben, Einsichten in die Auswirkungen sehr kurzreichweitiger Wechselwirkungen.

In Teil 1 der Arbeit wird das Verhalten geladener Teilchen in einem externen Feld untersucht. Dabei kommen sowohl Monte-Carlo-Computersimulationen als auch Poisson-Boltzmann-Theorie zum Einsatz. Zunächst wird eine binäre Kolloidmischung im Schwerefeld betrachtet. Dabei stellt sich heraus, daß die entscheidende Größe für die Dichteprofile nicht allein die Teilchenmasse, sondern das Verhältnis von Masse und Ladung ist. Das bedeutet, daß die Spezies mit niedrigerem Masse-Ladungsverhältnis auch dann oberhalb der anderen Komponente sedimentiert, wenn ihre Masse die größere ist.

Weiter wird ein Elektrolyt in einem Kondensator betrachtet. Das äußere elektrische Feld kann dabei zur Ladungstrennung im Elektrolyten führen, der seinerseits ein Feld aufbaut. Das Zusammenwirken der Felder führt zu einem Übergang zwischen einem delokalisierten und einem lokalisierten Zustand: ist die anliegende Spannung $U$ niedrig, verteilen sich die Ionen im gesamten System. Steigt $U$ über einen kritischen Wert $U_\mathrm{c}$, so konzentrieren sich die Ionen in der Nähe der Kondensatorplatten. Der mittlere Abstand $\langle h \rangle$ einer Ionenspezies von der entgegengesetzt geladenen Platte divergiert dabei mit $\langle h \rangle \sim \ln(U - U_\mathrm{c})/U_\mathrm{c}$.

In Teil 2 der Arbeit wird eine Dichtefunktionaltheorie für harte Teilchen vorgestellt. Dabei werden zum einen dreikomponentige Mischungen von Kugeln, Stäbchen und Plättchen im Grenzfall verschwindender Dicke von Stäbchen und Plättchen untersucht. Für den Überlapp von Kugeln und Plättchen wird zudem der Zusammenhang mit zweidimensionalen harten Scheiben aufgezeigt. Darüberhinaus werden binäre Mischungen von Kugeln und Stäbchen im sogenannten Onsager-Limes betrachtet. In diesem Grenzfall werden Terme erster Ordnung im Stäbchendurchmesser $D$ ebenfalls berücksichtigt. Experimentelle Systeme werden so insbesondere bei hoher Packungsdichte besser beschrieben. Um Anwendungen der Theorie zu erleichtern, wird das Funktional für einige einfache Geometrien explizit angegeben.

## Abstract

Out of the broad field of research that colloids provide, this thesis focuses on two aspects of the theoretical description of mesoscopic particles. On the one hand, charge-stabilised colloids are characterised by the very long range of the Coulomb interaction. On the other hand, the model of hard bodies provides insight into the effects of very short-ranged interactions: interparticle forces are exerted only upon contact.

In Part 1 of this thesis, the behaviour of charged particles under an external field is examined using both Monte-Carlo computer simulations and Poisson-Boltzmann theory. For a binary colloidal mixture in a gravitational field, it turns out that sedimentation is controlled by the ratio of particle mass to charge rather than by mass alone. Thus, the species with the lower mass-per-charge ratio will sediment on top, even if its mass is larger than that of the other species.

The ion distribution of an electrolyte between capacitor plates is influenced strongly by the external electric field. The non-uniform ion distribution, in turn, generates an electric field internal to the system. The interplay between these fields leads to a transition from a delocalised to a localised state: as long as the voltage $U$ applied across the capacitor remains low, the ions are distributed throughout the system. When $U$ rises above a certain threshold value $U_\mathrm{c}$, the ions become localised next to the capacitor plates. The average distance $\langle h \rangle$ of one species of ions from the oppositely charged capacitor plate diverges logarithmically as $\langle h \rangle \propto \ln(U - U_\mathrm{c})/U_\mathrm{c}$.

In Part 2 of this thesis, a density functional theory for hard bodies is presented. In particular, ternary mixtures of spheres, and rods and platelets of vanishing thickness, are examined. For the overlap of spheres and platelets, the relationship to two-dimensional hard disks is explained. Binary mixtures of rods and spheres in the Onsager limit are also considered. In this limit, terms that are linear in the needle thickness $D$ are included in the functional. This allows for a more accurate description of experimental systems – which are necessarily characterised by a finite $D$ – at high packing fractions. The theory follows Rosenfeld's hard-sphere density functional theory and generalises it to anisotropic particles. In order to facilitate applications, explicit expressions of the functional for simple geometries are given.

# Contents

CHAPTER 1

# Introduction

In an 1861 publication, Thomas Graham noted that some substances like starch and gelatine diffuse much more slowly than substances such as salt or sugar do. Taking the Greek translation of gelatine, *κόλλα*, he named this class of substances *colloids* [1]. Far from being an academic curiosity, colloids are very common in everyday life. Ink and paint are colloidal dispersions of pigments in water or oil; in homogenised milk [2], fat is dispersed in water. Human blood is also a colloid consisting mainly of red blood cells dispersed in blood plasma [3].

Colloidal particles range in size from the nanometre to the micrometre scale. Thus, they are significantly larger than atoms but much smaller than any objects that can be seen by the unaided eye. Therefore, they are referred to as *mesoscopic* particles. On the one hand, mesoscopic particles are small enough to exhibit collective behaviour similar to that found in atomic systems. Separation into liquid, vapour and solid phases with different lattice structures (e.g. face-centered cubic and body-centered cubic) are all known to exist in colloids. However, colloidal particles are also large enough so that their collective behaviour differs in many aspects from that of atoms and micro-molecules. For example, dynamics in colloids is slower than in atomic systems; it was their slow diffusion that prompted Graham [1] to define colloids as a separate class of matter. Another characteristic that separates colloids from atomic systems is their softness: While a substantial force is required to bend a metal bar, colloids can be deformed much more easily – to the delight of every child who has ever eaten jelly. It is important to notice that this softness is the result of collective behaviour; deformation of the individual particles is not necessarily easy. The difference in particle sizes (and, therefore, mass) between atoms and colloidal particles becomes directly apparent when the influence of gravity on different systems is observed. While macroscopic particles (such as sand grains) settle down in dense layers, the density of the atmosphere only varies on a scale of kilometres. The density of colloidal particles, however, typically varies on a scale of a few microns to a millimetre. Being mesoscopic, colloidal particles have a mass that lies between that of atoms and macroscopic particles. Therefore, their sedimentation behaviour falls between these extremes. This has already been observed by Perrin and been used to determine Avogadro's constant [4].

Sedimentation is only one example where the density or composition is not constant throughout a many-particle system. Such *inhomogeneities* are of special interest both from a fundamental and a more practically oriented point of view.

The presence of an inhomogeneity (such as an interface) in the system can induce many new effects. As an example, consider a system prepared in such a way that the vapour phase is stable. If an interface is present, a layer of liquid may appear even though the liquid phase is not stable in the bulk. This phenomenon is known as *wetting*, and extensive research [5, 6] has been carried out. From a more general point of view, one can scarcely fail to notice that any interaction between a colloidal system and the outside world must by definition involve an inhomogeneity – at least in the form of a surface of the finite system.

Focusing on the individual particles, it is evident that their index of refraction will in general differ from that of the solvent in which they are dispersed. It is possible to *index-match* the solvent to the dispersed particles by mixing it from different components. In practice, however, a slight difference in refractive indices will remain. It has been long known that in this case, fluctuating dipoles will appear, leading to an attractive force between the particles [7]. These *van-der-Waals forces* are usually only important on microscopic and mesoscopic scales. If, however, two macroscopic bodies are brought into very close contact over a large area, a considerable force may result. The stickiness of cling film to smooth surfaces is a prominent example. The ability of geckos to climb smooth surfaces is another: Gecko feet are covered with almost half a million very fine hairs. In total, these hairs make up a large contact area, thus preventing the gecko from sliding off the surface [8].

Colloidal particles are also subject to van-der-Waals forces. The corresponding pair potential has a deep minimum upon contact – in fact, in the idealised case of smooth spheres, the interaction potential diverges. Therefore, whenever two colloidal particles touch, they do not come apart again. The normal phase behaviour of the colloid which depends on the reversibility of the particle movements is thus destroyed.

In order to avoid such *coagulation*, colloids need to be *stabilised*, usually either electrostatically or sterically. Electrostatically stabilised colloids carry an electric charge. When the electrostatic repulsion between the particles is superimposed on the van-der-Waals attraction, a large potential barrier at slightly larger separations is erected, thereby effectively preventing coagulation [9, 10]. However, the potential minimum is not cancelled, so coagulation is still possible over long timescales.

Charge-stabilised colloids are intrinsically susceptible to external electric fields, providing the experimentalist with an easily controllable way to influence their behaviour [11]. Due to the long-ranged nature of the Coulomb potential, there is also a strong interaction between different components in a mixture (and, of course, between different particles of the same component). Moreover, there is a large number of microscopic ions present. Each of these *counter-ions* carries a small charge, thus maintain the global charge-neutrality of the system. Because counter-ions are much smaller and lighter than the *macro-ions*, they interact non-trivially with each other.

In Chapter 2 of this thesis, we turn to such a system and examine the interplay between an external gravitational field and the internal Coulomb forces. We find that in a binary mixture, the interaction of macro-ions and counter-ions and the external gravity field lead to an interesting phenomenon: sedimentation is controlled by the particles' charge per mass rather than by mass only. Therefore, heavy, highly-charged particles may sediment on top of lighter, weakly-charged ones.

In Chapter 3, the effect of an external electric field on a mixture of positively and negatively charged ions is examined. When such an electrolyte is placed between oppositely charged plates – a capacitor – the ions will be influenced strongly by the external electric field. The non-uniform ion distribution, in turn, will generate an electric field internal to the system. Examining the interplay between these fields, we find that a symmetric electrolyte in a capacitor undergoes a transition from a delocalised to a localised state: as long as the voltage $U$ applied across the capacitor remains sufficiently low, the ions are distributed throughout the capacitor. When $U$ rises above a certain threshold value, the ions become localised next to the capacitor plates.

As opposed to exploiting electric forces, colloids can also be stabilised against coagulation by grafting polymers onto the particles' surfaces. As reported in [12], ink was stabilised in this way in ancient Egypt: coagulation will render carbon-based ink unusable after a few minutes unless arabic gum is added to the mixture. Whenever two such particles approach one another, their respective polymer coatings will overlap. This leads to a large reduction of the accessible configuration space of the polymers which in turn gives rise to an entropic repulsion. If the polymers are short as compared to the size of the colloidal particles, the repulsion sets in rather abruptly so that the colloidal particles can be approximated as hard bodies: their interaction potential is infinite whenever they overlap and zero otherwise. Thus, the phase behaviour of such a colloid is governed only by the particles' shapes, and they are said to be *sterically stabilised*. Even the simplest such system, that of hard spheres, already displays phase separation into a fluid and a crystalline phase. Hard spheres can also be realised by charged colloids: if a large amount of salt is added, the macro-ion charges are completely screened by the microscopic salt ions even over very short distances. Thus, the interaction potential becomes that of hard spheres.

Thin rods and platelets are the simplest prolate and oblate hard body systems, respectively. Being non-isotropic, they display not only positional but also orientational order which leads to a variety of different liquid crystalline phases. This makes them interesting for fundamental studies, but platelike and rodlike particles are also found in our everyday life: Flatscreen TV sets and computer monitors influence the orientational ordering of rod-like liquid crystals by external fields in order to display images. Some viruses are also rod-shaped [13, 14], sometimes with aspect ratios in excess of 100 [15, 16]. Platelets occur in everyday life as well, most notably in clay which plays an important role as building

material e.g. for bricks and pots. Plate-like particles have also been subject of intense studies. The phase behaviour of polydisperse platelets [17] and of platelet–polymer mixtures has been studied in computer simulations [18,19] and scaled particle theory [20]. Capillary nematisation and wetting of binary hard-rod and hard-platelet fluids [21] and the Zwanzig model [22,23] in which particle orientations are restricted to the axes of the coordinate system have been subject of theoretical studies. Examples of experimental work include gibbsite, an important aluminium ore [24–26], bentonite [27], and clay suspensions [28,29].

In Chapter 4 we present a density functional theory for mixtures of hard spheres and thin rods (needles). We give explicit expressions for the functional for several simple geometries. As an application, a treatment of the free sphere–needle interface between demixed fluid phases is also presented.

In Chapter 5 we extend the density functional to the Onsager limit, i.e. terms that are linear in the needle thickness $D$ are included in the functional. This allows for a more accurate description of experimental systems at high packing fractions: Rods in real systems always have a finite diameter. The Onsager limit is also a first step toward a functional for rods at finite thickness and can thus foreshadow some of the problems that have to be overcome in order to reach that goal.

In Chapter 6 a density functional for mixtures of spheres, needles and thin platelets is developed along the same principles. The interaction between platelets and spheres turns out to be considerably more difficult than that between needles and spheres, so we restrict ourselves to an approximate treatment of the sphere–platelet Mayer bond. However, we point out in detail what needs to be done in order to recover the exact Mayer bond within the framework of this functional.

Finally, a summary of the results of the present work and some suggestions for future research are given in Chapter 7.

# Part 1

# Segregation Effects in Charged Colloids

CHAPTER 2

# The Colloidal Brazil Nut Effect

## 1. Introduction

Binary systems of granular matter separate upon shaking in gravity, so that the larger particles lie on top of the smaller ones even if they are heavier and denser than the latter. This is due to a sifting mechanism in which tiny grains filter through the interstices between the large particles which is well-known as *Brazil nut effect*: in a jar of mixed nuts or in a package of cereal, the largest species rises to the top [30, 31]. This clearly distinguishes granular matter from ordinary fluids where the rising species is controlled by Archimedes' law. Understanding the full details of the Brazil nut effect is still a problem; recently even a reverse Brazil nut effect of large light grains sinking in a granular bed has been predicted [32–34] and verified in experiments [35].

Here we report on equilibrium density profiles of binary charged colloidal fluids (*macro-ions*) under gravity. Using extensive Monte-Carlo computer simulations of the *primitive model* [36] of strongly asymmetric electrolytes and density functional theory, we predict that the heavier particles sediment on top of the lighter ones provided the charge per mass of the heavier particles is higher. In analogy to granular matter, we call this counter-intuitive phenomenon a *colloidal Brazil nut effect* [37]. It is generated by the entropy of the microscopic counterions in the solution, which are coupled to the macro-ions by strong Coulomb binding. Clearly, though this effect is qualitatively similar to the granular Brazil nut effect insofar as heavy particles are on top of lighter ones, its physical origin is different: first, the particle charge (and not the size) is crucial. Second, the colloidal Brazil nut effect is a pure equilibrium phenomenon while the granular Brazil nut effect happens intrinsically in non-equilibrium. The colloidal Brazil nut effect can be verified, e.g., in depolarised-light scattering or real-space experiments on sediments of strongly deionised binary charged suspensions [38,39]. Similar techniques have been used to measure one-component colloidal density profiles [38,40] where deviations from the ideal barometric law [4,41,42] are still subject to an ongoing debate [43–47].

## 2. Model

We simulate the asymmetric primitive model of binary charged suspensions in which the solvent enters only via a continuous dielectric background with

permittivity $\epsilon$ but all charged particles (two species of negatively charged macro-ions and microscopic counter- and co-ions) are treated explicitly at constant temperature $T$. With $Z_1e$, $Z_2e$, $-qe$ and $\sigma_1$, $\sigma_2$, $\sigma_c$ denoting the charges and the diameters of the two colloidal species and the micro-ions, the interaction between the charged particles is given as a combination of Coulomb forces and excluded volume of the hard particle cores. Here, $e$ is the electron charge. For simplicity we assume that the co- and counter-ions of the salt solution have the same valency and the same hard core diameter $\sigma_c$. We consider a finite system of $N_1$, $N_2$ charged macro-ions and corresponding number of counter-ions (fixed by global charge neutrality) plus salt ions of bulk concentration $c_s$. The simulation box is rectangular with lengths $L_x = L_y$ and $L_z = 32\,L_x$ in the three different spatial directions with periodic boundary conditions in $x$ and $y$ direction and finite length in $z$-direction. Hard walls are placed at $z = 0, L_z$ and gravity with acceleration $g$ points along the $-z$ direction. Only the colloidal particles with their buoyant masses $m_1$ and $m_2$ are subject to gravity, whereas the micro-ions are not.

A Monte-Carlo simulation is performed in the canonical ensemble with the long-ranged Coulomb interaction treated via Lekner sums [48]. Typically $10^3$ Monte Carlo moves per particle were performed for equilibration and it took an additional $10^4$ Monte Carlo moves per particle to gather statistics. Finite system size effects were carefully checked by changing all lateral linear dimensions by a factor of 4. This means that we have changed the total number of colloidal particles $N_1 + N_2$ in the range of 12–200. We have calculated the inhomogeneous $z$-dependent averaged density profiles $\rho_1(z)$, $\rho_2(z)$, $\rho_3(z)$ and $\rho_4(z)$ of the two macro-ions and the counter- and co-ions. Data are shown for the largest system size where $N_1 = N_2 = 100$.

Besides the ratios $Z_1/q$, $Z_2/q$, $m_1/m_2$, $\sigma_1/\sigma_2$, $\sigma_c/\sigma_2$, the system is characterised by two partial area densities $n_i = N_i/L_xL_y$ $(i = 1, 2)$, the Bjerrum length $\lambda_B = q^2e^2/\epsilon kT$ ($kT$ denoting the thermal energy), the gravitational length $\ell_2 = kT/m_2g$ of the second particle species, and the salt concentration. In order to reduce the parameter space, we have assumed throughout the simulations monovalent micro-ions ($q = 1$), and the same hard core diameter of the macro-ions $\sigma = \sigma_1 = \sigma_2$ which serves as a natural length scale. We further fixed $Z_2 = 15$, $\lambda_B = \sigma_c = \sigma/128$ and $n_1 = n_2 = 0.1/\sigma^2$. This corresponds to typical parameters for low-charge aqueous suspensions. We varied the colloidal charge $Z_1$, the colloidal mass ratio $m_1/m_2$ (with $m_1 > m_2$), the gravitational length $\ell_2$, and the salt concentration.

## 3. Results

In the salt-free case, density profiles for the two macro-ions and the counter-ions are shown in Figure 1 for $m_1/m_2 = 1.5$ and three different macro-ion charges $Z_1 = 45, 30, 25$. For large heights $z$, the heavy particles (solid curve) are on top of

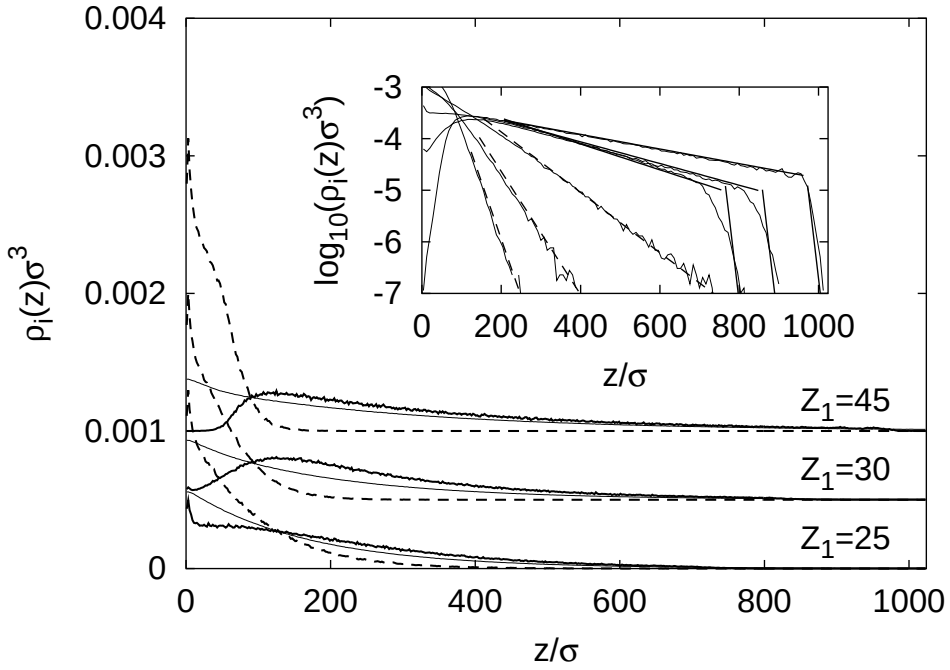


FIGURE 1. Density profiles of macro- and counter-ions for $Z_1 = 45, 30, 25$ (solid lines; top to bottom). The second colloidal component is shown as a dashed line. Counter-ion densities (thin lines) have been divided by $Z_1 + Z_2$. For clarity, curves pertaining to different simulation runs have been shifted by $5 \times 10^{-4}$ with respect to each other. The parameters are: $m_1/m_2 = 1.5$, $\ell_2/\sigma = 10$, $c_\mathrm{s} = 0$. Inset: Semi-logarithmic plots of the same colloidal density profiles with the slopes predicted from theory.

the lighter ones (dashed curve). This colloidal Brazil nut effect is getting stronger for increasing charge asymmetry between the colloidal particles: for the highest charge $Z_1 = 45$, the two macro-ion species are almost completely separated. To quantify the Brazil nut effect, we define – in analogy to the ordinary Brazil nut problem [34] – a mean (or sedimentation) height of the two profiles via

$$h_i = \frac{\int_0^\infty z\rho_i(z)\,\mathrm{d}z}{\int_0^\infty \rho_i(z)\,\mathrm{d}z} \qquad i = 1, 2 \tag{2.1}$$

By definition, the colloidal Brazil nut effect occurs if $h_1 > h_2$, but there is no Brazil nut effect in the opposite case, $h_1 \leq h_2$.

Let us now describe the properties of the density profiles for increasing $z$ qualitatively and put forward a simple theory to describe the basic features. Close to the hard container bottom at $z = 0$, small correlation effects are visible as a density shoulder of the low-charge particles while high-charge particles are depleted from the wall. The reason is a combination of a pure interface

effect and Archimedes' principle. First, we have checked by simulation that depletion of high-charge particles persists for zero gravity. Second, by crudely mapping the interacting binary colloidal mixture onto one with effective hard interaction cores, the high-charge particles will have a larger diameter and hence Archimedes' principle will lift the high-charge particles in the sea of small ones provided their mass density is smaller [49]. For our parameters, however, the latter effect is small and confined to regions close to the wall. More importantly, as revealed by the semi-logarithmic plot in the inset of Figure 1, there is an exponential decay of the two colloidal profiles for intermediate heights associated with two different decay lengths for the two colloidal species. The decay length for the heavier but high-charge particles is larger than that for the low-charge particles. This gives the most significant contribution in the integral (2.1) of the mean height. Finally, for large $z$, a cross-over appears towards another exponential decay involving the gravitational length $\ell_1 = kT/m_1 g$ for the high-charge particles. It is important to note that the density profiles fulfil *local charge neutrality* throughout the whole sample except at the container bottom ($z = 0$) and at very large heights $z$. But even there the excess charge separated is small.[1]

Our theoretical explanation for the colloidal Brazil nut effect is based on a simple density functional approach. The free energy $\mathcal{F}$ per unit area, which is a functional of the inhomogeneous density fields $\rho_1(z), \rho_2(z), \rho_3(z)$ of the macro- and counter-ions, splits into the gravitational energy, the entropy of the three species, and all Coulomb contributions. The latter are approximated within a mean-field-type Poisson-Boltzmann theory [43–47]. Hence:

$$\begin{aligned}\mathcal{F}[\rho_1(z), \rho_2(z), \rho_3(z)] = &\sum_{\nu=1}^{2} \int_0^\infty m_\nu g z \rho_\nu(z)\, \mathrm{d}z \\ &+ \sum_{\nu=1}^{3} \int_0^\infty kT \rho_\nu(z)(\ln(\Lambda_\nu^3 \rho_\nu(z)) - 1)\, \mathrm{d}z \\ &+ \frac{1}{2} \int_0^\infty \int_0^\infty \frac{\rho_t(z)\rho_t(z')}{\epsilon\sqrt{r'^2 + (z-z')^2}} \mathrm{d}z'\, \mathrm{d}z\, \mathrm{d}^2 r' \quad (2.2)\end{aligned}$$

Here, $\Lambda_\nu, (\nu = 1, 2, 3)$, are Lagrange multipliers which ensure that the overall colloidal densities per unit area equal the prescribed number densities, i.e. $\int_0^\infty \rho_i(z)\, \mathrm{d}z = n_i$ $(i = 1, 2)$. $\Lambda_3$ is fixed by *global* charge neutrality, and $\rho_t(z) = Z_1 e \rho_1(z) + Z_2 e \rho_2(z) - q e \rho_3(z)$ is the total *local* charge density of the system. The functional $\mathcal{F}$ is minimal for the physically realised equilibrium density profiles.

[1] The charge non-neutrality at the system boundaries will result in a small electric field as recently predicted by theory in Ref. [47] and also confirmed by simulation of the one-component colloidal system [50]. The presence of this field, however, will change neither the density field for intermediate $z$ nor the general conclusions of our analysis which assumes local charge neutrality.

We discuss two different cases of weak and strong Coulomb coupling subsequently. For weak Coulomb coupling, which is realised for very large heights $z$ where the densities are extremely small, one may neglect the third term on the right-hand side of Eq. (2.2). Then, the minimisation of $\mathcal{F}$ yields colloidal density profiles which follow the traditional barometric law $\rho_i(z) \propto \exp(-z/\ell_i)$ $(i = 1, 2)$. Strong Coulomb coupling, on the other hand, will impose *local* charge neutrality $\rho_t(z) = 0$ which implies that the counter-ion density field is enslaved to that of the macro-ions. Minimising $\mathcal{F}$ in this limit with respect to the two colloidal densities only, again yields an exponential decay $\rho_i(z) \propto \exp(-\gamma_i z)$ $(i = 1, 2)$ but with inverse decay lengths $\gamma_i$ which are smaller than $1/\ell_i$. These decay lengths $\gamma_i$ turn out to be as follows: Let $\alpha$ be the index $i$ for which the mass per charge ratio $\frac{m_i}{Z_i/q+1}$ is *minimal* and let $\beta = 3-\alpha$ be the index complementary to $\alpha$, i.e. $\beta = 1$ if $\alpha = 2$ and $\beta = 2$ if $\alpha = 1$. Then

$$\gamma_\alpha = \frac{m_\alpha}{Z_\alpha/q + 1} \frac{g}{kT} \tag{2.3}$$

and

$$\gamma_\beta = \left( m_\beta - m_\alpha \frac{Z_\beta}{Z_\alpha + q} \right) \frac{g}{kT} > \gamma_\alpha \tag{2.4}$$

with $\gamma_\beta \geq \frac{m_\beta g}{kT(Z_\beta/q+1)} \geq \gamma_\alpha$. This second case of strong Coulomb coupling will be realised for heights $z$ where correlations between the ions are small (which justifies the mean-field approximation) but where local charge neutrality is still valid. The physical reason for the much slower decay of the colloidal density profiles in the second regime results from the counter-ion entropy which tends to delocalise the counter-ions. However, since the macro-ions are coupled to the counter-ions due to the constraint of local charge neutrality, they are lifted upwards together with their counter-ions. Assuming that the main contribution in the integrand of the right-hand side of (2.1) comes from the second regime, the mean heights are given by $h_\alpha = 1/\gamma_\alpha$ and $h_\beta = 1/\gamma_\beta$. A Brazil nut effect occurs when $\alpha = 1$ and $\beta = 2$. Hence the transition towards the Brazil nut effect happens at $\frac{m_1}{Z_1/q+1} = \frac{m_2}{Z_2/q+1}$.

Let us now test the prediction of the theory against our simulation data. First, the slopes in the inset of Figure 1 confirm the inverse decay lengths $\gamma_\alpha$ and $\gamma_\beta$ perfectly for a large range of intermediate heights; the theoretical predictions for the slopes as given by Eqs. (2.3) and (2.4) are shown as thick lines. The crossover to the bare gravitational length for large $z$ is confirmed for the high-charge particles and is found to be pretty sharp. Consistently with the theoretical assumption, local charge neutrality in the intermediate regime is fulfilled. Second, we have tested the location of the transition towards the colloidal Brazil nut effect by systematically varying the mass and charge ratio. The results are summarised in Figure 2. The theory, which predicts the transition at $(Z_1 + 1)/(Z_2 + 1) = m_1/m_2$, is shown as a straight line there. All parameter

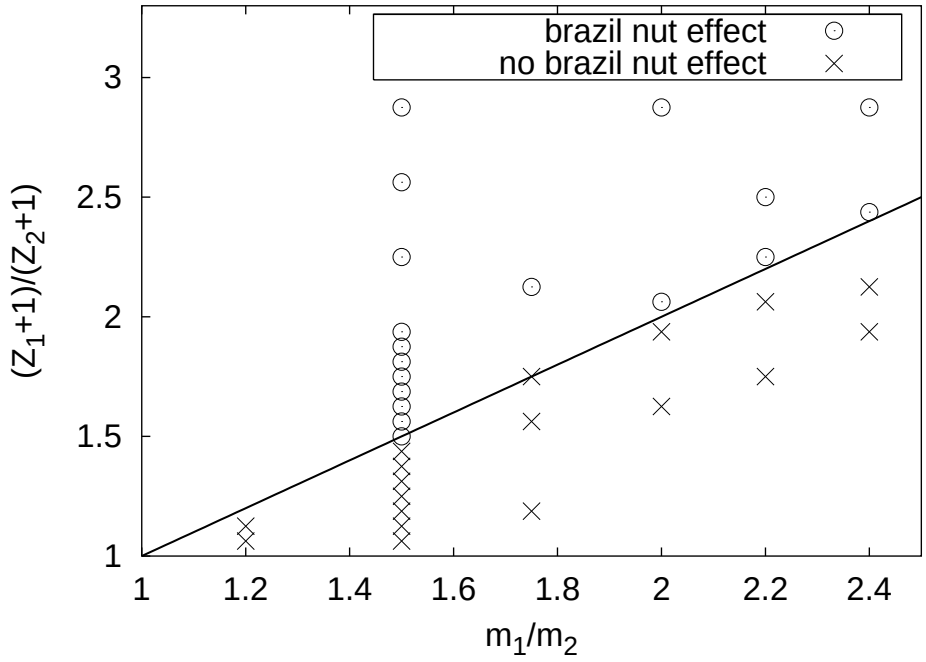


FIGURE 2. Crossover towards the Brazil nut effect. Shown are different charge asymmetries $(Z_1 + 1)/(Z_2 + 1)$ and mass ratios $m_1/m_2$ for which the Brazil nut effect was (circles) or was not observed (crosses). The straight line shows the theoretical prediction. The parameter combinations were obtained by changing $\ell_2$ and $Z_1$ in the range of $4 \ldots 20\,\sigma$ and $16 \ldots 45$, respectively.

combinations simulated are indeed separated by this theoretical prediction, confirming our simple theory. This is remarkable as any wall or bulk correlation effects are neglected in the theory.

In order to elucidate this further, we have compared the theoretical predictions $1/\gamma_1$, $1/\gamma_2$ for the heights with the simulation data in a situation where the transition line was crossed. In Figure 3 the heights are shown as a function of a varied charge $Z_1$. The simulation data reveal that the variation of both heights $h_i$ with $Z_1$ is large close to the transition and becomes maximal at the transition. In the theory, this feature is reproduced and accompanied by a generic cusp at the transition. Moreover, a marked maximum in the fluctuations of the mean heights of both species appears at the cusp. Though the cusp is smeared out and in general the heights are larger in the simulation data due to the density reduction close to the wall, there is still semi-quantitative agreement. The rapid variation of the heights at the transition implies that the location of the transition towards the Brazil nut effect is very robust explaining the validity of the theory in Figure 2.

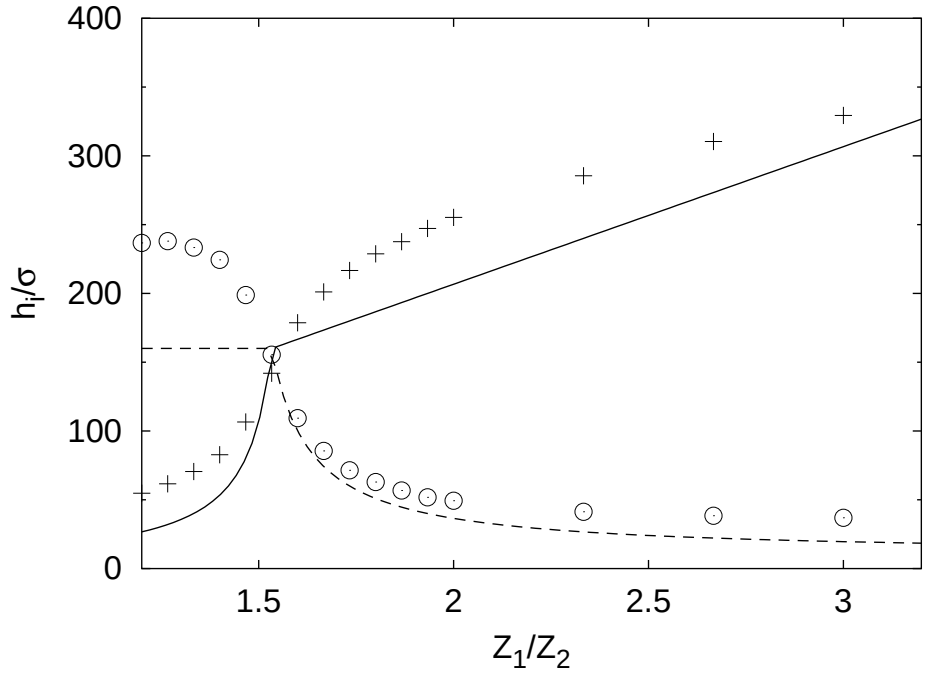


FIGURE 3. Mean heights $h_i$ of heavy (+) and light ($\odot$) particles as a function of $Z_1$ for the parameters of Figure 1, namely $m_1/m_2 = 1.5$, $\ell_2/\sigma = 10$, $c_s = 0$. The lines show the theoretical predictions.

Finally we address the case of added monovalent salt. Density profiles for the two macro-ion species and the counter- and co-ions are presented in Figure 4. Addition of salt reduces the Brazil nut effect; in the inset of Figure 4 the heights are plotted versus added salt concentration. The $c_s^{(0)}$ needed to reverse the Brazil nut effect is estimated as $c_s^{(0)} \approx Z_1\rho_1(z_0) + Z_2\rho_2(z_0)$ which is the counter-ion concentration at the position $z_0$ where the two colloidal density profiles cross in the salt-free case. This salt concentration is indicated as an arrow in the inset of Figure 4, confirming the validity of the estimate. Though the Brazil nut effect is proven to remain stable with respect to added salt, it will only show up for de-ionised solutions. Highly charged suspensions in non-polar solvents with a small dielectric constant $\epsilon$ and low impurity ion concentrations [51] are promising candidates to exhibit a strong Brazil nut effect.

## 4. Conclusions and Outlook

In conclusion, we predict an analog of the granular Brazil nut effect in equilibrium sediments of charged suspensions, which is generated by an entropic charge lifting due to the Coulomb coupling to the counter-ions. An experimental verification of the levitation should be possible employing depolarised light scattering [38] or confocal microscopy [51]. The simulated charge asymmetries

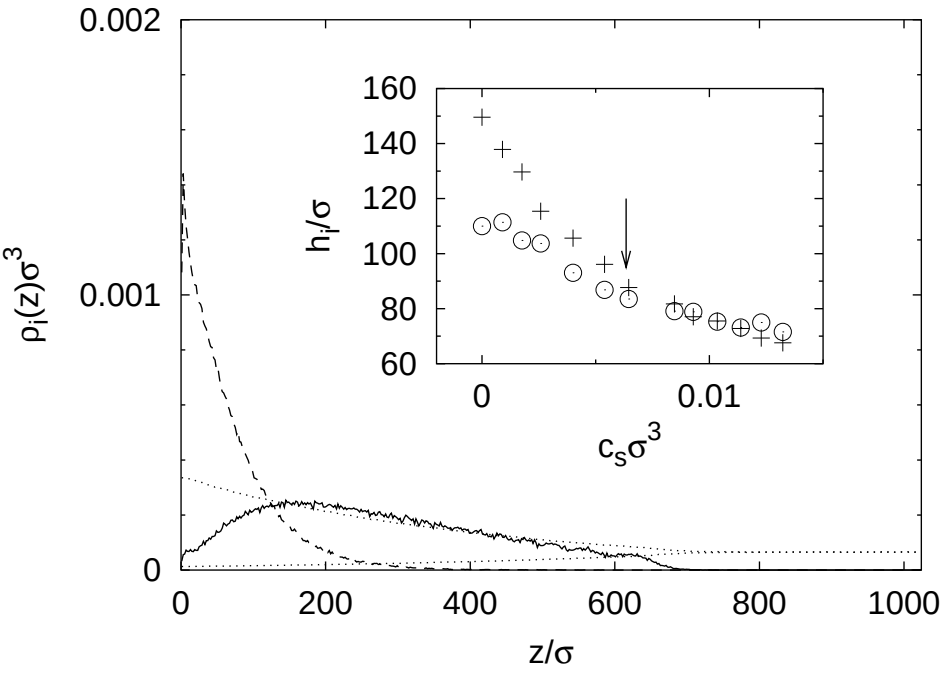


FIGURE 4. Density profiles for added salt. The macro-ion densities are shown by the thick lines. The counter- and co-ion densities (thin dotted lines) have been divided by $Z_1 + Z_2$; the co-ion density is smaller than that of the counter-ions. The parameters are $Z_1 = 45$, $m_1/m_2 = 2$, $\ell_2 = 20\,\sigma$, and $c_s\sigma^3 = 2.5 \times 10^{-3}$. Inset: Sedimentation heights $h_i$ of heavy (+) and light ($\odot$) particles as a function of reduced salt concentration for $Z_1 = 32$, $m_1/m_2 = 2$, and $\ell_2 = 5\,\sigma$. The theoretical estimate of the threshold salt concentration is marked by an arrow.

correspond to micelles and proteins rather than highly charged colloids but the simple theory which was confirmed by the simulations is applicable for arbitrary charges.

The lifting effect is immediately generalisable to sediments of solutions which are polydisperse in mass and charge [52]. Therefore the colloidal Brazil nut effect has important biochemical implications for the separation of polydisperse biological matter, such as protein solutions. Analytical sedimentation is typically used in an ultracentrifuge to separate different species [53]. The colloidal Brazil nut effect implies that the separation is sensitive to the mass per charge but not to the mass itself. Recently, J. Zwanikken *et al.* [54] have generalised the functional (2.2) to polydisperse systems. Performing a free minimisation – in contrast to our simple parameterisation – of this functional, they have been able to achieve very good agreement with the simulation data that have been

presented in this chapter. For polydisperse systems, Zwanikken *et al.* predict that species also segregate according to their mass-per-charge ratio.

CHAPTER 3

# Localisation–Delocalisation Transition of Electrolytes Between Microelectrodes

## 1. Introduction

If a charged body is placed into a salt solution, the cations and anions of the salt will screen the body charge. For high temperatures and/or low charge densities, the traditional linearised screening theory leads to an electric double layer around the charged body surface which involves an exponentially decreasing density field of the micro-ions as a function of their distance to the surface. One of the simplest set-ups are two parallel homogeneously charged plates with the famous solution of Gouy-Chapman almost a century ago [55, 56]. Subsequently, further linear and nonlinear screening theories have been performed and the electrostatic forces acting between two parallel plates have been calculated, see e.g. Ref. [57–61] and references therein.

While the colloidal community has spent much effort to investigate the interaction between like-charge plates which directly affects colloidal stability, one of the central topics of electrochemistry concerns electrolytes between plates of *opposite* charges. The latter situation, an electrolyte in a capacitor or condenser, is relevant for a fundamental understanding of electrodes. Here the surface charge density on, or equivalently, the electric field between the plates can be tuned by the external voltage $U$ applied. Recent progress has also been achieved in miniaturising capacitors leading to well-controlled micro-electrodes [62–64] or even nano-electrodes [65, 66] in an electrolyte solution. These are used as basic switching elements in micro-fluidic devices and in nano-electronics.

In this chapter, we show that symmetric electrolytes in a condenser of two oppositely charged plates undergo a transition from a localised to a delocalised state. The transition occurs as a function of external voltage $U$ applied for fixed electrolyte area density and temperature in the limit where the plate distance $D$ goes formally to infinity. The order parameter of the transition is the first moment $\langle h \rangle$ of the micro-ion density profiles which is the averaged distance of the anions and cations to the oppositely charged plate. If $\sigma$ denotes the modulus of the charge of anions (or cations) between the plates per unit area, the transition occurs exactly at that voltage $U_c$ which equals the surface charge density of the plates, $\sigma_p$, to $\sigma$. The fingerprint of this transition is a *logarithmic divergence* of the order parameter $\langle h \rangle$ in $(U - U_c)/U_c$ for $U \searrow U_c$ (resp. in $(\sigma - \sigma_p)/\sigma_p$ for $\sigma_p \searrow \sigma$). For $U < U_c$, on the other hand, the averaged distance is of the

order of the plate distance $D$ diverging in the limit $D \to \infty$. This is obtained by Poisson-Boltzmann theory and confirmed by computer simulations of the primitive electrolyte model with explicit micro-ions.

The physical reason for the localisation-delocalisation is simple: for $U > U_c$ (resp. for $\sigma < \sigma_p$), all electrolyte ions will feel an external electric field attractive to the plates of opposite charge, and *all* ions will screen this field which results in a localised density profile decaying exponentially with the distance to the plates. On the other hand, for $U < U_c$ (resp. for $\sigma > \sigma_p$), a fraction of the electrolyte ions is sufficient to completely screen the surface charge. Hence the rest of them is free to delocalise between the plates due to entropy reasons. Despite its simplicity we are not aware that this transition has been discussed previously in the literature. This might be due to the fact that for typical electrolyte solutions between charged plates, one encounters the delocalised case $\sigma > \sigma_p$. This is different, however, for micro-electrodes where, at fixed bulk salt concentration, the area density $\sigma$ can be drastically reduced by a confinement which is, however, still larger than the molecular length scales. Therefore, as we shall detail below, the transition is clearly detectable in micro-electrodes.

## 2. Model

In our theoretical model, we consider a system of two species of ions with charges $+qe$ and $-qe$, respectively, ($q > 0$), and microscopic hard core diameters $d$. The ions are kept at finite temperature $T$ and placed in a solvent of dielectric permittivity $\epsilon$ inside a capacitor. The condenser consists of two homogeneously and oppositely charged planar plates which are a distance $D$ apart. The plates are no in contact with the electrolyte to prevent electrolysis. The plate charge is $\sigma_{\rm p}$ at $z = 0$ and $-\sigma_{\rm p}$ at $z = D$. The total micro-ion number density per plate area is denoted $2\sigma$. The system is globally charge neutral. One of the basic length scales is the microscopic Bjerrum length $\lambda_{\rm B} = q^2e^2/\epsilon kT$ which is the typical distance where two oppositely charged ions gain a thermal energy $k_BT$. The opposite plate charges $\pm\sigma_{\rm p}$ lead to an external electric field in the condenser, $E = 4\pi\sigma_p/\epsilon$. Equivalently one may see the plate charge originating from an external voltage $U$ applied with $U = ED$. The plates are infinitely large in the $x$ and $y$ directions. We address the case of large plate distances $D$, taking formally the limit $D \to \infty$ at finite $\sigma$. The key quantity to characterise localisation and delocalisation are the inhomogeneous averaged density profiles, $\rho_+(z)$ and $\rho_-(z)$ of the cations and anions. Due to symmetry, $\rho_-(D/2 + z) = \rho_+(D/2 - z)$, hence it is sufficient to consider only one species. The whole set-up is shown schematically in Figure 1.

## 3. Poisson–Boltzmann Theory

An analytical approach is provided by one-dimensional nonlinear Poisson-Boltzmann theory [67–69] which is a mean-field approximation. This approach

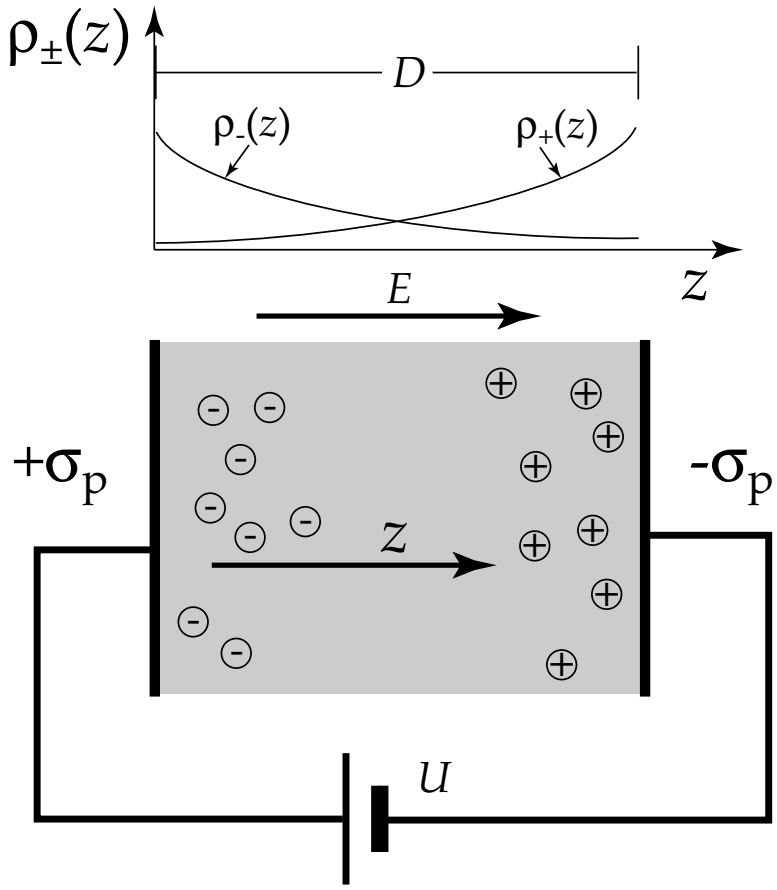


FIGURE 1. Schematic drawing of the electrolyte condenser considered. The voltage $U$ is applied across the capacitor, charging the plates to the area charge density $\sigma_{\mathrm{p}}$. This corresponds to an electric field $E$ external to the electrolyte. The microscopic cations and anions are shown in the dielectric fluid, and their averaged density profiles $\rho_+(z)$ and $\rho_-(z)$ are sketched as well.

incorporates entropy and electrostatics but neglects any correlations and fluctuations of the electrolyte. Let us assume that we have a situation above the transition, $U > U_c$, such that we are dealing with localised micro-ion density profiles close to the plates. Since the plate distance is large, it is reasonable to further assume completely separated cation and anion density profiles in the two slabs separated by the midplane of the condenser at $z = D/2$. Then Poisson's and Boltzmann's equations read as

$$\frac{\mathrm{d}^2\Phi(z)}{\mathrm{d}z^2} = -\frac{4\pi}{\epsilon} qe\rho_-(z) \tag{3.1}$$

$$\rho_-(z) = \frac{\sigma}{D} e^{-qe\Phi(z)/kT} \tag{3.2}$$

in the domain $0 \leq z \leq D/2$ for the anionic density. Here, $\Phi$ is the electric potential.

The analytical solution is

$$\rho_-(z) = \frac{A\lambda\sigma}{\sinh^2\bigl(\sqrt{A}z + \varphi\bigr)} \tag{3.3}$$

where $A$ and $\varphi$ are determined from the boundary conditions $\int_0^{D/2} \rho_-(z)\,\mathrm{d}z = \sigma$ and $\mathrm{d}\Phi(z)/\mathrm{d}z|_{z=0} = -E$ as $\coth\varphi = 1/(b\sqrt{A})$ and $A = [1/b - 1/\lambda]^2$ where $b = 1/(2\pi\lambda_\mathrm{B}\sigma_\mathrm{p})$ is the traditional Gouy-Chapman length, and we introduce the *localisation length* $\lambda = 1/(2\pi\lambda_\mathrm{B}\sigma)$. Clearly, for nonzero $A$ the density profile (3.3) is localised. Hence, necessarily, $A$ has to vanish at a possible localisation-delocalisation transition. This yields the threshold criterion for the critical electric field $E_\mathrm{c} = 4\pi qe\sigma/\epsilon$ or the critical external voltage $U_\mathrm{c} = E_c D$. Equivalently, this can be expressed as $\sigma_\mathrm{p} = qe\sigma$ or $\lambda = b$. Note that $E_\mathrm{c}$ is also equal to the maximum *internal* electric field that is generated by complete separation of charges in the system. In other words, the density profiles are delocalised whenever the system can compensate for the external electric field by building up an equal but opposite internal field. When the external field is too strong to be compensated for, the remaining field localises the ions next to the capacitor plates.

In order to quantify the localisation-delocalisation transition, we introduce the first moment of the density profile as an order parameter defining a characteristic height

$$\langle h\rangle = \frac{\int_0^{D/2} z\rho_-(z)\,\mathrm{d}z}{\int_0^{D/2} \rho_-(z)\,\mathrm{d}z}. \tag{3.4}$$

Eqn. (3.3) yields

$$\langle h\rangle = \lambda \ln\frac{2\delta+1}{2\delta}. \tag{3.5}$$

where $\delta = (U - U_c)/U_c \equiv (E - E_c)/E_c > 0$ measures the dimensionless distance to the transition. Thus, the characteristic height $\langle h\rangle$ diverges logarithmically $\propto \ln\delta$ as the external voltage approaches its critical value $U_\mathrm{c}$.

We have further performed extensive computer simulations of the primitive electrolyte model where the solvent is treated as a dielectric continuum [59]. This model includes any correlations and fluctuations of the micro-ions which are neglected in the analytical Poisson-Boltzmann approach. We consider a finite, globally charge-neutral system of $N$ cations and $N$ anions in a rectangular simulation box with lengths $L_x, L_y, D$ and periodic boundary conditions in the $x$ and $y$ directions. Walls impenetrable to the ions are placed at $z = 0, D$, and an external electric field $\mathbf{E} = E\mathbf{e_z}$ is applied in the $z$ direction. We take $L \equiv L_x = L_y$ and vary $D$ and $L$ to check for finite-size effects.

A Monte-Carlo (MC) simulation is performed in the canonical ensemble. The Coulomb interaction is calculated via Lekner sums [48]. We use the Bjerrum

length $\lambda_B$ as the basic length scale. The hard-core diameter of the ions was $d = 0.25\,\lambda_B$. The lateral system size was $L = 512\,\lambda_B$ for most runs. Upon increasing it to $1024\,\lambda_B$ to check for finite size effects, the results did not change. The area density per species varied between $0.95 \ldots 4.8 \times 10^{-4}\lambda_B^{-2}$ for the smaller system corresponding to a total number $2N$ of simulated particles varying between 2000 and 10000. Equilibration took typically 250 MC steps per particle; statistics were gathered during 50000 MC steps per particle. The distance between the capacitor plates was varied between $D = 128\,\lambda_B$ to $D = 4096\,\lambda_B$.

Simulation data for the density profiles for $\delta = 3.17$ and $\delta = 0.043$ are presented in Figure 2. The parameters were chosen to be $\sigma = 9.54 \times 10^{-4}\lambda_B^{-2}$, $D = 4.10 \times 10^3 \lambda_B$ and $L = 5.12 \times 10^2 \lambda_B$. One can clearly see the delocalisation of the density profiles close to the transition. The predictions of Poisson-Boltzmann theory for positive $\delta$ as given by Eq. (3.3) are also included and show favourable agreement with the simulation data.

Furthermore we have performed a detailed approach towards the transition for three different parameter combinations. The resulting heights $\langle h \rangle$ are shown in Figure 3. We have plotted the data using the universal scaling representation suggested by the theory. The averaged height is scaled with the length scale $\lambda$, and the distance to the transition is just expressed by the dimensionless $\delta$. Not only do the simulation data fall onto the same universal curve, there is even quantitative agreement with the prediction (3.5) of our analytical Poisson-Boltzmann approach. The inset of Figure 3 shows the same data on a semi-logarithmic plot proving that there is indeed a logarithmic divergence in the simulation data. Based on both Figures 2 and 3 we conclude that the predictions of the Poisson-Boltzmann theory are quantitatively confirmed by the simulation. Regarding the divergence of $\langle h \rangle$ close to the transition ($0 < \delta \ll 1$), we think that Poisson-Boltzmann theory is still adequate. Correlation effects may lead to micro-ion structuring and layering near the walls. Halfway between the plates, however, the concentration of micro-ions is small close to the transition such that Poisson-Boltzmann theory is still applicable there. Therefore we believe that the asymptotic form of the divergence (3.5) will not be changed for strong Coulomb coupling. The same insensitivity is expected for surface charge modulations [70, 71] provided the modulation length is much smaller than the plate spacing $D$.

## 4. Conclusions

Finally we discuss whether the condition at the delocalisation-localisation transition, $\sigma_p = qe\sigma$, can be fulfilled in realistic samples. This criterion needs high plate charges $\sigma_p$ and small electrolyte densities $\sigma$. Let us subsequently estimate limits for these two quantities. Very highly charged plates immersed into an electrolyte will lead to chemi- and physisorption of the microscopic ions [72] such that they are not any longer dissociated. A typical maximum for an

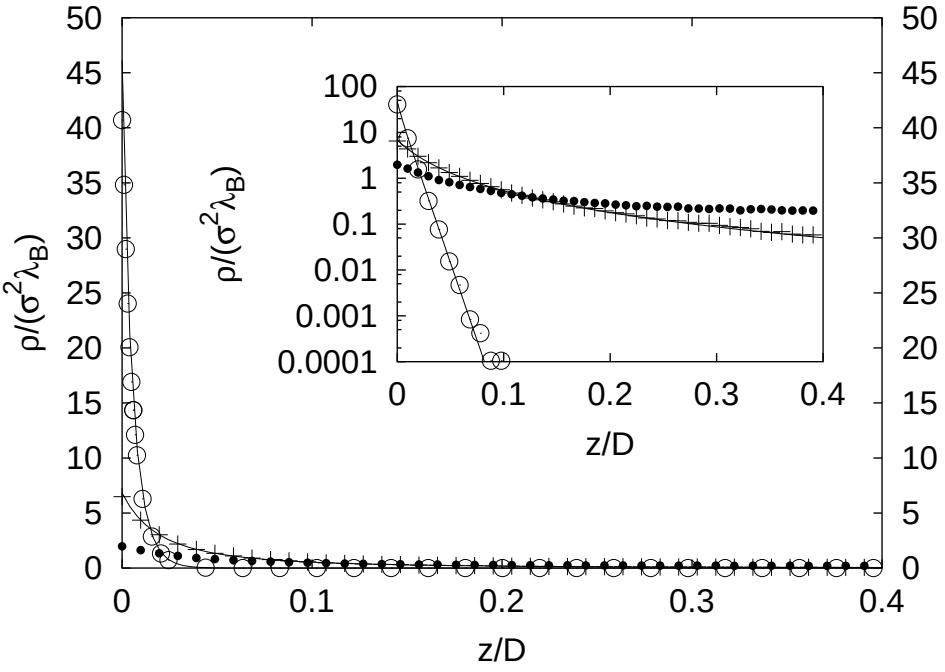


FIGURE 2. Density profiles as obtained by simulation for $\delta = 3.17$ (+) and $\delta = 0.043$ (∘) and their respective theoretical predictions. A delocalised density profile ($\delta = -0.48$) is also shown (small dots). The other parameters were $\sigma = 9.54 \times 10^{-4} \lambda_{\mathrm{B}}^{-2}$, $D = 4.10 \times 10^{3} \lambda_{\mathrm{B}}$ and $L_x = L_y = 5.12 \times 10^{2} \lambda_{\mathrm{B}}$. The inset shows the same data on a semilogarithmic scale.

effective renormalised plate charge is given by the Manning threshold value [73] and is of the order of $\sigma_{\mathrm{p}} = 1\, e/\lambda_{\mathrm{B}}^2$. In aqueous solutions at room temperature, monovalent electrolytes typically have bulk concentrations ranging from at least $10^{-6}$ mol/litre to $10^{-3}$ mol/litre. Depending on the electrolyte concentration, the criterion therefore requires plate distances which are in the range between a millimetre and a micrometre to see the transition. The conclusion from this estimate is that the transition can in principle be observed in small condensers. However, for reasonable electrolyte concentrations, one has to go down to micro-electrodes.

In an experiment on micro-electrodes, one can see the fingerprints of the transition by watching the electrolyte concentration directly. This is in principle possible by fluorescent marking of the micro-ions (see e.g. [74, 75] for recent progress in this domain) Alternatively, the transition may be observed by watching the response of the system [76, 77] under a time-dependent AC electric field. Close to the localisation-delocalisation transition, there should be a marked anomaly in the resistance at low frequencies; a delocalised state should contribute

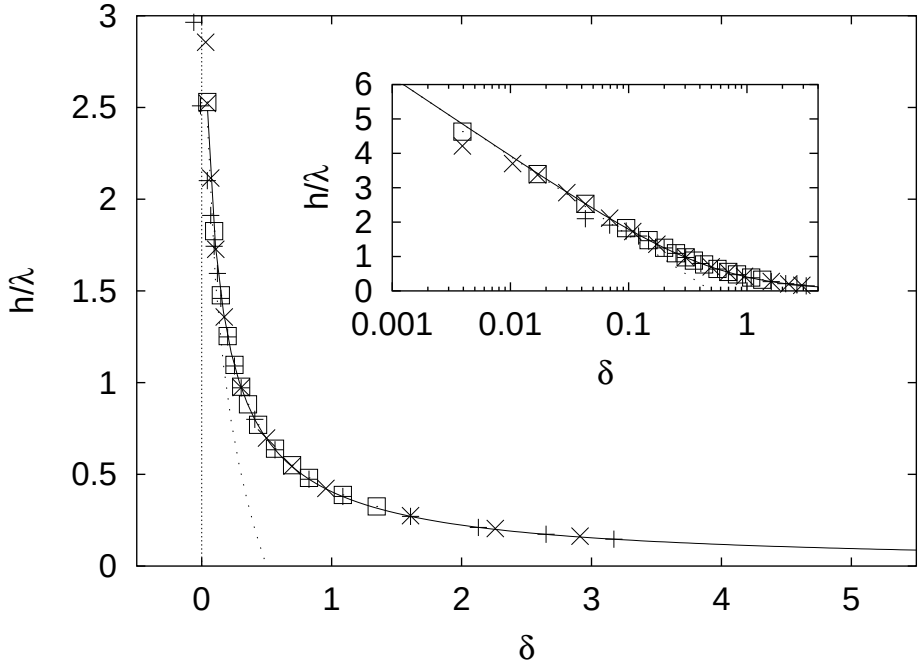


FIGURE 3. Reduced mean height $h/\lambda$ of one species as a function of the reduced external field $\delta$. The solid line shows the theoretical prediction. It diverges at $\delta = 0$. The asymptotic behaviour $\propto \ln \delta$ for small $\delta$ is shown as a dotted line. Simulation results are shown for different area densities, namely $\sigma = 9.5 \times 10^{-4}\, \lambda_{\mathrm{B}}^{-2}$ (+), $\sigma = 7.6 \times 10^{-3}\, \lambda_{\mathrm{B}}^{-2}$ (×), and $\sigma = 1.9 \times 10^{-2}\, \lambda_{\mathrm{B}}^{-2}$ (□). The other parameters were $D = 4.10 \times 10^{3} \lambda_{\mathrm{B}}$ and $L_x = L_y = 5.12 \times 10^{2} \lambda_{\mathrm{B}}$. The inset shows the same data in a semi-logarithmic plot.

much more efficiently to the conductivity than a localised one. Another implication of the delocalisation-localisation transition concerns the transport of mesoscopic neutral particles with an electric dipole moment (e.g. proteins close to the isoelectric point) in the transverse direction of a micro-electrode. Tuning the external voltage such that the system parameters are close to the transition, it is expected that the effective interaction and the transport through such a micro-fluidic device can be tailored at wish.

In conclusion, we have predicted a sharp localisation-delocalisation transition in a electrolyte solution confined to a condenser as a function of the external voltage applied. At the transition, there is a qualitative change in the screening of the condenser plates by the electrolyte. There are either enough electrolyte ions in order to completely screen the plate charge leaving additional ions in the solution which are delocalised due to entropy. Or micro-ions are missing for complete screening, but then they are all localised. Crossing through the transition produces a logarithmic divergence of the averaged distance of the

micro-ions to the plates in the limit of large plate distances. The basics of this transition is a simple competition between entropy and electrostatics, and nonlinear Poisson-Boltzmann theory describes it adequately. It would be interesting to systematically investigate electrolytes in micro-electrodes in order to detect this transition experimentally.

We finally point out that a similar effect occurs in asymmetric electrolytes and even for strongly asymmetric systems such as nanometric proteins or mesoscopic charged colloids. It would be interesting to expose sedimenting charged suspensions [38, 47, 50, 78] to an additional electric field and study the corresponding levitation. [1]

[1]Note that the logarithmic divergence law is qualitatively different from the ordinary divergence in a levitating solution where, when gravity $g$ goes to zero, the averaged height $\langle h \rangle$ diverges *algebraically* as $1/g$.

# Part 2

# Effects of Particle Shape

CHAPTER 4

# Mixtures of Spheres and Thin Rods

## 1. Introduction

Mixtures of spherical and rod-like particles provide soft matter systems that display astonishingly rich phase behaviour [79]. When a second component is added as a depletant agent to a suspension of colloidal spheres, the spheres may exhibit colloidal vapour, liquid, and crystalline phases. Rod-like depletants alone, however, already have rich liquid-crystalline phase behaviour. The possible combinations of both types of ordering are vast. Experimental examples of rod-sphere mixtures are dispersions of silica spheres and silica coated boehmite rods [80, 81], silica beads immersed in suspensions of rod-like fd bacteriophage virus [13, 14], and, in the biological domain, microtubules inside vesicles modelling the eukaryotic cell [82, 83]. Experimental work has also been devoted to self-diffusion and sedimentation of spheres in dispersions of rods [84]. Depletion-induced crystallisation was found in mixtures of colloidal silica spheres and colloidal silica rods with light microscopy and confocal scanning laser microscopy [81]. Fluid–fluid phase separation was observed experimentally in a mixture of silica spheres and semi-flexible polymeric rods (PBLG with molecular weight 105000) [85]. The free interface between demixed fluid phases is one topic that we address in the present chapter.

As a simple theoretical model of a rod–sphere mixture Bolhuis and Frenkel proposed a binary system of hard spheres and vanishingly thin hard needles [86]. Due to the vanishing needle thickness, and hence the absence of interactions between needles, this system does not display liquid crystalline order, but exhibits (sphere) vapour, liquid and solid states, as was found in Ref. [86] with simulation and a perturbation theory. The theory is similar to the free volume treatment of the Asakura-Oosawa (AO) model [87,88] of colloidal spheres and non-interacting polymer spheres by Lekkerkerker et al. [89]. The depletion potential exerted on a pair of spheres due to the presence of the rods was studied theoretically [90], and experimentally using optical tweezers [13, 14]. Considerable work was done to understand the nature of the depletion force due to rodlike polymers in the Onsager limit [91], and the interactions between flat plates and between two large spheres via the Derjaguin approximation [92]. Theoretical phase behaviour of mixtures of spheres and rods with finite diameter were studied in Ref. [80] and compared to experiment [81], and in a mixture of parallel hard spherocylinders and hard spheres layered phases were investigated [93].

Density-functional theory (DFT) [94, 95] is a powerful tool to study equilibrium properties of inhomogeneous many-particle systems. For realistic systems, one usually has to rely on approximations for the central quantity of DFT, the excess free energy functional. One particularly successful example of such an approximation is Rosenfeld's density functional for hard sphere (HS) fluids [96] that also describes the HS solid [97–100]. An early extension of this theory to treat hard convex bodies was proposed [101], and used to derive bulk direct correlation functions for molecular fluids [102], two-dimensional anisotropic fluids [103], and hard sphere chain fluids [104]. The theory of Ref. [101] suffered from an incomplete deconvolution of the Mayer bond leading to an incorrect virial expansion, and an extension to remedy this deficiency was made for the model of hard spheres and hard, vanishingly thin needles [105]. Subsequently, this was also generalised to a hard body amphiphilic mixture [106] and to mixtures of colloidal spheres, rods and polymer spheres [107]. Recently, the entropic torque exerted on a single spherocylinder immersed in a hard sphere fluid at a hard wall was calculated with a similar approach [108].

In contrast to the case of simple fluids, interfaces in such complex systems are genuinely characterised by positional *and* orientational order. Interfaces between phases with different liquid crystalline ordering, like isotropic-nematic interfaces, have attracted considerable interest, see Ref. [109] for a recent study of the hard-rod fluid. In this chapter we investigate the free interface between demixed (isotropic) fluid phases in a rod-sphere mixture, an issue that has not been addressed so far. We use the simplest non-trivial model in the context, namely Bolhuis and Frenkel's mixture of hard spheres and vanishingly thin needles, and investigate it by means of the geometry-based DFT proposed earlier [105]. As this theory reproduces the bulk fluid free energy and hence the accurate fluid demixing binodal of perturbation theory [86], and was also shown to yield bulk (sphere) pair correlation functions in good agreement with computer simulation results [105], we are confident to apply it to inhomogeneous situations. We find that, driven by packing effects of the spheres, orientational order of the needles occurs at the free fluid-fluid interface, and that the density profiles are oscillatory provided the sphere-rich fluid is on the oscillatory side of the Fisher-Widom line in the bulk phase diagram [110–113]. The interface tension is found to be of the order of the thermal energy per molecular area, and we investigate its scaling with needle length and sphere diameter in detail.

Similar interface studies using density-functional approaches were recently carried out [114, 115] for the AO model [87, 88] of colloid-polymer mixtures. Our present model, however, allows to go beyond those studies through the investigation of orientational order at the interface. Clearly, such ordering is absent in the AO model of spherical bodies.

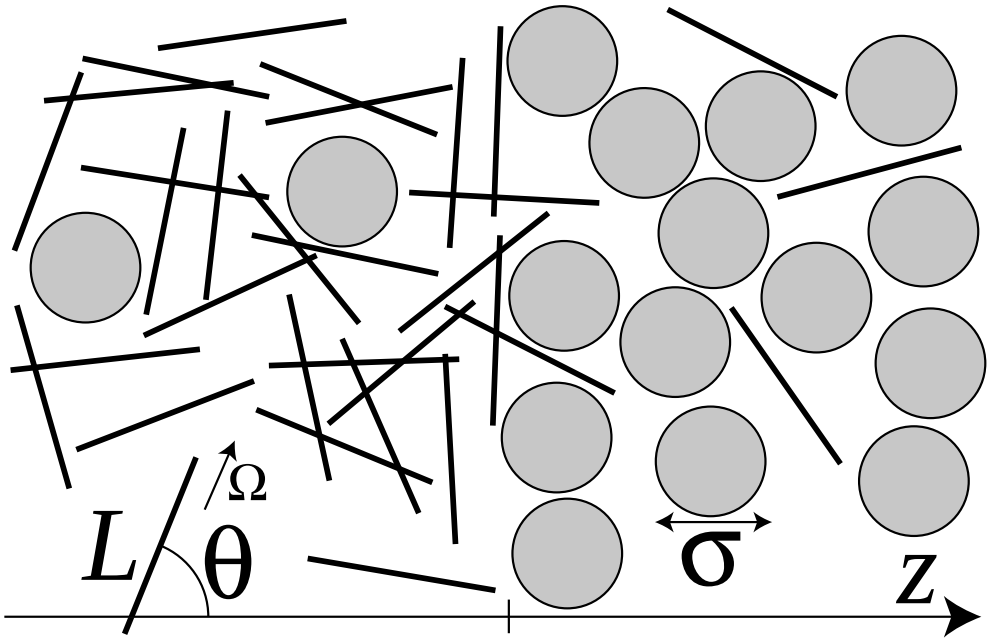


FIGURE 1. Model of hard spheres with diameter $\sigma = 2R$ and needles with length $L$. In planar geometry, the $z$-direction is perpendicular to the interface between needle-rich ($z < 0$) and sphere-rich ($z > 0$) phases. The needle orientation is denoted by $\mathbf{\Omega}$, and the angle between $\mathbf{\Omega}$ and the $z$-axis is $\vartheta$.

## 2. Model

We consider a mixture of hard spheres (species $S$) with radii $R$ and straight hard needles (species $N$) with length $L$ and diameter $D$, see Figure 1 for a sketch. The spheres interact with a hard core potential $V_{\mathrm{SS}}(r)$ as a function of their centre separation distance $r$, which is given by $V_{\mathrm{SS}}(r) = \infty$ if $r < 2R$ and zero otherwise. Spheres and needles interact with a hard body interaction that depends, due to the particle shapes, on the difference vector $\mathbf{r}$ between sphere and needle centre, as well as on the needle orientation given by a unit vector $\mathbf{\Omega}$ pointing along the needle shape. (The needles possess an inflection symmetry, $\mathbf{\Omega} \to -\mathbf{\Omega}$.) The sphere–needle interaction is given by $V_{\mathrm{SN}}(\mathbf{r}, \mathbf{\Omega}) = \infty$ if both shapes overlap, and zero otherwise.

The needles are taken to have vanishing thickness. Although these "line" particles would non-trivially collide in a dynamic description, their excluded volume vanishes due to the vanishing particle volume. Therefore, configurations of overlapping needles carry vanishing statistical weight. As we are interested in static quantities only, the needles can be regarded as an ideal gas of rotators, solely due to their geometric properties. As an aside, no such scaling holds in the somewhat similar AO model of hard sphere colloids and ideal (polymer)

*spheres*. There the interactions between the particles of the second component are regarded as being ideal from the outset.

We denote the number densities of spheres and needles by $\rho_{\mathrm{S}}(\mathbf{r})$ and $\rho_{\mathrm{N}}(\mathbf{r},\mathbf{\Omega})$, respectively. As bulk thermodynamic parameters, we use the packing fraction of spheres $\eta = 4\pi R^3\rho_{\mathrm{S}}/3$ and the scaled needle density $\rho_* = \rho_{\mathrm{N}}L^2\sigma$, where $\sigma = 2R$ denotes the sphere diameter. Furthermore, we denote the density in a reservoir of pure needles that is in chemical equilibrium with the system as $\rho_{\mathrm{N}}^{\mathrm{r}}$ and use a scaled version $\rho_*^{\mathrm{r}} = \rho_{\mathrm{N}}^{\mathrm{r}}L^2\sigma$. The ratio of needle length and sphere diameter, $L/\sigma$, is a control parameter. As only hard core interactions are present, temperature $T$ is an irrelevant variable that only sets the energy scale through $kT$, where $k$ is Boltzmann's constant.

## 3. Density functional theory

**3.1. Description of the functional.** In this section we briefly review the DFT proposed in Ref. [105]. The starting point is a geometrical representation of the particles in terms of weight functions $w_\mu^i$, where $i$ labels the species, and $\mu = 3, 2, 1, 0$ corresponds to the particles' volume, surface, integral mean curvature and Euler characteristic, respectively [101]. The weight functions are determined to give the Mayer bonds $f_{ij} = \exp(-\beta V_{ij}) - 1$, where $\beta = 1/kT$, by a linear combination of terms $w_\gamma^i(\mathbf{r}) * w_{3-\gamma}^j(\mathbf{r})$, where the star denotes the spatial convolution, $g(\mathbf{r}) * h(\mathbf{r}) = \int g(\mathbf{x})h(\mathbf{r}-\mathbf{x})\,\mathrm{d}^3x$. For needles, following Ref. [101] yields

$$w_1^{\mathrm{N}}(\mathbf{r},\mathbf{\Omega}) = \frac{1}{4}\int_{-L/2}^{L/2} \delta(\mathbf{r}+\mathbf{\Omega}\,l)\,\mathrm{d}l, \tag{4.1}$$

$$w_0^{\mathrm{N}}(\mathbf{r},\mathbf{\Omega}) = \frac{1}{2}\left[\delta(\mathbf{r}+\frac{L}{2}\mathbf{\Omega}) + \delta(\mathbf{r}-\frac{L}{2}\mathbf{\Omega})\right], \tag{4.2}$$

where $\delta(x)$ is the Dirac distribution. The function $w_1^{\mathrm{N}}$ describes the linear shape of a needle, whereas $w_0^{\mathrm{N}}$ is only non-vanishing at the needle endpoints.

For spheres the weight functions [96, 100] are

$$w_3^{\mathrm{S}}(\mathbf{r}) = \Theta(R-r), \quad w_2^{\mathrm{S}}(\mathbf{r}) = \delta(R-r), \tag{4.3}$$

$$\mathbf{w}_{\mathrm{v}2}^{\mathrm{S}}(\mathbf{r}) = w_2^{\mathrm{S}}(\mathbf{r})\,\mathbf{r}/r, \quad \hat{\mathbf{w}}_{\mathrm{m}2}^{\mathrm{S}}(\mathbf{r}) = w_2^{\mathrm{S}}(\mathbf{r})[\mathbf{rr}/r^2 - \hat{\mathbf{1}}/3], \tag{4.4}$$

where $r = |\mathbf{r}|$, $\Theta(x)$ is the Heaviside step function, $\hat{\mathbf{1}}$ is the $3\times 3$ identity matrix, and $\mathbf{rr}$ is a dyadic product. Further, linearly dependent, weights are $w_1^{\mathrm{S}}(\mathbf{r}) = w_2^{\mathrm{S}}(\mathbf{r})/(4\pi R), \mathbf{w}_{\mathrm{v}1}^{\mathrm{S}}(\mathbf{r}) = \mathbf{w}_{\mathrm{v}2}^{\mathrm{S}}(\mathbf{r})/(4\pi R), w_0^{\mathrm{S}}(\mathbf{r}) = w_1^{\mathrm{S}}(\mathbf{r})/R$. The weight functions for spheres have different tensorial rank: $w_0^{\mathrm{S}}$, $w_1^{\mathrm{S}}$, $w_2^{\mathrm{S}}$, $w_3^{\mathrm{S}}$ are scalars; $\mathbf{w}_{\mathrm{v}1}^{\mathrm{S}}$, $\mathbf{w}_{\mathrm{v}2}^{\mathrm{S}}$ are vectors; $\hat{\mathbf{w}}_{\mathrm{m}2}^{\mathrm{S}}$ is a (traceless) second-rank tensor. The Mayer bond between pairs of spheres is obtained through $-f_{\mathrm{SS}}/2 = w_3^{\mathrm{S}} * w_0^{\mathrm{S}} + w_2^{\mathrm{S}} * w_1^{\mathrm{S}} - \mathbf{w}_{\mathrm{v}2}^{\mathrm{S}} * \mathbf{w}_{\mathrm{v}1}^{\mathrm{S}}$

[96]. In order to recover the sphere-needle Mayer bond one uses [105]

$$w_2^{\mathrm{SN}}(\mathbf{r},\mathbf{\Omega}) = 2|\mathbf{w}_{\mathrm{v2}}^{\mathrm{S}}(\mathbf{r})\cdot\mathbf{\Omega}|, \tag{4.5}$$

which contains information about both species: it is non-vanishing on the surface of a sphere with radius $R$, but also possesses (needle) orientation–dependence. This function allows us to generate the Mayer bond through $-f_{\mathrm{SN}}(\mathbf{r},\mathbf{\Omega}) = w_3^{\mathrm{S}}(\mathbf{r}) * w_0^{\mathrm{N}}(\mathbf{r},\mathbf{\Omega}) + w_2^{\mathrm{SN}}(\mathbf{r},\mathbf{\Omega}) * w_1^{\mathrm{N}}(\mathbf{r},\mathbf{\Omega})$ as follows.

We take the difference vector between the centres of mass of needle and sphere to lie in the equatorial plane: $\mathbf{r} = (r\sin\varphi, r\cos\varphi, 0)$. Due to the rotational symmetry, we can choose the needle to be aligned parallel to the $y$-axis: $\mathbf{\Omega} = (0,1,0)$. Then,

$$\begin{aligned} &w_3^{\mathrm{S}}(\mathbf{r}) * w_0^{\mathrm{N}}(\mathbf{r},\mathbf{\Omega}) \\ &\quad= \frac{1}{2}\int_0^\infty\int_0^{2\pi}\int_0^{\pi}\Theta(R-r')\sum_{\pm}\delta(r\sin\varphi - r'\sin\vartheta'\sin\varphi') \\ &\qquad\times\delta\Big(r\cos\varphi - r'\sin\vartheta'\cos\varphi' \pm \frac{L}{2}\Big)\delta(-r'\cos\vartheta')r'^2\sin\vartheta'\,\mathrm{d}\varphi'\,\mathrm{d}\vartheta'\,\mathrm{d}r' \end{aligned} \tag{4.6}$$

$$= \frac{1}{2}\sum_{\pm}\Theta\Big(R^2 - r^2 - \frac{L^2}{4} \pm Lr\cos\varphi\Big), \tag{4.7}$$

and

$$\begin{aligned} &w_2^{\mathrm{SN}}(\mathbf{r},\mathbf{\Omega}) * w_1^{\mathrm{N}}(\mathbf{r},\mathbf{\Omega}) \\ &\quad= \frac{1}{2}\int_0^\infty\int_0^{2\pi}\int_0^{\pi}\Big|\begin{pmatrix}\sin\vartheta'\sin\varphi'\\ \sin\vartheta'\cos\varphi'\\ \cos\vartheta'\end{pmatrix}\cdot\begin{pmatrix}0\\1\\0\end{pmatrix}\Big|\delta(R-r') \\ &\qquad\times\int_{-L/2}^{L/2}\delta(r\sin\varphi - r'\sin\vartheta'\sin\varphi')\delta(r\cos\varphi - r'\sin\vartheta'\cos\varphi' + l) \\ &\qquad\times\delta(-r'\cos\vartheta')\,\mathrm{d}l\,r'^2\sin\vartheta'\,\mathrm{d}\vartheta'\,\mathrm{d}\varphi'\,\mathrm{d}r' \end{aligned} \tag{4.8}$$

$$= \frac{1}{2}\sum_{\pm}\Theta(R - |r\sin\varphi|)\Theta\Big(\frac{L}{2} - |r\cos\varphi \pm \sqrt{R^2 - r^2\sin^2\varphi}|\Big), \tag{4.9}$$

where the integrals over $\vartheta'$, $r'$, and $l$ in Eqs. (4.6,4.8) are straightforward. The integral over $\varphi$ is split into two domains: for $0 < \varphi < \pi$, $\sin\varphi$ is positive, while for $\pi < \varphi < 2\pi$ it is negative. The sum of Eqs. (4.7,4.9) represents the (negative) Mayer bond between sphere and needle, i.e. $-f_{\mathrm{SN}} = w_3^{\mathrm{S}} * w_0^{\mathrm{N}} + w_2^{\mathrm{SN}} * w_1^{\mathrm{N}}$. This can be seen by considering the cases where the above expressions are non-vanishing: In Eq. (4.7), the step function counts the number of needle endpoints that lie in the sphere. In Eq. (4.9) the first step function is non-zero only if the needle axis

intersects the sphere. If it does, the second step function counts how often the needle intersects the surface of the sphere. This covers all cases of sphere–needle overlap.

All weight functions are used to obtain weighted densities $n_\nu^i$ by smoothing the actual density profiles through spatial convolutions,

$$n_\nu^{\mathrm{N}}(\mathbf{r},\mathbf{\Omega}) = \rho_{\mathrm{N}}(\mathbf{r},\mathbf{\Omega}) * w_\nu^{\mathrm{N}}(\mathbf{r},\mathbf{\Omega}), \quad \nu = 1,0, \tag{4.10}$$

$$n_\nu^{\mathrm{S}}(\mathbf{r}) = \rho_{\mathrm{S}}(\mathbf{r}) * w_\nu^{\mathrm{S}}(\mathbf{r}), \quad \nu = 3,2,1,0,\mathrm{v2},\mathrm{v1},\mathrm{m2}, \tag{4.11}$$

$$n_2^{\mathrm{SN}}(\mathbf{r},\mathbf{\Omega}) = \rho_{\mathrm{S}}(\mathbf{r}) * w_2^{\mathrm{SN}}(\mathbf{r},\mathbf{\Omega}). \tag{4.12}$$

Note that $n_\nu^{\mathrm{N}}$ and $n_\nu^{\mathrm{S}}$ are *pure* weighted densities, involving only variables of either species [96,100,101]. The function $n_2^{\mathrm{SN}}$ is obtained as a convolution of the sphere density with an orientation-dependent weight function; hence it combines characteristics of both species and couples the orientational degrees of freedom of the needles to the sphere distribution.

The (Helmholtz) excess free energy is obtained by integrating over a free energy density,

$$F_{\mathrm{exc}}[\rho_{\mathrm{S}},\rho_{\mathrm{N}}] = \frac{kT}{4\pi}\iint \Phi\left(\{n_\nu^i\}\right)\,\mathrm{d}^3r\,\mathrm{d}^2\Omega, \tag{4.13}$$

where the reduced free energy density $\Phi$ is a simple function (not a functional) of the weighted densities $n_\nu^i$. The variable $\mathbf{r}$ runs over space, and as $\Phi$ depends also on orientation, $\mathbf{\Omega}$ runs over the unit sphere. The functional form of $\Phi$ is obtained by consideration of the exact zero-dimensional excess free energy [105], and is given by

$$\Phi = \Phi_{\mathrm{S}} + \Phi_{\mathrm{SN}}, \tag{4.14}$$

$$\begin{aligned}\Phi_{\mathrm{S}} = {} & -n_0^{\mathrm{S}}\ln(1-n_3^{\mathrm{S}}) + \frac{n_1^{\mathrm{S}}n_2^{\mathrm{S}} - \mathbf{n}_{\mathrm{v1}}^{\mathrm{S}}\cdot\mathbf{n}_{\mathrm{v2}}^{\mathrm{S}}}{1-n_3^{\mathrm{S}}} \\ & + \frac{\frac{1}{3}\left(n_2^{\mathrm{S}}\right)^3 - n_2^{\mathrm{S}}\left(\mathbf{n}_{\mathrm{v2}}^{\mathrm{S}}\right)^2 + \frac{3}{2}\left(\mathbf{n}_{\mathrm{v2}}^{\mathrm{S}}\hat{\mathbf{n}}_{\mathrm{m2}}^{\mathrm{S}}\mathbf{n}_{\mathrm{v2}}^{\mathrm{S}} - 3\det\hat{\mathbf{n}}_{\mathrm{m2}}^{\mathrm{S}}\right)}{8\pi(1-n_3^{\mathrm{S}})^2},\end{aligned} \tag{4.15}$$

$$\Phi_{\mathrm{SN}} = -n_0^{\mathrm{N}}\ln(1-n_3^{\mathrm{S}}) + \frac{n_1^{\mathrm{N}}n_2^{\mathrm{SN}}}{1-n_3^{\mathrm{S}}}. \tag{4.16}$$

The contribution $\Phi_{\mathrm{S}}$ is equal to the pure HS case [96,100], and $\Phi_{\mathrm{SN}}$ arises from needle-sphere interactions [105]. The arguments of the weighted densities are suppressed in the notation in Eqs. (4.15,4.16); see Eqs. (4.10-4.12) for the explicit dependence. This completes the prescription for the excess free energy functional for the case of vanishingly thin needles. For completeness, the ideal free energy

is

$$F_{\mathrm{id}}[\rho_{\mathrm{S}},\rho_{\mathrm{N}}] = kT\int \rho_{\mathrm{S}}(\mathbf{r})[\ln(\rho_{\mathrm{S}}(\mathbf{r})\Lambda_{\mathrm{S}}^3)-1]\,\mathrm{d}^3r + \frac{kT}{4\pi}\iint \rho_{\mathrm{N}}(\mathbf{r},\mathbf{\Omega})[\ln(\rho_{\mathrm{N}}(\mathbf{r},\mathbf{\Omega})\Lambda_{\mathrm{N}}^3)-1]\,\mathrm{d}^3r\,\mathrm{d}^2\Omega, \quad (4.17)$$

where $\Lambda_i$ is the (irrelevant) thermal wavelength of species $i = S, N$.

## 4. Planar geometry

In a fully inhomogeneous situation, the density profiles depend on three space coordinates. In addition, the needle density profiles depend on two orientation parameters, making for a total of five parameters. When applying the density functional to such a scenario, storage and computation requirements are therefore high. If, however, the density profiles can be assumed to depend only on a few parameters, this situation changes. The remaining parameters can then be integrated out analytically, yielding *effective weight functions* that are easy to handle numerically together with effectively one-dimensional density profiles.

In order to facilitate the application of the theory to situations like the free interface considered below in Secs. 6.2 and 6.3 and to planar wall problems, we give explicit expressions for the weight functions in situations depending on a single spatial coordinate $z$ and possessing translational invariance in the $x$ and $y$ directions, where $\mathbf{r} = (x, y, z)$ is a Cartesian coordinate system. Additionally, we assume invariance with respect to rotations around the $z$-axis by an angle $\varphi$. The remaining relevant angle $\vartheta$ is that between an orientation $\mathbf{\Omega}$ and the $z$-axis, see Figure 1 on page 39. Hence $\rho_{\mathrm{S}}(\mathbf{r}) = \rho_{\mathrm{S}}(z)$, and $\rho_{\mathrm{N}}(\mathbf{r},\mathbf{\Omega}) = \rho_{\mathrm{N}}(z,\vartheta)$. Due to the inflection symmetry of the needles, considering $\vartheta \in [0, \pi/2]$ is sufficient, In this *planar geometry* the weighted densities, Eqs. (4.10-4.12), can be expressed as

$$n_\nu^{\mathrm{N}}(z,\vartheta) = \int \rho_{\mathrm{N}}(z',\vartheta) w_\nu^{\mathrm{N}}(z-z',\vartheta)\,\mathrm{d}z' \quad (4.18)$$

$$n_\nu^{\mathrm{S}}(z) = \int \rho_{\mathrm{S}}(z') w_\nu^{\mathrm{S}}(z-z')\,\mathrm{d}z' \quad (4.19)$$

$$n_2^{\mathrm{SN}}(z,\vartheta) = \int \rho_{\mathrm{S}}(z') w_2^{\mathrm{SN}}(z-z',\vartheta)\,\mathrm{d}z', \quad (4.20)$$

where the effective weight functions $w_\nu^{\mathrm{N}}(z,\vartheta), w_\nu^{\mathrm{S}}(z), w_2^{\mathrm{SN}}(z,\vartheta)$ are obtained by carrying out the integrations in Eqs. (4.10-4.12) over coordinates $x, y$:

$$w_\nu^{\mathrm{N}}(z,\vartheta) = \int_{-\infty}^{\infty}\int_{-\infty}^{\infty} w_\nu^{\mathrm{N}}(\mathbf{r},\mathbf{\Omega})\,\mathrm{d}x\,\mathrm{d}y \tag{4.21}$$

$$w_\nu^{\mathrm{S}}(z) = \int_{-\infty}^{\infty}\int_{-\infty}^{\infty} w_\nu^{\mathrm{S}}(\mathbf{r})\,\mathrm{d}x\,\mathrm{d}y \tag{4.22}$$

$$w_2^{\mathrm{SN}}(z,\vartheta) = \int_{-\infty}^{\infty}\int_{-\infty}^{\infty} w_2^{\mathrm{SN}}(\mathbf{r},\mathbf{\Omega})\,\mathrm{d}x\,\mathrm{d}y, \tag{4.23}$$

where $\mathbf{r} = (x, y, z)$. In the following, we employ cylindrical coordinates $\mathbf{r} = (r\cos\varphi, r\sin\varphi, z)$.

Explicitly, for the needles one obtains

$$w_1^{\mathrm{N}}(z,\vartheta) = \frac{1}{4\cos\vartheta}\Theta\Big(\frac{L}{2}\cos\vartheta - |z|\Big), \tag{4.24}$$

$$w_0^{\mathrm{N}}(z,\vartheta) = \frac{1}{2}\delta\Big(\frac{L}{2}\cos\vartheta - |z|\Big). \tag{4.25}$$

For the spheres

$$w_3^{\mathrm{S}}(z) = \pi(R^2 - z^2)\Theta(R - |z|), \tag{4.26}$$

$$w_2^{\mathrm{S}}(z) = 2\pi R\Theta(R - |z|), \tag{4.27}$$

$$\mathbf{w}_{\mathrm{v}2}^{\mathrm{S}}(z) = 2\pi z\Theta(R - |z|)\mathbf{e}_z, \tag{4.28}$$

$$\hat{\mathbf{w}}_{\mathrm{m}2}^{\mathrm{S}}(z) = \pi\Big(\frac{z^2}{R} - \frac{R}{3}\Big)\Theta(R - |z|)\,\mathrm{diag}(-1,-1,2), \tag{4.29}$$

where $\mathbf{e}_z$ is the unit vector pointing along the $z$-axis and $\mathrm{diag}(\cdot)$ denotes a $3\times 3$ diagonal matrix. The linearly dependent weight functions are $w_1^{\mathrm{S}}(z) = \Theta(R - |z|)/2$, $w_0^{\mathrm{S}}(z) = \Theta(R - |z|)\,/(2R)$, $\mathbf{w}_{\mathrm{v}1}^{\mathrm{S}}(z) = z\Theta(R - |z|)\,\mathbf{e}_z/(2R)$. Finally, the mixed weight function is obtained as

$$w_2^{\mathrm{SN}}(z,\vartheta) = \begin{cases} 8\sqrt{R^2\sin^2\vartheta - z^2} & \\ \quad +8z\cos\vartheta & \\ \quad\quad \times \arcsin\Big(\frac{z\cot(\vartheta)}{\sqrt{R^2-z^2}}\Big) & \text{if } |z| < R\sin\vartheta \\ 4\pi|z|\cos\vartheta & \text{if } R\sin\vartheta \le |z| \le R \\ 0 & \text{else.} \end{cases} \tag{4.30}$$

For the scalar and vectorial sphere weight functions [Eqs. (4.3,4.4)] as well as for the pure needle weight functions [Eqs. (4.1,4.2)] the integrations in (4.21,4.22) are straightforward and yield the results given in Eqs. (4.24-4.28). The calculations for $\hat{\mathbf{w}}_{\mathrm{m}2}^{\mathrm{S}}(z)$ and $w_2^{\mathrm{SN}}(z,\vartheta)$ [defined through Eqs. (4.4) and (4.5), respectively] are slightly more involved, and are given explicitly in the following subsections.

**4.1. Tensor sphere weight function.** We insert the definition of the tensor weight [Eq. (4.4)] into Eq. (4.22),

$$\hat{\mathbf{w}}^{\mathrm{S}}_{\mathrm{m}2}(z) = \int_{-\infty}^{\infty}\int_{-\infty}^{\infty} \delta(R-|\mathbf{r}|)\left(\frac{\mathbf{rr}}{r^2}-\frac{\hat{\mathbf{1}}}{3}\right)\mathrm{d}x\,\mathrm{d}y \tag{4.31}$$

$$\begin{aligned}
&= \int_0^{2\pi}\int_0^{\infty} \delta\Big(R-\sqrt{r^2+z^2}\Big) \\
&\quad\times\left[\frac{1}{r^2+z^2}\begin{pmatrix} r^2\sin^2\varphi & r^2\sin\varphi\cos\varphi & r\sin\varphi z \\ r^2\sin\varphi\cos\varphi & r^2\cos^2\varphi & r\cos\varphi z \\ r\sin\varphi z & r\cos\varphi z & z^2\end{pmatrix}\right. \\
&\qquad\left.-\frac{\hat{\mathbf{1}}}{3}\right]\mathrm{d}\varphi\, r\,\mathrm{d}r
\end{aligned} \tag{4.32}$$

$$\begin{aligned}
&= \int_0^{\infty} \delta\Big(R-\sqrt{r^2+z^2}\Big) \\
&\quad\times\left(\frac{1}{r^2+z^2}\,\mathrm{diag}(\pi r^2,\pi r^2,2z^2)-\frac{2\pi}{3}\hat{\mathbf{1}}\right) r\,\mathrm{d}r
\end{aligned} \tag{4.33}$$

$$= \left(\frac{\pi}{R}\,\mathrm{diag}(R^2-z^2,R^2-z^2,2z^2)-\frac{2\pi R}{3}\hat{\mathbf{1}}\right)\Theta(R^2-z^2), \tag{4.34}$$

from which Eq. (4.29) can be readily obtained. The off-diagonal elements in Eq. (4.32) vanish due to the $\varphi$-integration over a complete wavelength, and to obtain Eq. (4.34) we have used $\delta(f(x)) = |f'(x_0)|^{-1}\delta(x-x_0)$, where $x_0$ is the zero of $f(x)$, i.e. $f(x_0)=0$.

**4.2. Mixed sphere-needle weight function.** Due to the rotational symmetry around the $z$-axis, we can take $\mathbf{\Omega} = (\sin\vartheta, 0, \cos\vartheta)$, and due to the inflection symmetry of the needles, we can restrict ourselves to $0 \le \vartheta \le \pi/2$. By inserting the definition of the mixed weight function [Eq. (4.5)] into Eq. (4.23) we obtain

$$w_2^{\mathrm{SN}}(z,\vartheta) = 2\iint\left|\delta\Big(R-|\mathbf{r}|\Big)\frac{1}{\sqrt{r^2+z^2}}\tbinom{r\cos\varphi}{r\sin\varphi}{z}\cdot\tbinom{\sin\vartheta}{0}{\cos\vartheta}\right|\mathrm{d}x\,\mathrm{d}y \tag{4.35}$$

$$= 2\int_0^{2\pi}\int_0^{\infty}\left|\delta\Big(R-\sqrt{r^2+z^2}\Big)\frac{z\cos\vartheta + r\cos\varphi\sin\vartheta}{\sqrt{r^2+z^2}}\right| r\,\mathrm{d}r\,\mathrm{d}\varphi \tag{4.36}$$

$$
\begin{aligned}
&= \Bigg\{ \Bigg[ 8\sqrt{(R^2 - z^2)\sin^2\vartheta - z^2\cos^2\vartheta} \\
&\qquad + 4z\cos\vartheta\ \operatorname{sgn}\big(\sqrt{R^2 - z^2}\sin\vartheta\big) \arcsin\left(\frac{z\cos\vartheta}{\sqrt{R^2 - z^2}\sin\vartheta}\right)\Bigg] \\
&\qquad\quad \times \Theta\left(1 - \Big|\frac{z\cos\vartheta}{\sqrt{R^2 - z^2}\sin\vartheta}\Big|\right) \\
&\quad + 4\pi|z\cos\vartheta|\Theta\left(\Big|\frac{z\cos\vartheta}{\sqrt{R^2 - z^2}\sin\vartheta}\Big| - 1\right)\Bigg\}\Theta(R - |z|)
\end{aligned}
\tag{4.37}
$$

$$
= \begin{cases}
8\sqrt{R^2\sin^2\vartheta - z^2} & \\
\qquad +8z\cos\vartheta\arcsin\left(\frac{z\cot\vartheta}{\sqrt{R^2 - z^2}}\right) & \text{if } |z| < R\sin\vartheta \\
4\pi|z|\cos\vartheta & \text{if } R\sin\vartheta \le |z| \le R \\
0 & \text{else.}
\end{cases}
\tag{4.38}
$$

In Eq. (4.36), we have used the same representation for the Dirac distribution as before. The non-trivial part is the integral over $\varphi$, which we discuss in the following. It is of the form

$$
\int_0^{2\pi} |a + b\cos\varphi|\, d\varphi
$$

with constants (with respect to $\varphi$) $a, b$. Due to the symmetry of the cosine function, the integration from 0 to $\pi$ yields the same result as that from $\pi$ to $2\pi$. We consider two cases: The argument of $|\cdot|$ changes its sign once if $|a/b| < 1$, and we have

$$
\begin{aligned}
&\int_0^{\pi} |a + b\cos\varphi|\, d\varphi \\
&\quad = \operatorname{sgn}(a+b)\Big(\big[a\varphi + b\sin\varphi\big]_0^x + \big[-a\varphi - b\sin\varphi\big]_x^{\pi}\Big) && (4.39)\\
&\quad = \operatorname{sgn}(b)(2b\sin x + 2ax - a\pi) && (4.40)\\
&\quad = \operatorname{sgn}(b)\Big(2b\sin\arccos\frac{-a}{b} + 2a\arccos\frac{-a}{b} - a\pi\Big) && (4.41)\\
&\quad = 2\sqrt{b^2 - a^2} + 2a\ \operatorname{sgn}(b)\arcsin\frac{a}{b}, && (4.42)
\end{aligned}
$$

where $x = \arccos(-a/b)$. If, on the other hand, $|a/b| > 1$, the argument does not change its sign. Then, $|a + b\cos\varphi| = (a + b\cos\varphi)\operatorname{sgn}(a)$:

$$
\int_0^{\pi} |a + b\cos\varphi|\, d\varphi = |a|\pi. \tag{4.43}
$$

Note that in Eq. (4.37), $\mathrm{sgn}(\cdot) = +1$ holds since $0 \leq \vartheta \leq \pi/2$.

This fully specifies the DFT in planar geometry. We note that the tensorial weight function, Eq. (4.29), is included for reasons of completeness. Albeit being crucial for a reliable description of the solid [100], it is known to yield a small contribution to the free energy in planar geometry, and may be neglected to a good approximation. We will adopt this strategy in Sec. 6 below.

## 5. Spherical geometry

Here we focus on situations that only depend on the distance to the origin, $r$, and that remain invariant under rotations around the origin. This is realised e.g. in the important test-particle limit that allows to obtain pair distribution functions by minimising the functional in the presence of a test sphere fixed at the origin. In spherical geometry, only the angle $\vartheta$ between needle orientation $\mathbf{\Omega}$ and position $\mathbf{r}$ remains relevant, and $\rho_{\mathrm{S}}(\mathbf{r}) = \rho_{\mathrm{S}}(r)$, and $\rho_{\mathrm{N}}(\mathbf{r}, \mathbf{\Omega}) = \rho_{\mathrm{N}}(r, \vartheta)$. Again, we can restrict ourselves to $0 \leq \vartheta \leq \pi/2$. The pure weighted densities, Eqs. (4.10-4.12) can be expressed as

$$n_\nu^{\mathrm{N}}(r, \vartheta) = \int_0^\infty \rho_{\mathrm{N}}(r', \vartheta) w_\nu^{\mathrm{N}}(r, r', \vartheta)\, \mathrm{d}r', \tag{4.44}$$

$$n_\nu^{\mathrm{S}}(r) = \int_0^\infty \rho_{\mathrm{S}}(r') w_\nu^{\mathrm{S}}(r, r')\, \mathrm{d}r', \tag{4.45}$$

where the reduced weight functions are

$$w_1^{\mathrm{N}}(r, r', \vartheta) = \frac{r'}{4\sqrt{r'^2 - r^2 \sin^2\vartheta}} \times \sum_\pm \Theta\Big(\frac{L}{2} - \Big|r\cos\vartheta \pm \sqrt{r'^2 - r^2\sin^2\vartheta}\Big|\Big), \tag{4.46}$$

$$w_0^{\mathrm{N}}(r, r', \vartheta) = \frac{1}{2}\sum_\pm \delta\left(r' - \sqrt{\Big(r \pm \frac{L}{2}\cos\vartheta\Big)^2 + \frac{L^2}{4}\sin^2\vartheta}\right), \tag{4.47}$$

$$w_3^{\mathrm{S}}(r, r') = \frac{\pi r'}{r}\big[R^2 - (r - r')^2\big]\Theta\big(R - |r - r'|\big), \tag{4.48}$$

$$w_2^{\mathrm{S}}(r, r') = \frac{2\pi R r'}{r}\Big[\Theta(R - |r - r'|) - \Theta(R - r - r')\Big], \tag{4.49}$$

$$\mathbf{w}_{\mathrm{v}2}^{\mathrm{S}}(r, r') = \frac{R^2 + r^2 - r'^2}{2Rr} w_2^S(r, r')\frac{\mathbf{r}}{r}, \tag{4.50}$$

$$\hat{\mathbf{w}}_{\mathrm{m}2}^{\mathrm{S}}(r, r') = \frac{1}{2}\left[\left(\frac{R^2 + r^2 - r'^2}{2Rr}\right)^2 - \frac{1}{3}\right] w_2^{\mathrm{S}}(r, r')\left(3\frac{\mathbf{rr}}{r^2} - \hat{\mathbf{1}}\right). \tag{4.51}$$

In Eqs. (4.50,4.51) only the dependence on the scalar argument $r$ is important; the dependence on $\mathbf{r}/r$ is trivial due to the structure of $\Phi$, Eq. (4.15). The linearly dependent weight functions are

$$w_1^{\mathrm{S}}(r,r') = \frac{r'}{2r}[\Theta(R-|r-r'|)-\Theta(R-r-r')], \tag{4.52}$$

$$\mathbf{w}_{\mathrm{v1}}^{\mathrm{S}}(r,r') = \frac{r^2-r'^2+R^2}{2Rr} w_1^{\mathrm{S}}(r,r'), \tag{4.53}$$

$$w_0^{\mathrm{S}}(r,r') = \frac{r'}{2Rr}[\Theta(R-|r-r'|)-\Theta(R-r-r')]. \tag{4.54}$$

The mixed weight function is

$$w_2^{\mathrm{SN}}(r,r',\vartheta) = \begin{cases} \frac{8r'}{r}\Big[\sqrt{r'^2(1-u^2)-R^2\cos^2\vartheta} \\ \qquad +(r-r'u)\cos(\vartheta)\arcsin\left(\frac{(r-r'u)\cot\vartheta}{r'\sqrt{1-u^2}}\right)\Big] \\ \qquad\qquad\qquad\qquad \text{if } |r-r'u| < r'\sqrt{1-u^2}\tan\vartheta \\ 4\pi(r'/r)|r-r'u|\cos\vartheta \qquad \text{if } |r-r'u| \geq r'\sqrt{1-u^2}\tan\vartheta \\ 0 \qquad\qquad\qquad\qquad\qquad\quad \text{if } |u|\geq 1, \end{cases} \tag{4.55}$$

where $u = (r'^2+r^2-R^2)/(2rr')$.

We note that the for a test-particle limit calculation, where a hard sphere is fixed at the origin, the above expression can be simplified, as the density distributions vanish inside the test particle. This allows one to omit the second step-function in Eq. (4.49) and rewrite the convolution kernels for spheres as a function of the difference $r-r'$ only. The expressions given above are completely general and apply also to cases of non-vanishing densities in the immediate vicinity of the origin.

## 6. Applications

As an example of how to utilise this density functional to perform explicit calculations in an inhomogeneous situation, we present the treatment of the free fluid–fluid interface by Brader *et al.* [116].

**6.1. Bulk phase diagram.** As a prerequisite for the interface study, we reconsider the bulk fluid demixing phase diagram of hard spheres and vanishingly thin needles. Within our approach, this is obtained from the bulk Helmholtz free energy, which in turn is obtained by applying the density functional (outlined in Sec. 3.1) to constant density fields of spheres and needles. Then, the weighted densities become proportional to the respective bulk densities, $n_\nu^i = \xi_\nu^i \rho_i$, where the proportionality constants are fundamental measures given by $\xi_\nu^i = \int w_\nu^i \,\mathrm{d}^3x$. For spheres $\xi_3^{\mathrm{S}} = 4\pi R^3/3, \xi_2^{\mathrm{S}} = \xi_2^{\mathrm{SN}} = 4\pi R^2, \xi_1^{\mathrm{S}} = R, \xi_0^{\mathrm{S}} = 1$, whereas for needles

$\xi_1^{\rm N} = L/4, \xi_0^{\rm N} = 1$. Then the excess Helmholtz free energy per volume $V$ is given by $F_{\rm exc}(\rho_{\rm S}, \rho_{\rm N})/V = \phi_{\rm HS}(\rho_{\rm S}) - \rho_{\rm N} kT \ln \alpha(\rho_{\rm S})$, where $\phi_{\rm HS}(\rho_{\rm S})$ is the excess free energy density of pure hard spheres in the scaled-particle (and Percus-Yevick compressibility) approximation and $\alpha = (1-\eta_{\rm S}) \exp[-(3/2)(L/\sigma)\eta_{\rm S}/(1-\eta_{\rm S})]$. This expression for the free energy is identical to the result from the perturbation theory of Bolhuis and Frenkel [86]. We note that this is also equivalent to a straightforward application of scaled-particle theory for non-spherical bodies [117] to the current model. From the free energy all thermodynamic quantities can be calculated, and equating the total pressure and the chemical potentials of both species in both phases yields the coexisting densities. The resulting binodal was found to be in remarkable agreement with simulation results [86].

Here we consider the case of equal sphere diameter and needle length, $\sigma = L$, where fluid-fluid phase separation is stable with respect to freezing [86] and display the phase diagram in system representation (as a function of $\eta$ and $\rho_*$) in Figure 2. Shown is the binodal for coexisting states, where a sphere-rich and needle-poor fluid (sphere liquid) coexists with a sphere-poor and needle-rich fluid (sphere gas). For low densities, the density discontinuity vanishes at a critical point. We also display the Fisher-Widom (FW) line, which separates regimes in the phase diagram where the ultimate decay of pair correlation functions (and inhomogeneous one-body density profiles) at large separation is either damped oscillatory or monotonic [110–113]. The FW line was calculated for the present model in Ref. [105] by considering the poles of the partial structure factors in the plane of complex wavevectors [111, 112]. Furthermore, we display four tielines between coexisting fluid states. These belong to reservoir densities of needles $\rho_*^{\rm r} = 16, 18, 20, 22$, and indicate the states where we will carry out detailed structural studies below. Tielines are horizontal in the phase diagram in needle reservoir representation (as a function of $\eta$ and $\rho_*^{\rm r}$), see the inset in Figure 2. The smallest reservoir density, $\rho_*^{\rm r} = 16$, is close to the critical point (which is located at $\eta_{\rm S} = 0.15767$, $\rho_* = 9.3141$, $\rho_*^{\rm r} = 14.642$). For $\rho_*^{\rm r} = 16$ the liquid density is located well on the monotonic side of the FW line, hence we expect one-body interface profiles to decay monotonically into both bulk phases. The set of the three higher reservoir densities ($\rho_*^{\rm r} = 18, 20, 22$) covers the region up to the triple point, which was located with perturbation theory at $\rho_*^{\rm r} \approx 24$ [86]. For these states we expect damped oscillatory profiles on the sphere-rich side of the interface.

**6.2. Structure of the fluid-fluid interface.** Here we aim at an understanding of the free interface between demixed fluid states, see Figure 1 on page 39 for a schematic sketch of the following situation: Two demixed bulk fluids are in equilibrium in contact; the coordinate perpendicular to their (planar) interface is denoted $z$, and the sphere-poor (-rich) phase is present for negative (positive) $z$-values. The coordinate origin (in $z$) is set to the position of the Gibbs dividing surface, i.e. the $z$-coordinate fulfils $\int_{-\infty}^{0} [\rho_{\rm S}(z) - \rho_{\rm S}(-\infty)]\, {\rm d}z + \int_{0}^{\infty} [\rho_{\rm S}(z) -$

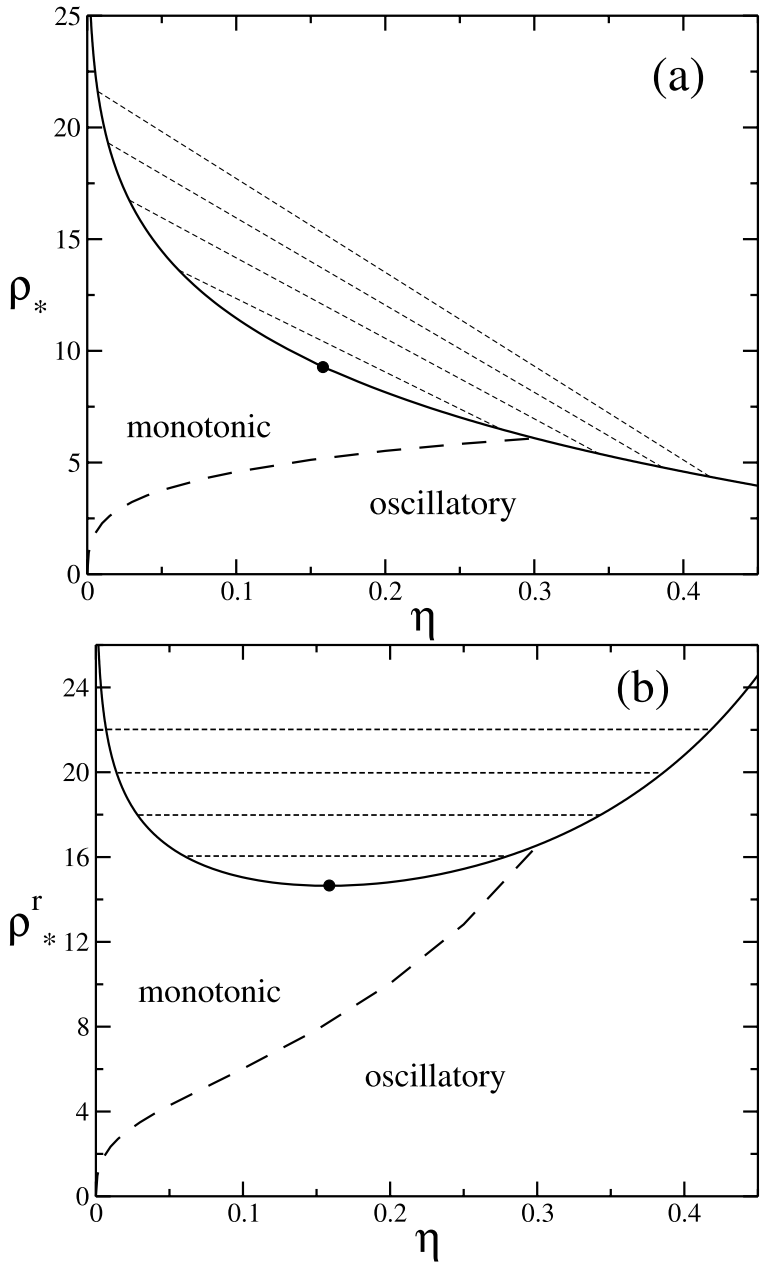


FIGURE 2. Fluid–fluid demixing phase diagram of the mixture of hard spheres and vanishingly thin needles with size ratio $L/\sigma = 1$ obtained from DFT. Shown are the binodal (solid line) and the Fisher-Widom line (dashed) dividing states where the ultimate decay of correlation functions is either monotonic or damped oscillatory. Tielines (short-dashed) between coexisting states are shown for $\rho_*^{\mathrm{r}} = 16, 18, 20, 22$. a) system representation with $\eta$ and $\rho_*$; b) reservoir representation with $\eta$ and $\rho_*^{\mathrm{r}}$.

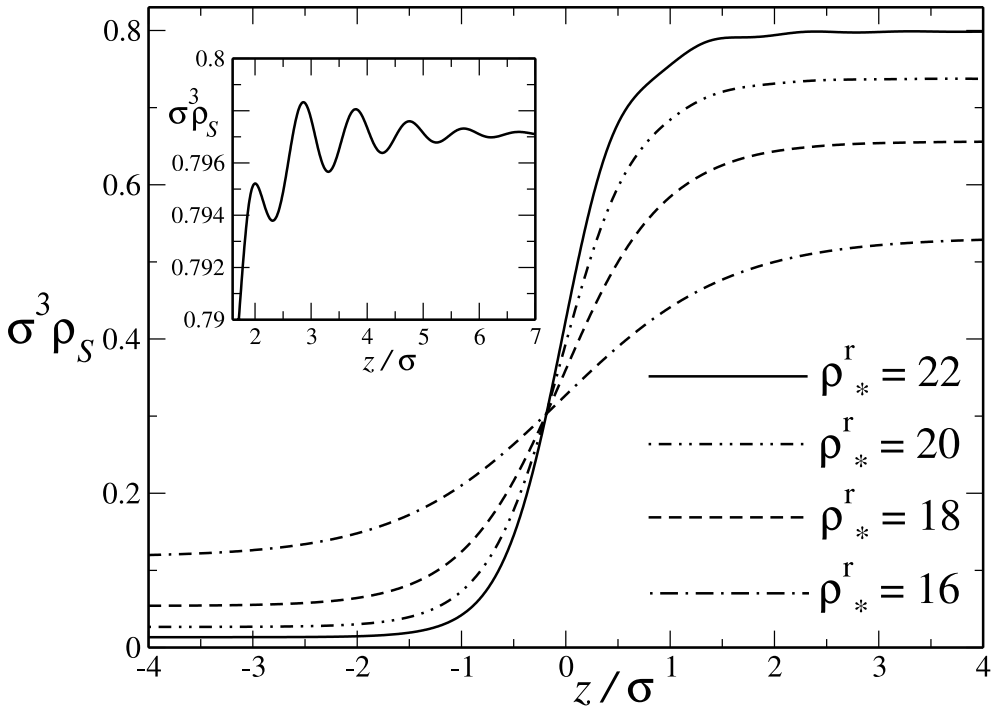


FIGURE 3. Scaled sphere density profiles $\sigma^3\rho_{\rm S}(z)$ at the free interface between sphere-poor ($z<0$) and sphere-rich ($z>0$) phases as a function of the scaled distance $z/\sigma$ perpendicular to the interface for $\rho^{\rm r}_* = 16, 18, 20, 22$ corresponding to the tielines in the phase diagram, Fig. 2. The inset shows a magnified view of the (oscillatory) profile $\sigma^3\rho(z)$ as a function of $z/\sigma$ at the sphere-rich side for $\rho^{\rm r}_* = 22$.

$\rho_{\rm S}(\infty)]\,{\rm d}z = 0$. Note that as we deal with isotropic states for $z \to \pm\infty$, the planar geometry considered in Sec. 4 applies.

The numerical minimisation of the density functional of Sec. 3.1 is done by an iteration technique, see e.g. [118]. We discretise $\rho_{\rm S}(z)$ and $\rho_{\rm N}(z,\vartheta)$ in $z$-direction with a resolution of $0.01\,\sigma$, and we find that angular discretisation in 20-50 steps are sufficient to get reliable results for density profiles. For the calculation of interface tensions between demixed fluids (Sec. 6.3), we use 120 steps. Note that when, say, 20 needle orientations are considered, we are dealing in effect (due to the additional sphere profile) with a 21 component mixture.

We choose the size ratio $\sigma/L = 1$ for our interface study. This is of the same order as realised in the experiments [85] with silica spheres of 78 nm diameter and polymer rods (PBLG) with $L = 70\,$nm. However, we disregard effects arising from rod flexibility and finite rod thickness and hence consider only $D = 0$ (note that $D = 1.6\,$nm for the polymer in [85]). We first turn to the sphere density profiles, $\rho_{\rm S}(z)$, displayed in Figure 3 as a function of the scaled distance $z/\sigma$

for scaled needle reservoir densities $\rho_*^{\mathrm{r}} = 16, 18, 20, 22$. These state points are indicated by tielines in Figure 2. The asymptotic densities for $z \to \pm\infty$ in Figure 3 correspond (up to the factor $\pi/6$) to the sphere packing fractions at both ends of the tielines. With increasing $\rho_*^{\mathrm{r}}$, and hence increasing distance to the critical point, the interface becomes sharper, i.e. it crosses over from one to the other limiting (bulk) value over a shorter distance. For the highest needle reservoir density considered, $\rho_* = 22$, clear oscillations emerge on the liquid side of the interface, see the inset in Figure 3. The amplitude of the oscillations, however, is considerably smaller than that typically found at interfaces in the AO model (where the depletants are ideal spheres rather than needles) [115]. From the general theory of asymptotic decay of correlation functions [111, 112], we expect that all state points where the liquid density is inside the oscillatory region of the phase diagram (separated by the FW line) will display similar behaviour, and indeed we find oscillations on the liquid side of the interface also for $\rho_*^{\mathrm{r}} = 18, 20$. The liquid state at density $\rho_*^{\mathrm{r}} = 16$ is inside the monotonic region, and no oscillations emerge upon magnifying the corresponding density profile in Figure 3.

In the present geometry the needle density profile depends on two variables, namely the perpendicular distance $z$ from the interface and the angle $\vartheta$ of needle orientation and interface normal. The DFT yields $\rho_{\mathrm{N}}(z, \vartheta)$ fully dependent on both variables. In order to demonstrate this, we choose $\rho_*^{\mathrm{r}} = 22$ as an example and display in Figure 4 $\rho_*(z, \vartheta) \sin\vartheta$ as a function of $z/\sigma$. The factor $\sin\vartheta$ is the spherical volume element, hence the density distribution at a given angle $\vartheta$ is weighted according to the actual probability that $\vartheta$ is attained. This weight is maximal for $\vartheta = \pi/2$ (parallel to the interface) and vanishes for $\vartheta = 0$ (perpendicular to the interface). In order to graphically represent the density profile, we display a set of curves parameterised by $\vartheta$; each curve then depends on the single variable $z$, see Figure 4. As expected, the needles show a clear tendency to aggregate on the sphere-poor side of the interface. In order to assess the orientational distribution we also plot the bare $\rho_*(z, \vartheta)$ in Figure 4b. We observe that for fixed $z$ on the needle-rich side of the profiles the density increases with increasing $\vartheta$. This means that large angles are favoured, hence the needles tend to lie parallel to the surface, corresponding to biaxial order. On the needle rich side of the interface, however, the opposite trend is manifest. Upon increasing $\vartheta$ at fixed $z$ the density decreases. Hence small angles are more favourable; needles arrange perpendicular to the interface displaying uniaxial order.

In order to investigate the needle behaviour in more detail, we obtain two characteristic distributions from the full needle density profile $\rho_*(z, \vartheta)$. One is

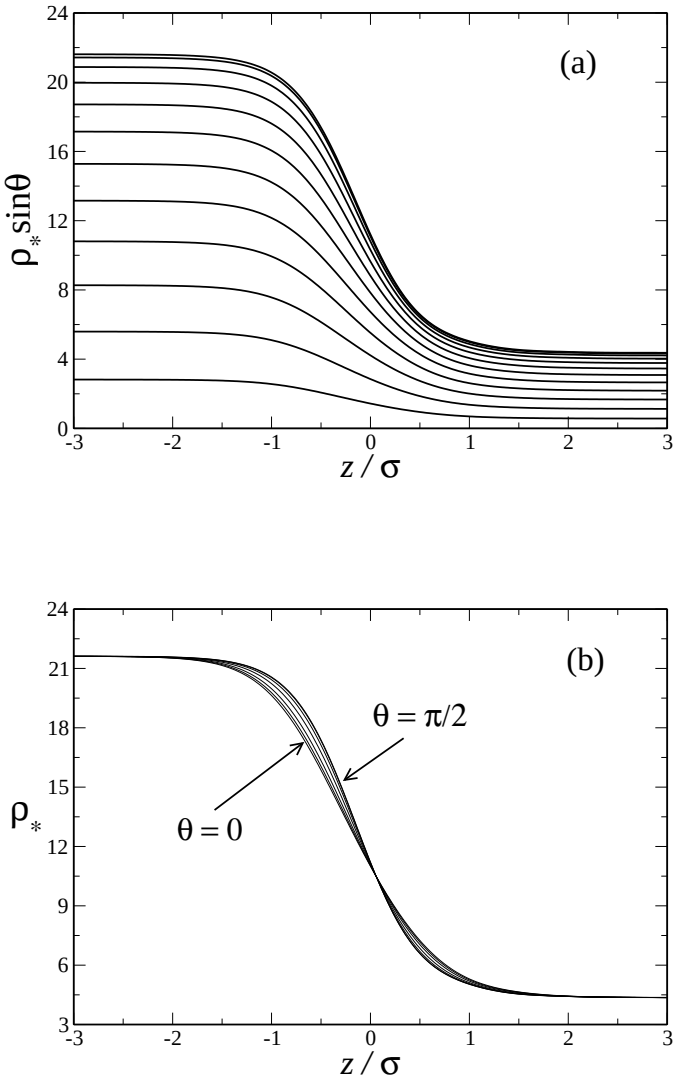


FIGURE 4. a) Scaled needle density multiplied by the spherical volume element, $\rho_*(z,\vartheta)\sin\vartheta$, as a function of $z/\sigma$ at the interface between sphere-poor ($z<0$) and sphere-rich ($z>0$) fluids for $\rho_*^{\mathrm{r}}=22$. Each curve is for fixed angle $\vartheta$ to the interface normal; from bottom to top $\vartheta$ increases from 0 (direction normal to the interface) to $\pi/2$ (direction parallel to the interface) in steps of $\pi/24$. b) The bare $\rho_*(z,\vartheta)$ without the volume element $\sin\vartheta$ is shown.

the orientation averaged needle density profile, defined as

$$\bar{\rho}_{\mathrm{N}}(z) = \frac{1}{4\pi} \int \rho_{\mathrm{N}}(\mathbf{r}, \mathbf{\Omega}) \, \mathrm{d}\Omega \tag{4.56}$$

$$= \frac{1}{2} \int_0^{\pi/2} \rho_{\mathrm{N}}(z, \vartheta) \sin\vartheta \, \mathrm{d}\vartheta, \tag{4.57}$$

which measures the density of needle midpoints regardless of their orientation. The other is an orientational order parameter profile defined as

$$\langle P_2(\cos\vartheta) \rangle = \frac{1}{\bar{\rho}_{\mathrm{N}}(z)} \frac{1}{4\pi} \int \rho_{\mathrm{N}}(\mathbf{r}, \mathbf{\Omega}) \, \mathrm{P}_2(\cos\vartheta) \, \mathrm{d}^2\Omega \tag{4.58}$$

$$= \frac{1}{2\bar{\rho}_{\mathrm{N}}(z)} \int \rho_{\mathrm{N}}(z, \vartheta) \, \mathrm{P}_2(\cos\vartheta) \sin\vartheta \, \mathrm{d}\vartheta, \tag{4.59}$$

where $\mathrm{P}_2(x) = (3x^2 - 1)/2$ is the second Legendre polynomial. Negative values of $\langle P_2(\cos\vartheta) \rangle$ indicate biaxial ordering, the extreme value being $-1/2$ for full parallel alignment to the interface (needles with $\vartheta = \pi/2$ lying in a plane). Positive values $\langle \mathrm{P}_2(\cos\vartheta) \rangle$ indicate uniaxial ordering, the extreme value (unity) is attained for perpendicular alignment to the interface ($\vartheta = 0$). Finally, $\langle \mathrm{P}_2(\cos\vartheta) \rangle = 0$ indicates isotropic states. Note that this order parameter has the same inflection symmetry as the needles.

In Figure 5 we show $\bar{\rho}_{\mathrm{N}}(z)$ for the four state points considered. A crossover from high values for negative $z$ to low values for positive $z$ is manifest; hence, as observed before, the needles are depleted in the space occupied by the colloids. The inset in Figure 5 shows a magnified view of the profile for $\rho_*^{\mathrm{r}} = 22$ on the sphere-rich side of the interface. Oscillations can be observed clearly. These arise from the packing effects of the *spheres*, and are "imprinted" on the needle distribution.

We next turn to the order parameter profile $\langle \mathrm{P}_2(\cos\vartheta) \rangle$, see Figure 6. On the needle-rich side ($z < 0$) of the interface we find that $\langle \mathrm{P}_2(\cos\vartheta) \rangle < 0$. This indicates needle ordering parallel to the interface, and can be understood in terms of packing effect, similar to those of rods near a hard wall. On the sphere-rich side ($z > 0$) we find that $\langle \mathrm{P}_2(\cos\vartheta) \rangle > 0$, hence the needles are oriented preferentially perpendicular to the interface. We attribute the ordering to needles that stick through the voids in the first sphere layer.

**6.3. Interface tension.** The interface tension $\gamma$ between demixed fluids is defined as the difference per unit area in grand potentials between the inhomogeneous situation and bulk. It is given by

$$\gamma A = \bar{\Omega} + PV \tag{4.60}$$

where $A$ is the interface area, $\bar{\Omega}$ is the grand potential in the inhomogeneous situation, and $P$ is the total pressure. Within our DFT approch it is obtained

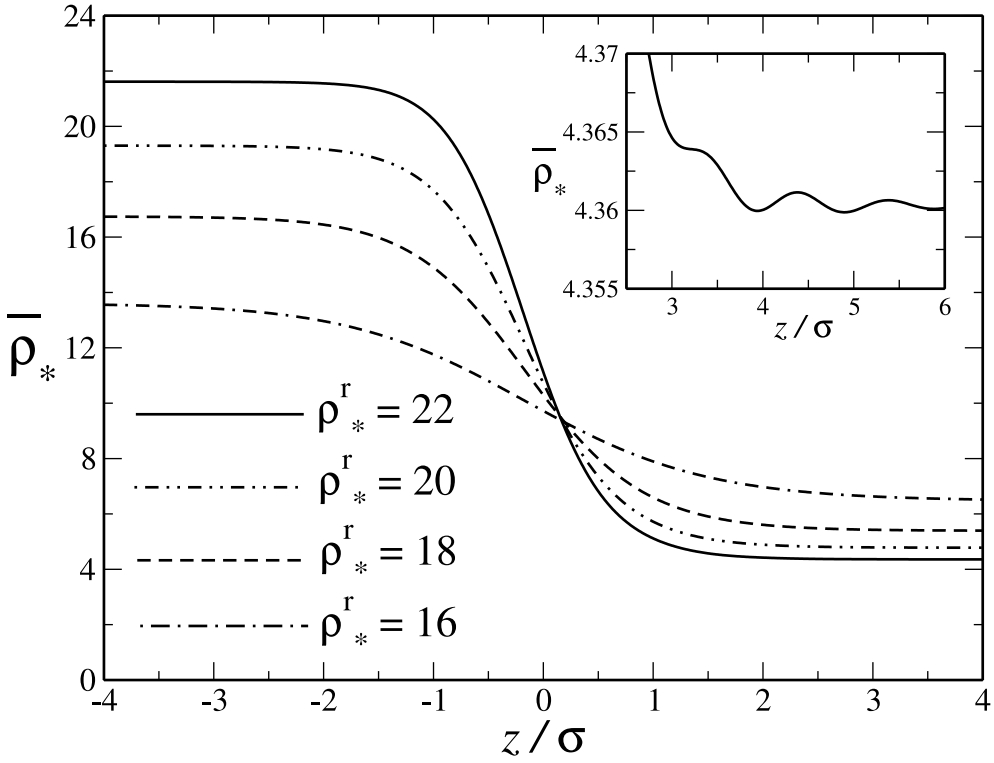


FIGURE 5. Orientation averaged needle density profiles $\bar{\rho}_*(z)$ as a function of the scaled distance $z/\sigma$ for $\rho^{\mathrm{r}}_* = 16, 18, 20, 22$ corresponding to Fig. 3. The inset shows $\bar{\rho}_*(z)$ as a function of $z/\sigma$ on the sphere-rich side ($z > 0$) of the interface for $\rho^{\mathrm{r}}_* = 22$. Damped oscillations are visible.

from

$$\gamma = \int [\omega(z) + P]\,\mathrm{d}z, \tag{4.61}$$

$$\omega(z) = -\mu_S \rho_{\mathrm{S}}(z) - \mu_N \bar{\rho}_{\mathrm{N}}(z) + \frac{\beta}{4\pi} \int \Phi(\{n^i_\nu(z,\vartheta)\})\,\mathrm{d}^2\Omega, \tag{4.62}$$

where $\Phi$ is the excess free energy density [given through Eqs. (4.14-4.16)] dependent on the weighted densities $n^i_\nu$ [Eqs. (4.18-4.20)], and $\mu_i$ is the chemical potential of species $i = S, N$. From dimensional analysis, it is clear that the typical scale of $\gamma$ should be the thermal energy, $kT$, divided by an area that is related to molecular length scales. However, as we deal with a binary mixture it is not obvious which power $b$ in $L^b\sigma^{2-b}$ gives the correct scaling with varying size ratio $L/\sigma$. We restrict ourselves to the cases $L/\sigma = 1, 1.5, 2$, where we find that $b = 1/3$ gives an almost complete data collapse, see Figure 7 for a plot of $\beta\gamma\sigma^{5/3}L^{1/3}$ as a function of the scaled distance to the critical value of the needle reservoir density, $(\rho^{\mathrm{r}}_* - \rho^{\mathrm{r}}_{*,\mathrm{crit}})/\rho^{\mathrm{r}}_{*,\mathrm{crit}}$. For states close to the critical

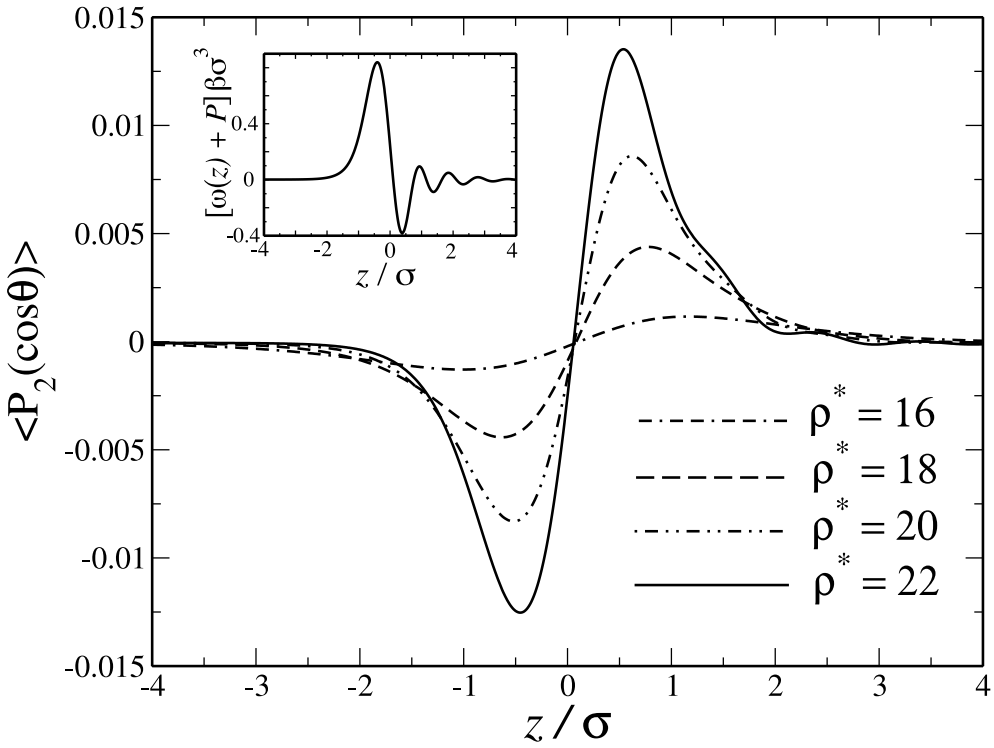


FIGURE 6. Orientational order parameter profiles $\langle \mathrm{P}_2(\cos\vartheta)\rangle$ as a function of the scaled distance $z/\sigma$ for $\rho_*^{\mathrm{r}} = 16, 18, 20, 22$ across the interface between sphere-poor ($z < 0$) and sphere-rich ($z > 0$) fluids. Negative values indicate parallel, positive values indicate normal alignment of needles relative to the interface. The inset shows the (scaled) integrand of the interface tension, $[\omega(z)+P]\beta\sigma^3$ as a function of $z/\sigma$ for $\rho_*^{\mathrm{r}} = 22$.

point, we find mean-field scaling of the surface tension, $\gamma \propto (\rho_*^{\mathrm{r}} - \rho_{*,\mathrm{crit}}^{\mathrm{r}})^{3/2}$. For $(\rho_*^{\mathrm{r}} - \rho_{*,\mathrm{crit}}^{\mathrm{r}})/\rho_{*,\mathrm{crit}}^{\mathrm{r}} > 0.4$ a linear relation is found that extends up to the triple point, for $L = \sigma$ this is from the perturbation theory of Ref. [86] roughly at the right end of the horizontal axis in Figure 7.

The magnitude of the interface tension is mainly governed by the difference in bulk densities of both phases. Hence a relevant variable is the difference $\eta_l - \eta_v$, where $\eta_l$ ($\eta_v$) is the sphere packing fraction in the coexisting liquid (vapour) phase. In the same spirit as above, we seek a combination of length scales to scale $\beta\gamma$, in order to obtain data collapse for different $L/\sigma$. It turns out that this is the case for $\beta\gamma\sigma^3 L^{-1}$, see the inset in Figure 7. Clearly, the different exponent to the case above arises from the relation between $\eta$ and $\rho_*$ given through the binodals for different $L/\sigma$. Although we only present results for $\sigma \leq L \leq 2\sigma$, we expect the scaling relations to hold beyond that range. However, for $L \gg \sigma$

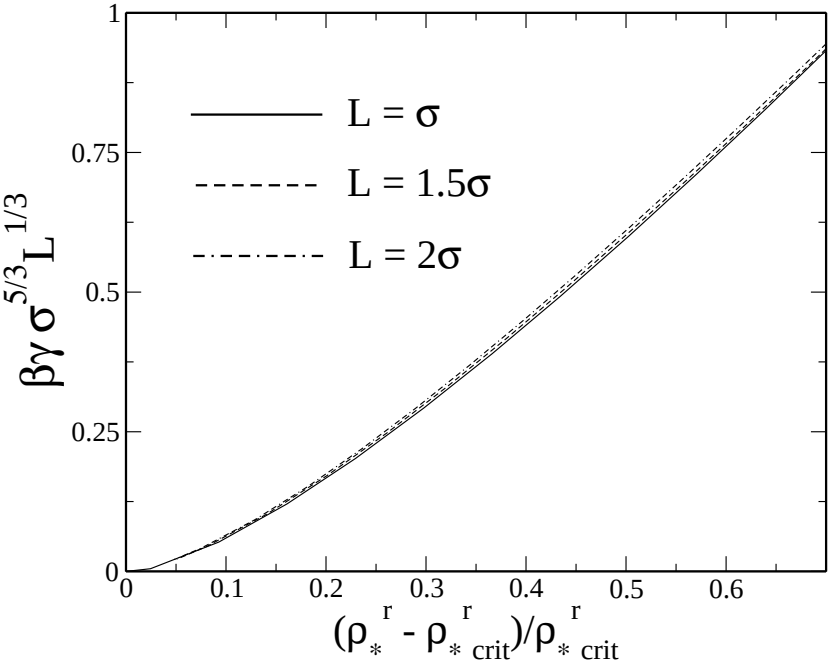


FIGURE 7. Scaled interface tension $\beta\gamma\sigma^{5/3}L^{1/3}$ as a function of the scaled distance from the critical point $(\rho_*^{\mathrm{r}} - \rho_{*,\mathrm{crit}}^{\mathrm{r}})/\rho_{*,\mathrm{crit}}^{\mathrm{r}}$ for size ratios $L/\sigma = 1, 1.5, 2$. All curves practically collapse onto each other. The inset shows the scaled interface tension $\beta\gamma\sigma^3 L^{-1}$ as a function of the difference between liquid and vapour sphere packing fractions, $\eta_l - \eta_v$, for the same size ratios $L/\sigma = 1, 1.5, 2$.

there might well be a crossover to a different scaling regime, and preliminary results show deviations already for $L = 5\,\sigma$.

As a final issue, we seek to elucidate further the origin of the surface tension. A recent study by Archer and Evans addressed this issue in a binary mixture of Gaussian core particles [119] (see Figuress 11 and 12 therein). They consider two different regimes for their model: (a) where demixing is driven by non-additivity and (b) where it is driven by energetics, and construct two new variables, namely the total density and a local concentration. In order to calculate the surface tension one must perform the integral Eq. (22) in Ref. [119] [corresponding to our Eq. (4.61)]. If the integrand is plotted they find that in regime (a) it closely resembles the local concentration and in regime (b) the total density. Their conclusion is that in one regime, $\gamma$ is dominated by concentration fluctuations and in the other, by fluctuations in the total density.

Applying this analysis to our model, we find that neither local concentration nor total density resemble the integrand of the surface tension in Eq. (4.61). However, the integrand closely resembles the (negative) of the orientational order parameter, see the inset in Figure 6 for a plot of $[w(z) + P]\beta\sigma^3$ as a function of $z/\sigma$ for the largest reservoir density considered, $\rho_*^{\mathrm{r}} = 22$. As interpretation of the similarity, negative values of $\langle \mathrm{P}_2(\cos\vartheta)\rangle$ indicate a loss of rotational entropy, and hence a a positive contribution to $\gamma$. Positive values of $\langle \mathrm{P}_2(\cos\vartheta)\rangle$ indicate a relaxation of the needles sticking through the first sphere layer and hence lowering the tension. From this analysis, it it tempting to argue that in the present model the surface tension is determined by *orientation* fluctuations.

## 7. Conclusions

In conclusion, we have considered the free (planar) interface between demixed fluid phases in a model mixture of spherical and needle-shaped colloidal particles. We have focused on the case of vanishingly thin needles, which constitutes a minimal model for orientational order at fluid interfaces. Both sphere and needle density profiles show either monotonic or damped oscillatory behaviour on the sphere-rich (and needle-poor) side of the interface, depending on which side of the Fisher-Widom line in the bulk phase diagram the sphere liquid state resides. The amplitude of the oscillations, however, is considerably smaller than in the related AO model of spherical (polymer) depletants, and will be further reduced by capillary fluctuations that are not taken into account in the present treatment. It is tempting to interpret the smaller amplitude in the current model by a washing out of oscillations due to the depletants' rotator degrees of freedom, which are absent in the AO case. On the needle-rich (and sphere-poor) side of the interface both density profiles decay monotonically towards the respective bulk densities. Needles possess biaxial order on the needle-rich side, i.e. they lie preferentially parallel to the interface plane. This can be understood in terms of simple packing of needles against the dense hard sphere fluid. On the sphere-rich side uniaxial order of needles occurs, i.e. needles tend to be oriented normal to the interface. This is somewhat surprising, and we interpret this effect as being caused by the void structure of the hard sphere fluid, into which the needles stick to maximise their entropy.

We have furthermore given explicit expressions for the present density functional for the important cases of planar and spherical symmetries, facilitating future studies.

Testing our predictions for the fluid-fluid interface constitutes a demanding task for computer simulations due to the large numbers of needles involved at state points of interest, and due to the difficulty of stabilising the free fluid-fluid interface in a finite simulation box. An alternative circumventing the first problem could be to study an effective one-component system of spheres that

interacts by means of the needle-depletion potential [90], although such an approach would prevent study of the orientational distribution of the needles.

Recently, P.G. Bolhuis *et al.* [123] have performed Monte-Carlo computer simulations of the fluid-fluid interface. They have confirmed the orientational ordering of the needles close to the interface.

Moreover, R. Roth *et al.* [124] have used the density functional presented in this chapter to investigate entropic wetting of a hard wall. They find that for small rods, the sphere liquid wets the wall completely as long as the rod density lies below the wetting point.

CHAPTER 5

# Mixtures of Spheres and Rods in the Onsager Limit

## 1. Introduction

Mixtures of colloidal spheres and mesoscopic rods, like colloidal rods or stiff polymer chains, suspended in a molecular solvent, are well-characterised model systems governed by steric (excluded volume) forces [13, 14, 80, 81, 85, 120, 121]. Interesting questions concern the bulk phase behaviour and effective sphere-sphere and sphere-wall interactions mediated by the presence of the rods [13, 14, 121]. Based on Rosenfeld's fundamental-measure theory for mixtures of non-convex bodies [101, 122], a density-functional theory [95] for a minimal model of hard sphere colloids and infinitely thin needles [86] was proposed [105] and used to investigate the structure of the interface between sphere-rich and sphere-poor phases [116, 123], and the wetting behaviour of a hard wall [124]. This binary DFT proved to predict phase behaviour accurately compared to the simulation results of [86], and to give high-quality results for (fluid) density profiles in inhomogeneous situations, when compared both to results from an effective one-component treatment [124] using the depletion potential between spheres [90, 125], and to computer simulation results of the free fluid-fluid interface of the binary mixture [123]. By combining Yu and Wu's functional for mixtures of polymeric fluids [126] and the theory of Ref. [105], Bryk arrived at a DFT for binary mixtures of hard rods and polymer chains [127].

In all these cases, the rods are assumed to have vanishing thickness. Due to the geometry, the statistical weight of configurations with overlapping rods vanishes, and hence the rods behave as though being ideal. (The rod-sphere interaction is unaffected by this argument and is governed by excluded volume.) Rosenfeld's theory when applied to a mixture of hard spheres of finite (large) packing fraction and a second component of (thick) spherocylinders at vanishing density was shown to predict the entropic force and torque on the rod near a hard wall very accurately [108], and more general cases have also been considered [128].

In order to capture effects of finite rod thickness *and* finite rod density, an extension to the theory for vanishingly thin rods [105] was made in Ref. [116], incorporating the Onsager limit of the rods [129], hence recovering exactly the rod-rod Mayer bond in the limit of large aspect ratio. The Onsager model continues to be a valuable system to study the properties of anisometric particles, see e.g. Ref. [109, 130, 131] for recent work. Cinacchi and Schmid proposed a

DFT for general anisotropic particles interpolating between the Rosenfeld and the Onsager functional [132]. The theory of Ref. [116] is, however, restricted to the limit of $LD/\sigma^2 \ll 1$ where $L$ and $D$ are the rod length and thickness, respectively, and $\sigma$ is the sphere diameter.

## 2. Model

In the present chapter, we extend the framework, restricting ourselves still to the Onsager limit [129] of $L/D \gg 1$.

In this case, a residual excluded volume persists for thin rods, leading to non-trivial interaction already in the pure needle system. Again, the pair potential is that of hard bodies and is given, for the difference vector $\mathbf{r}$ between the centres of two needles with orientations $\mathbf{\Omega}$ and $\mathbf{\Omega}'$, as $V_{\mathrm{NN}}(\mathbf{r}, \mathbf{\Omega}, \mathbf{\Omega}') = \infty$ if both rods overlap, and zero otherwise.

This is accomplished by introducing several new geometric weight functions. We demonstrate how these weight functions recover the leading order contribution (in $D$) to the rod–sphere and rod–rod Mayer bonds. Our model is a binary mixture of hard spheres (species $S$) of diameter $\sigma = 2R$ and hard needle-like spherocylinders (species $N$) with length $L$ (of the cylindrical part) and diameter $D$. This is considered in the (Onsager) limit of large rod aspect ratio of length-to-thickness, $L/D \gg 1$. The one-body density distributions of spheres and needles are denoted by $\rho_{\mathrm{S}}(\mathbf{r})$ and $\rho_{\mathrm{N}}(\mathbf{r}, \mathbf{\Omega})$, respectively, where $\mathbf{r}$ is the position coordinate (pointing to the centre of the respective particle shape) and $\mathbf{\Omega}$ is a unit vector describing the needle orientation.

Note that the Onsager limit is obtained by letting $L/D \to \infty$ while keeping the combination $\rho_{\mathrm{N}} D L^2$ constant. Here we furthermore restrict ourselves to size ratios that fulfil $LD \ll R^2$, i.e. the sphere surface is assumed to be large compared to the needle surface. This additional restriction is similar in spirit to the Onsager limit for pure needles and constitutes the simplest scaling regime of the three lengths $R, L, D$.

## 3. Density functional theory

We start by defining the density functional. In order to not duplicate material, explicit expressions are given only for the new quantities. We refer the reader directly to Chapter 4 for a full account of the known terms. We do, however, discuss the relation to the sphere-rod Mayer bond in detail below. The Helmholtz excess (over ideal gas) free energy functional is expressed as

$$F_{\mathrm{exc}}[\rho_{\mathrm{S}}, \rho_{\mathrm{N}}] = kT \frac{1}{4\pi} \iint \Phi(\{n_i^\alpha\}) \, \mathrm{d}^3 r \, \mathrm{d}^2\Omega, \tag{5.1}$$

where $k$ is the Boltzmann constant and $T$ is temperature, $n_i^\alpha$ are weighted densities that are obtained through convolutions of the bare density profiles with geometric weight functions $w_i^\alpha$; $\alpha$ refers to the particle species and $i$ refers to

the type of weighted density. The weight functions $w_i^\alpha$ are obtained by imposing the correct (2nd order) low-density behaviour of (5.1); this is achieved by the so-called deconvolution of the Mayer bond, which we will turn to below. The functional form of $\Phi$ is obtained from consideration of the dimensional crossover [99, 100] and scaled-particle ideas [96].

The weight functions necessary to recover the sphere–needle and needle–needle Mayer bonds are found to be

$$w_1^{\mathrm{SN}}(\mathbf{r},\mathbf{\Omega}) = (2\pi)^{-1}\delta(\mathbf{r}\cdot\mathbf{\Omega})\delta(R-r), \tag{5.2}$$

$$w_{2\pm}^{\mathrm{SN}\Delta}(\mathbf{r},\mathbf{\Omega}) = \delta(R-r)\Theta(\pm\mathbf{\Omega}\cdot\mathbf{r}), \tag{5.3}$$

$$w_{1\pm}^{N\Delta}(\mathbf{r},\mathbf{\Omega}) = (D/2)\delta\left(\mathbf{r}\pm L\mathbf{\Omega}/2\right), \tag{5.4}$$

$$w_2^{\mathrm{N}}(\mathbf{r},\mathbf{\Omega}) = \pi D \int_{-L/2}^{L/2} \delta(\mathbf{r}+\mathbf{\Omega}l)\,\mathrm{d}l, \tag{5.5}$$

$$w_2^{\mathrm{NN}}(\mathbf{r},\mathbf{\Omega};\mathbf{\Omega}') = 16D\sqrt{1-(\mathbf{\Omega}\cdot\mathbf{\Omega}')^2}\; w_1^{\mathrm{N}}(\mathbf{r},\mathbf{\Omega}). \tag{5.6}$$

where $R=\sigma/2$ is the sphere radius, $\delta(\cdot)$ is the Dirac distribution, $\Theta(\cdot)$ is the Heaviside step function, and $r=|\mathbf{r}|$. We use *mixed* weight functions that depend on properties of both species (see Fig. 1 for illustrations). $w_1^{\mathrm{SN}}$ describes the "equator" of the sphere, where the polar axis is pointing into the direction given by the (needle) orientation $\mathbf{\Omega}$. $w_{2\pm}^{\mathrm{SN}\Delta}$ describes the "northern" (subscript $+$) and "southern" (subscript $-$) hemisphere. Hence $w_{2+}^{\mathrm{SN}\Delta}+w_{2-}^{\mathrm{SN}\Delta}=w_2^{\mathrm{S}}$, where $w_2^{\mathrm{S}}$ is the usual sphere surface weight function [96]. The rod endcaps are described by $w_{1\pm}^{\mathrm{N}\Delta}$, where $w_{1+}^{\mathrm{N}\Delta}+w_{1-}^{\mathrm{N}\Delta}=Dw_0^N$ (as defined in Eq. (4.2)). The weight function $w_2^{\mathrm{N}}$ makes the dimensional analysis consistent [101, 122], and is proportional to a known weight, $w_2^{\mathrm{N}}=4\pi D w_1^{\mathrm{N}}$, where $w_1^{\mathrm{N}}$ is given in Eq. (4.1) and obtained directly through [101, 122]. The function $w_2^{\mathrm{NN}}$ describes the residual rod surface in the limit of large aspect ratio.

The corresponding fundamental measures, $\xi_\alpha^i=\iint w_\alpha^i/(4\pi)\,\mathrm{d}^3r\,\mathrm{d}^2\Omega$, are

$$\xi_1^{\mathrm{SN}}=R,\quad \xi_{2\pm}^{\mathrm{SN}\Delta}=2\pi R^2,\quad \xi_{1\pm}^{N\Delta}=D/2,\quad \xi_2^{\mathrm{N}}=\pi LD, \tag{5.7}$$

equal to the integral mean curvature of the sphere, surface of a hemisphere of radius $R$, radius of a hemispherical endcap of the rod, and residual (for small $D/L$) rod surface, respectively.

Weighted densities are built using spatial convolution, but retaining the angular dependence. For the needle–needle weight function, an angular convolution is also required. This turns out to be necessary for the present case of interacting

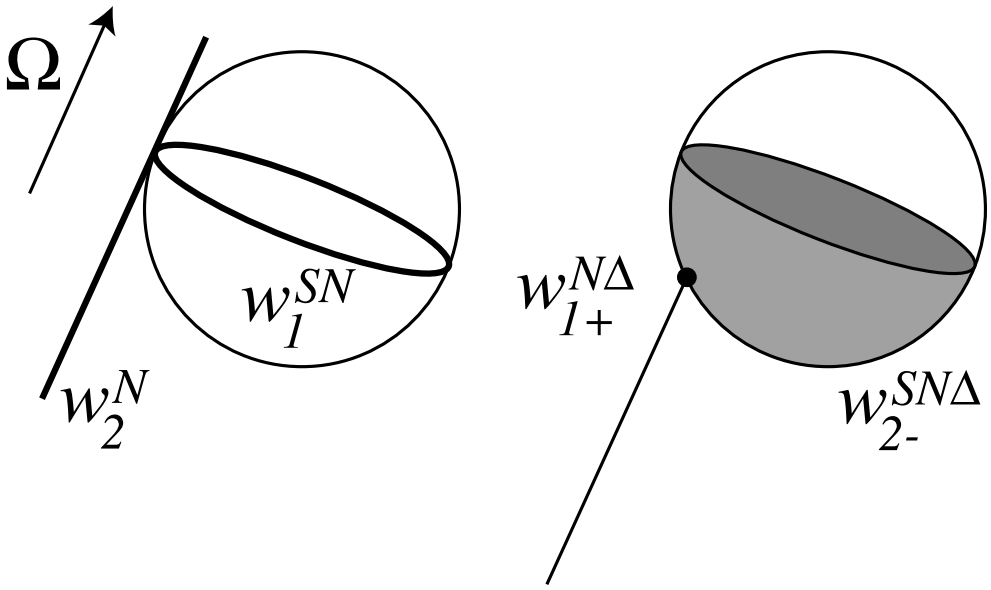


FIGURE 1. Illustration of the geometry of the weight functions: $w_2^{\mathrm{N}}$ describes the residual rod surface (thick line), $w_1^{\mathrm{SN}}$ is non-vanishing on the equator of the sphere (bold circle), $w_1^{\mathrm{N}\Delta+}$ corresponds to one rod endcap (dot), and $w_2^{\mathrm{SN}\Delta-}$ describes a hemisphere (gray).

anisotropic particles.

$$n_1^{\mathrm{SN}}(\mathbf{x},\mathbf{\Omega}) = \int \rho_{\mathrm{S}}(\mathbf{r}) w_1^{\mathrm{SN}}(\mathbf{x}-\mathbf{r},\mathbf{\Omega})\,\mathrm{d}^3 r, \tag{5.8}$$

$$n_{2\pm}^{\mathrm{SN}\Delta}(\mathbf{x},\mathbf{\Omega}) = \int \rho_{\mathrm{S}}(\mathbf{r}) w_{2\pm}^{\mathrm{SN}\Delta}(\mathbf{x}-\mathbf{r},\mathbf{\Omega})\,\mathrm{d}^3 r, \tag{5.9}$$

$$n_{1\pm}^{N\Delta}(\mathbf{x},\mathbf{\Omega}) = \int \rho_{\mathrm{N}}(\mathbf{r},\mathbf{\Omega}) w_{1\pm}^{N\Delta}(\mathbf{x}-\mathbf{r},\mathbf{\Omega})\,\mathrm{d}^3 r, \tag{5.10}$$

$$n_2^{\mathrm{N}}(\mathbf{x},\mathbf{\Omega}) = \int r\rho_{\mathrm{N}}(\mathbf{r},\mathbf{\Omega}) w_2^{\mathrm{N}}(\mathbf{x}-\mathbf{r},\mathbf{\Omega})\,\mathrm{d}^3 r, \tag{5.11}$$

$$n_2^{\mathrm{NN}}(\mathbf{r},\mathbf{\Omega}') = \frac{1}{4\pi}\iint \rho_{\mathrm{N}}(\mathbf{r},\mathbf{\Omega}) w_2^{\mathrm{NN}}(\mathbf{x}-\mathbf{r},\mathbf{\Omega};\mathbf{\Omega}')\,\mathrm{d}^3 r\,\mathrm{d}^2\Omega, \tag{5.12}$$

Note that orientation-dependent *sphere* densities are built via (5.8) and (5.9).

Following Rosenfeld's dimensional analysis [96, 101, 122], and in accordance with the scaled-particle theory for mixtures of non-spherical particles [117], the (reduced) free energy density is found to be $\Phi = \Phi_S + \Phi_{\mathrm{SN}} + \Phi_{\mathrm{SNN}} + \Delta\Phi$, where $\Phi_{\mathrm{S}}$ is the hard sphere term [96], $\Phi_{\mathrm{SN}}$ is the contribution in the case of infinitely thin needles [105]; these terms are given explicitly in Eqs. (4.15) and (4.16),

respectively. The new contributions are

$$\Delta\Phi = \frac{n_1^{\mathrm{SN}} n_2^{\mathrm{N}} + n_{1+}^{\mathrm{N}\Delta} n_{2-}^{\mathrm{SN}\Delta+} + n_{1-}^{\mathrm{N}\Delta} n_{2+}^{\mathrm{SN}\Delta}}{1 - n_3^{\mathrm{S}}}, \tag{5.13}$$

$$\Phi_{\mathrm{SNN}} = \frac{n_1^{\mathrm{N}} n_2^{\mathrm{NN}}}{1 - n_3^{\mathrm{S}}}, \tag{5.14}$$

where $n_3^{\mathrm{S}}(\mathbf{r}) = \Theta(R - |\mathbf{r}|) * \rho_{\mathrm{S}}(\mathbf{r})$ is the usual local packing fraction for spheres. This completes the prescription of the functional.

As an aside, we can immediately reformulate the Onsager excess free energy functional for a pure system of rods, being precisely a second order virial expansion, by setting $\Phi = \Phi_{\mathrm{SNN}}$ and $n_3^{\mathrm{S}} = 0$ in Eq. (5.1).

The exact 2nd virial coefficient between sphere and rod is

$$B_2^{\mathrm{SN}} = \pi R^2 \left( L + \frac{4R}{3} \right) + \pi DR(L + 2R) + \pi D^2 \left( \frac{L}{4} + R \right) + \frac{\pi D^3}{6}, \tag{5.15}$$

where the theory of Chapter 4 obtains the first term (independent of $D$), and the present chapter recovers also the next term, linear in $D$.

Expanding (5.13) for small density leads to second (leading) order

$$\Delta\phi = n_1^{\mathrm{SN}} n_2^{\mathrm{N}} + n_{1+}^{\mathrm{N}\Delta} n_{2-}^{\mathrm{SN}\Delta} + n_{1-}^{\mathrm{N}\Delta} n_{2+}^{\mathrm{SN}\Delta} \tag{5.16}$$

$$= \rho_{\mathrm{S}} \rho_{\mathrm{N}} (\xi_1^{\mathrm{SN}} \xi_2^{\mathrm{N}} + \xi_{1+}^{\mathrm{N}\Delta} \xi_{2-}^{\mathrm{SN}\Delta} + \xi_{1-}^{\mathrm{N}\Delta} \xi_{2+}^{\mathrm{SN}\Delta}) \tag{5.17}$$

$$= \rho_{\mathrm{S}} \rho_{\mathrm{N}} \pi (LDR + 2DR^2). \tag{5.18}$$

Hence the additional contribution to the 2nd virial coefficient is

$$B_2^{\mathrm{SN}\Delta} = \Delta\phi / (\rho_{\mathrm{S}} \rho_{\mathrm{N}}) = \pi (LDR + 2DR^2), \tag{5.19}$$

indeed equal to the second term of the exact result, given in (5.15).

## 4. Deconvolution of the Mayer bonds

**4.1. The rod–rod Mayer bond.** The Mayer bond $f(\mathbf{r}, \mathbf{\Omega}, \mathbf{\Omega}')$ of two hard bodies is defined as being $-1$ if both particles overlap and zero otherwise. In order to deal with rod–rod interactions, we first express the Mayer bond between rods in the Onsager limit through

$$f_{\mathrm{NN}}(\mathbf{r}, \mathbf{\Omega}, \mathbf{\Omega}')/2 = -w_2^{\mathrm{NN}}(\mathbf{r}, \mathbf{\Omega}; \mathbf{\Omega}') * w_1^{\mathrm{N}}(\mathbf{r}, \mathbf{\Omega}'), \tag{5.20}$$

where $\mathbf{r}$ is the difference vector between the needle centres and $\mathbf{\Omega}, \mathbf{\Omega}'$ are their respective orientations.

Choosing a specific coordinate system, we demonstrate the validity of (5.20). Since only the relative orientation of both rods is relevant, we take $\mathbf{\Omega}' = (0, 0, 1)$ and $\mathbf{\Omega} = (0, \sin\vartheta, \cos\vartheta)$; the difference vector between both particle positions is

$(x, y, z)$. We then perform the spatial convolution of the weight functions given in Eqs.(4.1,5.6) as

$$
\begin{aligned}
&-2w_2^{\mathrm{NN}}(\mathbf{r}, \mathbf{\Omega}; \mathbf{\Omega}') * w_1^{\mathrm{N}}(\mathbf{r}, \mathbf{\Omega}') \\
&\quad = -2D \sin\vartheta \int_{-\infty}^{\infty}\int_{-\infty}^{\infty}\int_{-\infty}^{\infty}\int_{-L/2}^{L/2} \delta(x')\delta(y' + l\sin\vartheta)\delta(z' + l\cos\vartheta)\,\mathrm{d}l \\
&\qquad \times \int_{-L/2}^{L/2} \delta(x - x')\delta(y - y')\delta(z - z' + l')\,\mathrm{d}l'\,\mathrm{d}x'\,\mathrm{d}y'\,\mathrm{d}z' \qquad (5.21)\\
&\quad = -2D \tan\vartheta \int_{-\infty}^{\infty}\int_{-\infty}^{\infty}\int_{-\infty}^{\infty} \delta(x')\Theta\Big(\frac{L}{2} - \Big|\frac{y'}{\sin\vartheta}\Big|\Big)\delta\Big(z' - \frac{y'}{\tan\vartheta}\Big) \\
&\qquad \times \int_{-L/2}^{L/2} \delta(x - x')\delta(y - y')\delta(z - z' + l')\,\mathrm{d}l'\,\mathrm{d}x'\,\mathrm{d}y'\,\mathrm{d}z' \qquad (5.22)\\
&\quad = -2D\,\delta(x)\Theta\Big(\frac{L}{2} - \Big|\frac{y}{\tan\vartheta} + z\Big|\Big)\Theta\Big(\frac{L}{2} - \Big|\frac{y}{\sin\vartheta}\Big|\Big) \qquad (5.23)\\
&\quad = f_{\mathrm{NN}}(\mathbf{r}, \mathbf{\Omega}; \mathbf{\Omega}'). \qquad (5.24)
\end{aligned}
$$

From Eq. (5.21) to (5.22), we solve the integral over $l$ as an explanatory case; the other integrals can be done analogously. In order to recognise that Eq. (5.23) is indeed the rod–rod Mayer bond, we compare with the expressions given in Ref. [133], and observe that the step-functions in Eq. (5.23) correspond to Eqs. (A1,A2) in the appendix of Ref. [133]. Since

$$\lim_{D\to 0} \frac{1}{2D}\Theta(D - |x|) = \delta(x),$$

the term $2D\,\delta(x)$ corresponds to Eq. (A3) in Ref. [133] in the limit of small values of $D$, hence Eq.(5.24) constitutes a valid equality.

**4.2. The sphere–rod Mayer bond.** In the following we demonstrate the deconvolution of the sphere–rod Mayer bond. We split $f_{\mathrm{SN}} = f_{\mathrm{SN}}^{(D=0)} + \Delta f_{\mathrm{SN}}$, where $f_{\mathrm{SN}}^{(D=0)}$ is the Mayer bond for vanishingly thin needles, which can be deconvolved into one-body weight functions, see Chapter 4, Section 3.1 (where this contribution is denoted $f_{\mathrm{SN}}$). We express the correction, valid for small $D/L$, as

$$
\begin{aligned}
-\Delta f_{\mathrm{SN}}(\mathbf{r}, \mathbf{\Omega}) = \frac{D}{2}\Big(&\Theta(|\mathbf{r}\cdot\mathbf{\Omega}| - L/2)\delta(|\mathbf{r} - (\mathbf{r}\cdot\mathbf{\Omega})\mathbf{\Omega}| - R) \\
&+ \delta(|\mathbf{r} + L\mathbf{\Omega}/2| - R)\Theta(-\mathbf{r}\cdot\mathbf{\Omega} - L/2) \\
&+ \delta(|\mathbf{r} - L\mathbf{\Omega}/2| - R)\Theta(\mathbf{r}\cdot\mathbf{\Omega} - L/2)\Big),
\end{aligned} \qquad (5.25)
$$

where $\mathbf{r}$ is the difference vector between the particle centres and $\mathbf{\Omega}$ is the rod orientation. Note that

$$\lim_{D\to 0} \frac{D}{2}\delta(x) = \Theta\left(\frac{D}{4} - \left|x - \frac{D}{4}\right|\right).$$

Using the weight functions, (5.2)–(5.5), this can be expressed as

$$-\Delta f_{\mathrm{SN}} \;=\; w_1^{\mathrm{SN}} * w_2^{\mathrm{N}} + w_{1+}^{\mathrm{N}\Delta} * w_{2-}^{\mathrm{SN}\Delta} + w_{1-}^{N\Delta} * w_{2+}^{\mathrm{SN}\Delta}, \tag{5.26}$$

where $*$ denotes the spatial convolution.

We next choose a specific coordinate system, and demonstrate the validity of Eq. (5.26). We first consider the first term on the right hand side of Eq. (5.26) and take the needle orientation $\mathbf{\Omega}$ to be parallel to the $z$ axis and both needle and sphere to lie within the $y$-$z$ plane, i.e. $\mathbf{\Omega} = (0, \bar{\varphi}), \mathbf{r} = (r, \vartheta, 0)$. Then,

$$\begin{aligned} & w_1^{\mathrm{SN}}(\mathbf{r}, \mathbf{\Omega}) * w_2^{\mathrm{N}}(\mathbf{r}, \mathbf{\Omega}) \\ & \quad = \frac{D}{2} \int_0^{\pi}\int_0^{2\pi} \delta(R\cos\vartheta') \\ & \qquad \times \int_{-L/2}^{L/2} \delta\Big(\begin{smallmatrix} -R\sin\vartheta'\sin\varphi' \\ r\sin\vartheta - R\sin\vartheta'\cos\varphi' \\ r\cos\vartheta - R\cos\vartheta' + l \end{smallmatrix}\Big) \mathrm{d}l\, R^2 \sin\vartheta'\, \mathrm{d}\varphi'\, \mathrm{d}\vartheta' \end{aligned} \tag{5.27}$$

$$= \frac{D}{2} \int_0^{2\pi}\int_{-L/2}^{L/2} \delta\Big(\begin{smallmatrix} -R\sin\varphi' \\ r\sin\vartheta - R\cos\varphi' \\ r\cos\vartheta + l \end{smallmatrix}\Big) \mathrm{d}l R\, \mathrm{d}\varphi' \tag{5.28}$$

$$= \frac{D}{2}\Theta\left(\frac{L}{2} - |r\cos\vartheta|\right) \int_0^{2\pi} \delta(R\sin\varphi')\delta(r\sin\vartheta - R\cos\varphi') R\, d\varphi' \tag{5.29}$$

$$= \frac{D}{2}\Theta\left(\frac{L}{2} - |r\cos\vartheta|\right) \delta(r\sin\vartheta - R), \tag{5.30}$$

which recovers the first line of Eq. (5.25).

We next consider the term $w_{1+}^{\mathrm{N}\Delta} * w_{2-}^{\mathrm{SN}\Delta}$ in Eq. (5.26); the calculation of $w_{1-}^{\mathrm{N}\Delta} * w_{2+}^{\mathrm{SN}\Delta}$ can be performed analogously and is skipped here. We write the convolution in its most general form, i.e. using absolute coordinates,

$$\begin{aligned} & \int w_{1+}^{\mathrm{N}\Delta}(\mathbf{r} - \mathbf{r}', \mathbf{\Omega}) w_{2-}^{\mathrm{SN}\Delta}(\mathbf{r}'' - \mathbf{r}') \mathrm{d}^3 r' \\ & \qquad = \int \frac{D}{2}\delta(\mathbf{r} - \mathbf{r}' + \mathbf{\Omega}\frac{L}{2})\delta(R - |\mathbf{r}'' - \mathbf{r}'|)\Theta(-\mathbf{\Omega}\cdot(\mathbf{r}'' - \mathbf{r}'))\, \mathrm{d}^3 r'. \end{aligned} \tag{5.31}$$

Then we place everything in the $x$-$y$-plane, $\vartheta = \bar{\vartheta} = \vartheta'' = \pi/2$; the sphere shall sit on the negative $x$-axis: $\varphi'' = -\pi/2$. Using the remaining translational symmetry, we put the tip of the needle in the origin: $r = L/2, \varphi = \pi + \bar{\varphi}$. To summarise, we

have: $\mathbf{r} = (L/2, \pi/2, \pi + \bar{\varphi}), \mathbf{r}' = (r', \vartheta', \varphi'), \mathbf{r}'' = (r'', \pi/2, -\pi/2), \mathbf{\Omega} = (\pi/2, \bar{\varphi})$. Using these coordinates we can transform Eq. (5.31) and obtain:

$$\begin{aligned} & w_{1+}^{\mathrm{N}\Delta}(\mathbf{r}, \mathbf{\Omega}) * w_{2-}^{\mathrm{SN}\Delta}(\mathbf{r}, \mathbf{\Omega}) \\ &= \frac{D}{2} \int_0^\infty \int_0^{2\pi} \int_0^\pi \delta(r' \sin\vartheta' \sin\varphi') \delta(r' \sin\vartheta' \cos\varphi') \delta(r' \cos\vartheta') \\ &\quad \times \delta(R - \sqrt{r''^2 + r'^2 + 2r'r'' \sin\vartheta' \sin\varphi'}) \\ &\quad \times \Theta(r'' \sin\bar{\varphi} + r' \sin\vartheta' \sin\varphi' \sin\bar{\varphi} + r' \sin\vartheta' \cos\varphi' \cos\bar{\varphi}) \\ &\quad \times r'^2 \sin\vartheta' \mathrm{d}\vartheta' \, \mathrm{d}\varphi' \, \mathrm{d}r' \end{aligned} \tag{5.32}$$

$$\begin{aligned} &= \frac{D}{2} \int_0^\infty \int_0^{2\pi} \delta(r' \sin\varphi') \delta(r' \cos\varphi') \delta(R - \sqrt{r''^2 + r'^2 + 2r'r'' \sin\varphi'}) \\ &\quad \times \Theta(r'' \sin\bar{\varphi} + r' \sin\varphi' \sin\bar{\varphi} + r' \cos\varphi' \cos\bar{\varphi}) \, r' \, \mathrm{d}\varphi' \, \mathrm{d}r' \end{aligned} \tag{5.33}$$

$$= \frac{D}{2} \sum_{\pm} \int_0^\infty \delta(r') \delta(R - \sqrt{r''^2 + r'^2}) \Theta(r'' \sin\bar{\varphi} \pm r' \cos\bar{\varphi}) \, \mathrm{d}r' \tag{5.34}$$

$$= \frac{D}{2} \delta(R - r'') \Theta(r'' \sin\bar{\varphi}) \tag{5.35}$$

which recovers the second line of Eq. (5.25).

We turn to a brief investigation of the prediction of the DFT for the bulk free energy. There the contribution of (5.13) to the free energy per volume is obtained by setting $\rho_i = \text{const}$, and hence $n_i^\alpha = \xi_i^\alpha \rho_i$. With the sphere packing fraction $\eta = \pi \rho_{\mathrm{S}} \sigma^3/6$, the resulting excess free energy is

$$\begin{aligned} \frac{\beta F_{\mathrm{exc}}}{V} = \phi_{\mathrm{hs}}(\eta) - \rho_{\mathrm{N}} \ln(1-\eta) + \frac{\pi L^2 D}{4} \frac{\rho_{\mathrm{N}}^2}{1-\eta} \\ + \frac{3}{2} \left( \frac{L}{2R} + \frac{LD}{2R^2} + \frac{D}{R} \right) \frac{\rho_{\mathrm{N}} \eta}{1-\eta}, \end{aligned} \tag{5.36}$$

where $\phi_{\mathrm{hs}}$ is equal to the Percus-Yevick compressibility (scaled-particle) result for pure hard spheres, $V$ is the system volume, and the second and third term inside the parentheses is the contribution due to (5.13).

## 5. Planar Geometry

As in the previous chapter, we give explicit expressions for the effective weight functions. Planar geometry is characterised by invariance under translations in the $x$ and $y$ directions, and under rotations around the $z$ axis. Thus $\rho_{\mathrm{S}}(\mathbf{r}) = \rho_{\mathrm{S}}(z)$ and $\rho_{\mathrm{N}}(\mathbf{r}, \mathbf{\Omega}) = \rho_{\mathrm{N}}(z, \vartheta)$.

The weighted densities, Eq. (5.8-5.12), can then be expressed as

$$n_1^{\mathrm{SN}}(z,\vartheta) = \int_{-\infty}^{\infty} \rho_{\mathrm{S}}(z') w_1^{\mathrm{SN}}(z'-z,\vartheta)\,\mathrm{d}z', \tag{5.37}$$

$$n_{2\pm}^{\mathrm{SN}\Delta}(z,\vartheta) = \int_{-\infty}^{\infty} \rho_{\mathrm{S}}(z') w_{2\pm}^{\mathrm{SN}\Delta}(z'-z,\vartheta)\,\mathrm{d}z', \tag{5.38}$$

$$n_{1\pm}^{\mathrm{N}\Delta}(z,\vartheta) = \int_{-\infty}^{\infty} \rho_{\mathrm{N}}(z',\vartheta) w_{1\pm}^{\mathrm{N}\Delta}(z'-z,\vartheta)\,\mathrm{d}z', \tag{5.39}$$

$$n_2^{\mathrm{N}}(z,\vartheta) = \int_{-\infty}^{\infty} \rho_{\mathrm{N}}(z',\vartheta) w_2^{\mathrm{N}}(z'-z,\vartheta)\,\mathrm{d}z', \tag{5.40}$$

$$n_2^{\mathrm{NN}}(z,\vartheta') = \frac{1}{4\pi}\int_0^{\pi}\int_{-\infty}^{\infty} \rho_{\mathrm{N}}(z',\vartheta') w_2^{\mathrm{NN}}(z'-z,\vartheta';\vartheta)\,\mathrm{d}z'\,\mathrm{d}\vartheta', \tag{5.41}$$

where the effective weight functions are defined by

$$w_1^{\mathrm{SN}}(z,\vartheta) = \int_{-\infty}^{\infty}\int_{-\infty}^{\infty} w_1^{\mathrm{SN}}(\mathbf{r},\boldsymbol{\Omega})\,\mathrm{d}x\,\mathrm{d}y, \tag{5.42}$$

$$w_{2\pm}^{\mathrm{SN}\Delta}(z,\vartheta) = \int_{-\infty}^{\infty}\int_{-\infty}^{\infty} w_{2\pm}^{\mathrm{SN}\Delta}(\mathbf{r},\boldsymbol{\Omega})\,\mathrm{d}x\,\mathrm{d}y, \tag{5.43}$$

$$w_{1\pm}^{\mathrm{N}\Delta}(z,\vartheta) = \int_{-\infty}^{\infty}\int_{-\infty}^{\infty} w_{1\pm}^{\mathrm{N}\Delta}(\mathbf{r},\boldsymbol{\Omega})\,\mathrm{d}x\,\mathrm{d}y, \tag{5.44}$$

$$w_2^{\mathrm{N}}(z,\vartheta) = \int_{-\infty}^{\infty}\int_{-\infty}^{\infty} w_2^{\mathrm{N}}(\mathbf{r},\boldsymbol{\Omega})\,\mathrm{d}x\,\mathrm{d}y, \tag{5.45}$$

$$w_2^{\mathrm{NN}}(z,\vartheta;\vartheta') = \int_{-\infty}^{\infty}\int_{-\infty}^{\infty} w_2^{\mathrm{NN}}(\mathbf{r},\boldsymbol{\Omega};\boldsymbol{\Omega}')\,\mathrm{d}x\,\mathrm{d}y. \tag{5.46}$$

Carrying out the integrations, one obtains

$$w_1^{\mathrm{SN}}(z,\vartheta) = \frac{R}{\pi}\frac{\Theta(R|\sin\vartheta| - |z|)}{\sqrt{R^2\sin^2\vartheta - z^2}}, \tag{5.47}$$

$$w_{2\pm}^{\mathrm{SN}\Delta}(z,\vartheta) = \begin{cases} 0 & \text{if } z > R \\ 2\pi R & \text{if } R > \pm z > R\sin\vartheta \\ 0 & \text{if } -R\sin\vartheta > z \\ 2R\arccos\frac{|z\cot\vartheta|}{\sqrt{R^2-z^2}} & \text{else,} \end{cases} \tag{5.48}$$

$$w_{1\pm}^{\mathrm{N}\Delta}(\mathbf{r},\vartheta) = D\,\delta\left(z \pm \frac{L}{2}\cos\vartheta\right), \tag{5.49}$$

$$w_2^{\mathrm{N}}(\mathbf{r},\vartheta) = \frac{\pi D}{\cos\vartheta}\Theta\left(\frac{L}{2} - \frac{|z|}{\cos\vartheta}\right), \tag{5.50}$$

$$\begin{aligned} w_2^{\mathrm{NN}}(z,\vartheta;\vartheta') = {} & \frac{D\tan\vartheta}{\pi}\Theta\Big(\frac{L\cos\vartheta}{2} - |z|\Big) \\ & \times \int_0^{2\pi} \sqrt{1 - (\sin\vartheta'\sin\vartheta\cos\varphi + \cos\vartheta'\cos\vartheta)^2}\,\mathrm{d}\varphi. \end{aligned} \tag{5.51}$$

For the final effective weight function, one integral has to be solved numerically.

## 6. Conclusions

In conclusion we have extended the DFT of Refs. [105,116] and Chapter 4 to include effects of non-vanishing rod thickness. To that end we have introduced several qualitatively new weight functions into the geometric framework. Our theory accounts for excluded volume effects caused by finite rod aspect ratios, $D/L$. We emphasise, however, that although we treat the statistical weight associated with finite $D$, the present theory will not resolve features of density variation on length scales comparable to $D$. We also have only dealt with contributions of the order of $1/(1-n_3^{\mathrm{S}})$ to the excess free energy. Rosenfeld's prescription [101,122] also involves terms proportional to $1/(1-n_3^{\mathrm{S}})^2$, which we have not treated here. Whether the weight functions introduced in the present work can be used to modify these terms is an interesting problem that we leave for future research.

The proposed theory should lead to rich bulk phase behaviour as one has, besides demixing into fluid phases with different chemical composition of species, also the possibility of nematic ordering of rods. In turn this clearly leads to a rich variety of interesting interfacial situations. It would also be interesting to see how the present theory performs against other theoretical approaches or computer simulations. From the practical point of view the present functional causes only a moderate increase of computational complexity as the new weighted densities

for the sphere–rod Mayer bond are built with spatial convolutions only (although the angular convolution needed for the rod–rod Mayer bond is more involved).

CHAPTER 6

# Mixtures of Spheres, Thin Rods and Thin Platelets

## 1. Introduction

Dispersions of non-spherical colloidal particles are model systems to study phenomena in condensed matter ranging from fluid phase separation to the emergence of liquid crystalline phases. Example of such systems are clay suspensions [134, 135], gibbsite platelets [136], mixtures of silica spheres and silica-coated boehmite rods [137], or wax disks [138]. For binary mixtures the phase behaviour is considerably richer than for pure systems, due to the additional possibility of demixing into bulk phases with different chemical compositions, e.g. in dispersions of disks and spheres [138].

Theoretical work has been devoted to fluids of platelike particles near a hard wall [139], an interaction site model for lamellar colloids [140], wetting and capillary nematisation of binary hard-platelet and hard-rod fluids [21], the lamellar Zwanzig model [22, 23], and colloidal hard-rod fluids near geometrically structured substrates [141]. The phase diagram of mixtures of hard colloidal spheres and discs was obtained within a free-volume scaled particle approach [142]. The depletion potential between two spheres immersed in a sea of platelets was studied in detail [143, 144], and the Derjaguin approximation was found to be quite accurate for this case [143]. Sedimentation was found to influence liquid crystal phase transitions of colloidal platelets [25], as well as multi-phase equilibria in mixtures of platelets and ideal polymer [145].

The fundamental-measure theory (FMT) is an (approximate) density-functional theory (DFT) [94, 95] originally proposed by Rosenfeld for additive hard sphere mixtures [96]. Early extensions to more general non-spherical shapes have been given [101, 122]. This theory, when applied to homogeneous and isotropic fluid states, does recover the correct second virial coefficient of the equation of state, but fails to recover the exact density functional up to second order in density. To remedy this problem, an interpolation between the hard sphere Rosenfeld functional and the Onsager functional for elongated rods was proposed in Ref. [132] and applied to the bulk isotropic-nematic transition.

The Bolhuis-Frenkel model of hard spheres and vanishingly thin hard needles [86] can be considered as the simplest model hard core mixture of spheres and rods. Previous work was devoted to the formulation of a DFT for this model [105], and an extension to include rod–rod interactions on the Onsager

(second virial) level [116, 146] has been proposed. Predictions for the orientation ordering of the rods at a free interface between (isotropic) sphere-rich and sphere-poor phases [116] were successfully confirmed by simulations [123]. The fluid demixing phase behaviour of ternary mixtures of spheres, rods, and model polymers was considered [107]. Hard spheres were considered in random rod networks [147], and the isotropic-nematic transition of rods in matrices of quenched (immobilised) spheres was investigated [148].

Central to FMT is the so-called deconvolution of the Mayer bond into *weight functions* that are characteristic of the shape of the particles. The Mayer bond is $f_{ij} = \exp(-\beta V_{ij}) - 1$ for a given pair interaction potential $V_{ij}$ between species $i$ and $j$, where $\beta = 1/(kT)$, $k$ is the Boltzmann constant and $T$ is temperature. Such weight functions have been obtained for hard sphere mixtures in Ref. [96] and for the Mayer bond between a sphere and a vanishingly thin needle in Ref. [105], curing, for this particular model, the defect of Rosenfeld's initial formulation for non-convex bodies [101, 122].

Here we show how to treat platelet-shaped particles and their mixtures with spheres and needles within the same framework. The relevant weight functions are given and it is shown explicitly how the Mayer bonds for the ternary mixture are obtained through convolutions. For two-dimensional hard disks, the Rosenfeld functional only approximately yields the Mayer bond. Despite this deficiency this theory is considered to be a useful tool to study inhomogeneous situations, see e.g. Ref. [149] for an investigation of laser-induced freezing and melting of confined colloidal particles. The treatment of the sphere-platelet case inevitably leads to the same (arguably small) deficiency, while we achieve an exact deconvolution of the Mayer bonds for platelet-platelet and platelet-needle interactions.

Harnau and Dietrich recently considered bulk and wetting phenomena in a similar binary mixture of colloidal hard spheres and hard platelets [150]. We will discuss the relationship of the current work to Ref. [150] in detail in Sec. 7, after having laid out our approach.

## 2. Model

We consider a mixture of hard spheres (species $S$) with diameter $\sigma = 2R$, where $R$ is the radius, hard platelets (species $D$) of diameter $2R_{\mathrm{D}}$ and vanishing thickness, and hard needle-like rods (species $N$) of length $L$ and again vanishing thickness. The pair interaction potential $V_{ij}$ between any two particles of species $i, j = S, D, N$ is infinite if their geometrical shapes overlap and zero otherwise. The one-body density distribution of species $i = S, D, N$ is denoted by $\rho_{\mathrm{S}}(\mathbf{r})$, $\rho_{\mathrm{D}}(\mathbf{r}, \mathbf{\Omega})$, and $\rho_{\mathrm{N}}(\mathbf{r}, \mathbf{\Omega})$, respectively, where $\mathbf{r}$ is the position of the particle centre, and $\mathbf{\Omega}$ is a unit vector pointing along (normal to) the shape of the needle (platelet), thus describing its orientation in space.

## 3. Deconvolution of the Mayer bonds

**3.1. The sphere-sphere and sphere-needle Mayer bonds.** For completeness we first summarise results from the literature for hard spheres and their mixtures with needles. Rosenfeld's hard sphere weight functions [96] are

$$w_3^{\mathrm{S}}(\mathbf{r}) = \Theta(R - |\mathbf{r}|), \tag{6.1}$$

$$w_2^{\mathrm{S}}(\mathbf{r}) = \delta(R - |\mathbf{r}|), \tag{6.2}$$

$$\mathbf{w}_{\mathrm{v}2}^{\mathrm{S}}(\mathbf{r}) = w_2^{\mathrm{S}}(\mathbf{r})\frac{\mathbf{r}}{|\mathbf{r}|}, \tag{6.3}$$

where $\Theta(\cdot)$ is the unit step (Heaviside) function and $\delta(\cdot)$ is the Dirac distribution. Here and in the following the $w_\tau^i$ are quantities with the dimension of (length)$^{\tau-3}$; the subscript v indicates vectorial quantities. Further, linearly dependent, weight functions are $w_1^{\mathrm{S}}(\mathbf{r}) = w_2^{\mathrm{S}}(\mathbf{r})/(4\pi R)$, $w_0^{\mathrm{S}}(\mathbf{r}) = w_2^{\mathrm{S}}(\mathbf{r})/(4\pi R^2)$, and $\mathbf{w}_{\mathrm{v}1}^{\mathrm{S}}(\mathbf{r}) = \mathbf{w}_{\mathrm{v}2}^{\mathrm{S}}(\mathbf{r})/(4\pi R)$. For pure hard spheres the Mayer bond is obtained through

$$-f_{\mathrm{SS}}(\mathbf{r})/2 = w_3^{\mathrm{S}}(\mathbf{r}) * w_0^{\mathrm{S}}(\mathbf{r}) + w_2^{\mathrm{S}}(\mathbf{r}) * w_1^{\mathrm{S}}(\mathbf{r}) - \mathbf{w}_{\mathrm{v}2}^{\mathrm{S}}(\mathbf{r}) * \mathbf{w}_{\mathrm{v}1}^{\mathrm{S}}(\mathbf{r}), \tag{6.4}$$

where the (three-dimensional) convolution is defined as

$$h(\mathbf{r}) * g(\mathbf{r}) = \int h(\mathbf{x})g(\mathbf{x}-\mathbf{r})\,\mathrm{d}^3x$$

and also implies a scalar product between vectors, as appears in the last term on the right hand side of Eq. (6.4).

Vanishingly thin needles do not experience excluded volume, but do interact with hard spheres. For such binary mixture the needles' weight functions used in Ref. [105] were obtained from the prescription of Refs. [101, 122], and are given by

$$w_0^{\mathrm{N}}(\mathbf{r}, \mathbf{\Omega}) = \frac{1}{2}\left[\delta\left(\mathbf{r} - \frac{L}{2}\mathbf{\Omega}\right) + \delta\left(\mathbf{r} + \frac{L}{2}\mathbf{\Omega}\right)\right], \tag{6.5}$$

$$w_1^{\mathrm{N}}(\mathbf{r}, \mathbf{\Omega}) = \frac{1}{4}\int_{-L/2}^{L/2} \delta(\mathbf{r} - l\mathbf{\Omega})\,\mathrm{d}l. \tag{6.6}$$

Introducing a "mixed" weight function that is non-vanishing on the surface of a sphere, but carries a dependence on orientation,

$$w_2^{\mathrm{SN}}(\mathbf{r}, \mathbf{\Omega}) = 2|\mathbf{w}_{\mathrm{v}2}^{\mathrm{S}}(\mathbf{r}) \cdot \mathbf{\Omega}|, \tag{6.7}$$

allows one to obtain the Mayer bond between sphere and needle through convolutions,

$$-f_{\mathrm{SN}}(\mathbf{r}, \mathbf{\Omega}) = w_3^{\mathrm{S}}(\mathbf{r}) * w_0^{\mathrm{N}}(\mathbf{r}, \mathbf{\Omega}) + w_2^{\mathrm{SN}}(\mathbf{r}, \mathbf{\Omega}) * w_1^{\mathrm{N}}(\mathbf{r}, \mathbf{\Omega}). \tag{6.8}$$

For the case of residual rod-rod interactions in the Onsager limit, $f_{\mathrm{NN}}$ can also be deconvolved into weight functions, see Chapter 5. In the following, however, we will restrict ourselves to vanishingly thin needles.

**3.2. Strictly two-dimensional hard disks.** As a prerequisite for our subsequent treatment of platelets with a rotational degree of freedom in three dimensions, we give an overview of Rosenfeld's functional for the simpler model of strictly two-dimensional disks. We need, however, to deal with a multicomponent mixture with radii $R_i$ of species $i$, and characterised by the pair potential $V_{ij}(r) = \infty$ if $r < R_i + R_j$ and zero otherwise, where $r$ is the centre-centre distance between the disks of species $i$ and $j$. (Of course, when viewed from the viewpoint of the three-dimensional model, all disks possess the same orientation $\mathbf{\Omega}$, perpendicular to the 2d plane of position coordinates). Rosenfeld's weight functions are

$$w_2^{(i)}(\mathbf{r}) = \Theta(R_i - |\mathbf{r}|), \tag{6.9}$$

$$w_1^{(i)}(\mathbf{r}) = \delta(R_i - |\mathbf{r}|), \tag{6.10}$$

$$\mathbf{w}_{\mathrm{v1}}^{(i)}(\mathbf{r}) = w_2^{(i)}(\mathbf{r})\frac{\mathbf{r}}{|\mathbf{r}|}, \tag{6.11}$$

and there is an additional, linearly dependent weight function,

$$w_0^{(i)}(\mathbf{r}) = w_2^{(i)}(\mathbf{r})/(2\pi R_i),$$

corresponding to the Euler characteristic.

The exact Mayer bond $f_{ij}$ is then approximated through $f_{ij} \approx f_{ij}^*$, where

$$\begin{aligned} -f_{ij}^*(r) = {} & w_0^{(i)}(\mathbf{r}) * w_2^{(j)}(\mathbf{r}) + w_2^{(i)}(\mathbf{r}) * w_0^{(j)}(\mathbf{r}) \\ & + \frac{1}{2\pi}\Big(w_1^{(i)}(\mathbf{r}) * w_1^{(j)}(\mathbf{r}) - \mathbf{w}_{\mathrm{v1}}^{(i)}(\mathbf{r}) * \mathbf{w}_{\mathrm{v1}}^{(j)}(\mathbf{r})\Big), \end{aligned} \tag{6.12}$$

where here (and only here) $*$ denotes the two-dimensional convolution,

$$h(\mathbf{r}) * g(\mathbf{r}) = \int h(\mathbf{x})g(\mathbf{x}-\mathbf{r})\,\mathrm{d}^2x,$$

and again implies a scalar product between vectors.

As our treatment of the three-dimensional sphere-platelet case below relies heavily on Eq. (6.12), we will obtain an explicit expression for $f_{ij}^*$ and discuss some of its properties. We choose 2d Cartesian coordinates $\mathbf{r}$ and $\mathbf{x}$, such that $\mathbf{r} = (0, r), \mathbf{x} = (x' \sin\varphi', x' \cos\varphi')$, which allows us to write

$$\int w_0^{(i)}(\mathbf{x}) w_2^{(j)}(\mathbf{x}-\mathbf{r})\,\mathrm{d}^2x$$

$$= \int_0^{2\pi}\int_0^{\infty} \frac{1}{2\pi R_i}\delta(x'-R_i)\Theta\Big(R_j - \sqrt{x'^2+r^2-2rx'\cos\varphi'}\Big)\, x'\,\mathrm{d}x'\,\mathrm{d}\varphi' \tag{6.13}$$

$$= \frac{1}{\pi}\arccos\Big(\frac{r^2+R_i^2-R_j^2}{2rR_i}\Big)\,\Theta\big(2rR_i - \big|r^2+R_i^2-R_j^2\big|\big) \tag{6.14}$$

By the cosine theorem, this is equal (up to a factor of $2\pi$) to the length of the arc which the rim of the left disc traces across the interior of the right one (see Figure 2).

To get the Mayer function from the original Rosenfeld functional, the term $(w_1 * w_1 - \mathbf{w}_{\mathrm{v1}} * \mathbf{w}_{\mathrm{v1}})/(2\pi)$ remains to be calculated. Using the same assumptions as before, we obtain:

$$\frac{1}{2\pi}\int w_1^{(i)}(\mathbf{x}) w_1^{(j)}(\mathbf{x}-\mathbf{r}) - \mathbf{w}_{\mathrm{v1}}^{(i)}(\mathbf{x})\mathbf{w}_{\mathrm{v1}}^{(j)}(\mathbf{x}-\mathbf{r})\,\mathrm{d}^2x$$

$$= \frac{1}{2\pi}\int_0^{2\pi}\int_0^{\infty} \delta\left(R_i - x'\right)\,\delta\left(R_j - \sqrt{r^2+x'^2-2rx'\cos\varphi'}\right) \times \left(1 - \frac{1}{R_iR_j}\begin{pmatrix} x'\sin\varphi' \\ x'\cos\varphi' \end{pmatrix}\cdot\begin{pmatrix} x'\sin\varphi' \\ x'\cos\varphi'-r \end{pmatrix}\right) x'\,\mathrm{d}x'\,\mathrm{d}\varphi' \tag{6.15}$$

$$= \frac{1}{\pi}\Theta(R_i - |R_j - r|)\,\frac{r^2-(R_i-R_j)^2}{\sqrt{4r^2R_i^2-(r^2+R_i^2-R_j^2)^2}} \tag{6.16}$$

In the special case that both platelets have the same radius, $R_i = R_j$, as relevant for describing the pure hard disk system, the above expression further simplifies to

$$\frac{1}{2\pi}\int w_1^{(i)}(\mathbf{x}) w_1^{(i)}(\mathbf{x}-\mathbf{r}) - \mathbf{w}_{\mathrm{v1}}^{(i)}(\mathbf{x})\mathbf{w}_{\mathrm{v1}}^{(i)}(\mathbf{x}-\mathbf{r})\,\mathrm{d}^2x$$

$$= \frac{1}{\pi}\Theta(2R_i - r)\,\frac{r}{\sqrt{4R_i^2-r^2}}. \tag{6.17}$$

**3.3. Platelet-platelet Mayer bond in three dimensions.** Returning to three dimensions, direct application of Rosenfeld's recipe [101, 122] to platelets

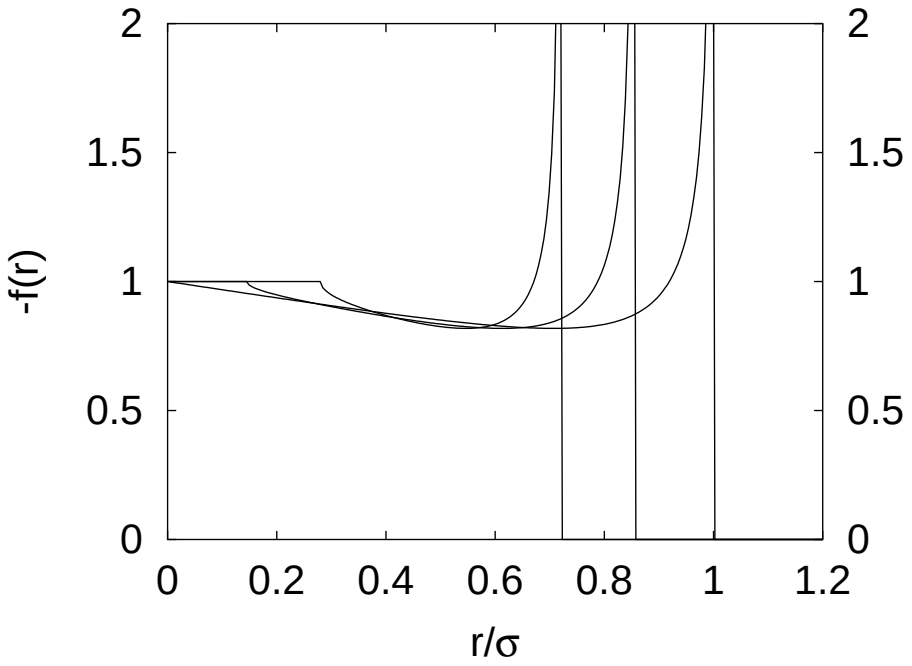


FIGURE 1. The Mayer bond between two-dimensional hard disks of radii $R_1/R_2 = 1, 0.71, 0.44$ (right to left) is shown as a function of the centre-to-centre distance of the two disks. This is also the Mayer bond of a sphere and disk of equal radius as a function of the distance between the centre of the platelet and the sphere's axis (parallel to the orientation $\mathbf{\Omega}$ of the platelet). The distance between the centre of the sphere and the plane of the platelet is $0, 0.7, 0.9$ (right to left). Note that whenever the platelet fully cuts through the sphere, the Mayer bond obtained is exact.

yields the scalar weight functions

$$w_2^{\mathrm{D}}(\mathbf{r}, \mathbf{\Omega}) = 2\Theta(R_{\mathrm{D}} - |\mathbf{r}|)\delta(\mathbf{r} \cdot \mathbf{\Omega}), \tag{6.18}$$

$$w_1^{\mathrm{D}}(\mathbf{r}, \mathbf{\Omega}) = \frac{1}{8}\delta(R_{\mathrm{D}} - |\mathbf{r}|)\delta(\mathbf{r} \cdot \mathbf{\Omega}), \tag{6.19}$$

$$w_0^{\mathrm{D}}(\mathbf{r}, \mathbf{\Omega}) = \frac{1}{2\pi R_{\mathrm{D}}}\delta(R_{\mathrm{D}} - |\mathbf{r}|)\delta(\mathbf{r} \cdot \mathbf{\Omega}), \tag{6.20}$$

corresponding to the surface, $\xi_2^{\mathrm{D}} = 2\pi R_{\mathrm{D}}^2$, integral mean curvature, $\xi_1^{\mathrm{D}} = \pi R_{\mathrm{D}}/4$, and Euler characteristic, $\xi_0^{\mathrm{D}} = 1$, of the platelets, respectively. The remaining scalar weight function that describes the particle volume vanishes, $w_3^{\mathrm{S}}(\mathbf{r}, \mathbf{\Omega}) = 0$, due to the vanishing thickness, and hence vanishing volume of the platelets, $\xi_3^{\mathrm{D}} = 0$.

In contrast to the result of Rosenfeld's use of vectorial weight functions [101, 122], we here aim at an exact deconvolution of $f_{\mathrm{DD}}(\mathbf{r}, \mathbf{\Omega}', \mathbf{\Omega})$, where $\mathbf{r}$ is the

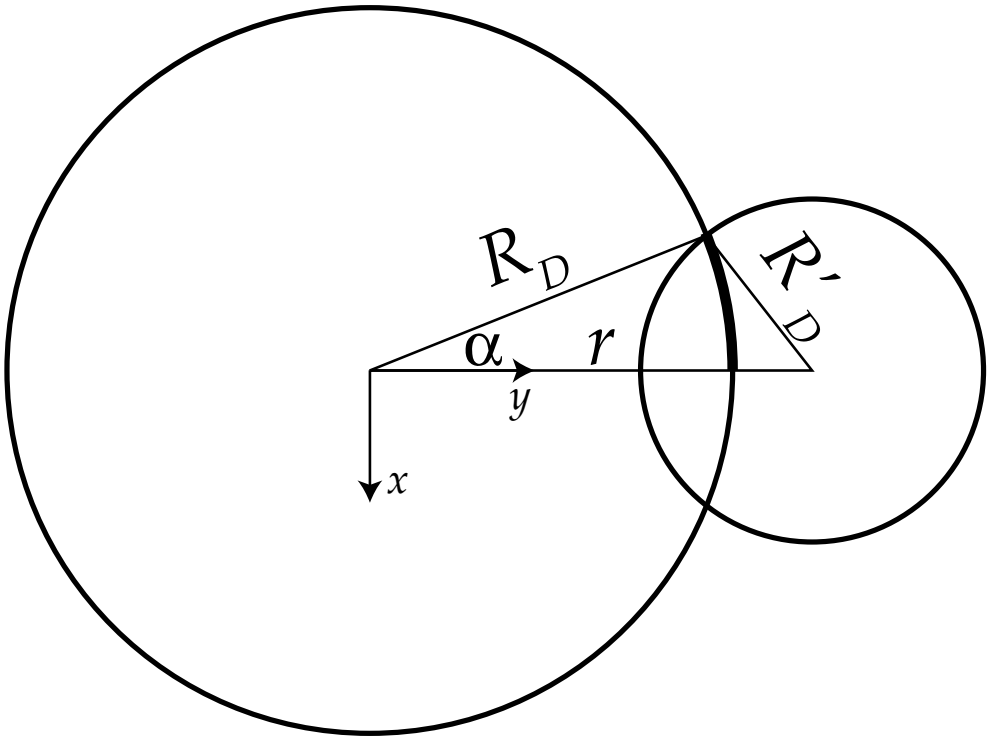


FIGURE 2. Overlapping pair of strictly two-dimensional hard disks with radii $R_i$ and $R_j$ and centre-centre distance $r$. Shown are the $x$ and $y$ axis of the coordinate system used, the angle $\alpha$ (that can be calculated by the cosine theorem) between the y-axis and $R_i$, as well as half of the part (bold) of the circumference of disk $i$ that lies inside disk $j$.

centre-centre distance vector between both particles and $\mathbf{\Omega}$ and $\mathbf{\Omega}'$ are their orientations. We introduce

$$w_1^{\mathrm{DD}}(\mathbf{r},\mathbf{\Omega};\mathbf{\Omega}') = \frac{2}{R_{\mathrm{D}}}|\mathbf{\Omega}\cdot(\mathbf{\Omega}'\times\mathbf{r})|w_1^{\mathrm{D}}(\mathbf{r},\mathbf{\Omega}), \tag{6.21}$$

and keep Rosenfeld's surface weight function, $w_2^{\mathrm{D}}(\mathbf{r},\mathbf{\Omega})$, as given in Eq. (6.18), in order to recover the Mayer bond between platelets via

$$\begin{aligned} -f_{\mathrm{DD}}(\mathbf{r},\mathbf{\Omega};\mathbf{\Omega}') = {} & w_1^{\mathrm{DD}}(\mathbf{r},\mathbf{\Omega};\mathbf{\Omega}') * w_2^{\mathrm{D}}(\mathbf{r},\mathbf{\Omega}') \\ & + w_2^{\mathrm{D}}(\mathbf{r},\mathbf{\Omega}) * w_1^{\mathrm{DD}}(\mathbf{r},\mathbf{\Omega}';\mathbf{\Omega}). \end{aligned} \tag{6.22}$$

As this expression consists of two symmetric terms, it is sufficient to consider the first, the second one gives the same contribution to $f_{\mathrm{DD}}$.

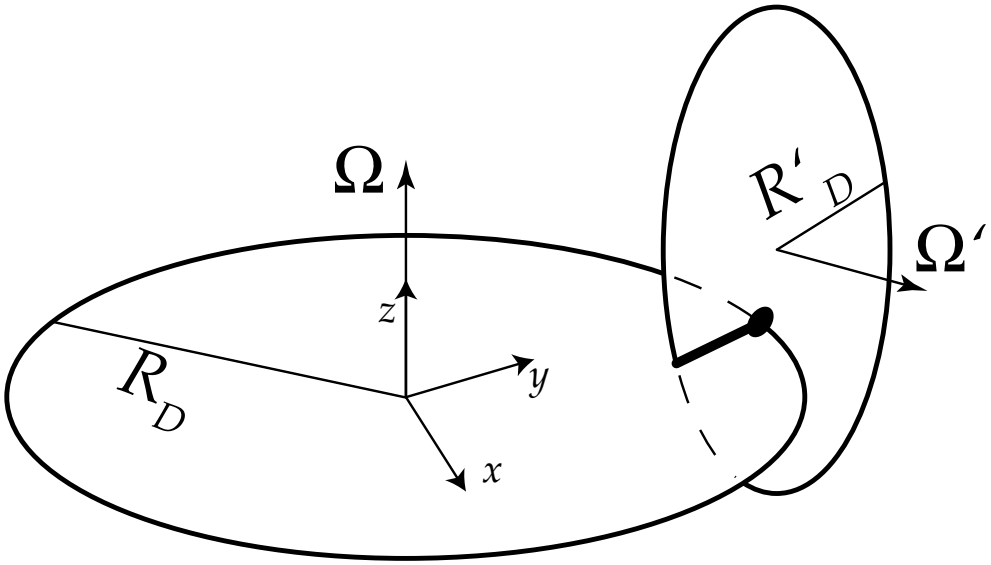


FIGURE 3. Setup for the calculation of the platelet–platelet Mayer bond. Platelet $D$ is located in the $x$–$y$-plane with its centre at the origin. Platelet $D'$ has its centre in the $y$–$z$-plane and an arbitrary orientation. The calculation checks for the intersection of the rim of $D$ and the interior of $D'$ (bold dot). The one-dimensional overlap volume of the two platelets is shown as a bold line.

Without loss of generality we place the particles such that one platelet shall be located at the origin with its orientation vector pointing up. The other platelet lies in the $y$–$z$ plane, see Figure 3 for an illustration of the coordinates chosen:

$$\mathbf{r} = (0, r, z) \qquad \mathbf{\Omega} = (0, 0, 1) \qquad \mathbf{\Omega}' = (\sqrt{1-\bar{z}^2}\sin\bar{\varphi}, \sqrt{1-\bar{z}^2}\cos\bar{\varphi}, \bar{z});$$

the integration variable is $\mathbf{x} = (r'\sin\varphi', r'\cos\varphi', z')$. With the weight function

$$w_1^{\mathrm{DD}}(\mathbf{r}, \mathbf{\Omega}; \mathbf{\Omega}') = \frac{1}{4R_{\mathrm{D}}} \left|\mathbf{\Omega}' \cdot (\mathbf{r} \times \mathbf{\Omega})\right| \, \delta\left(R_{\mathrm{D}} - |\mathbf{r}|\right) \, \delta\left(\mathbf{r} \cdot \mathbf{\Omega}\right), \tag{6.23}$$

we obtain:

$$\begin{aligned}
&\int w_1^{\mathrm{DD}}(\mathbf{x}, \mathbf{\Omega}; \mathbf{\Omega}') w_2^{\mathrm{D}}(\mathbf{x} - \mathbf{r}, \mathbf{\Omega}') \, \mathrm{d}^3 x \\
&\quad = \frac{1}{2R_{\mathrm{D}}} \int_0^{2\pi} \int_{-\infty}^{\infty} \int_0^{\infty} \left| \begin{pmatrix} 0 \\ 0 \\ 1 \end{pmatrix} \cdot \left[ \begin{pmatrix} \sqrt{1-\bar{z}^2}\sin\bar{\varphi} \\ \sqrt{1-\bar{z}^2}\cos\bar{\varphi} \\ \bar{z} \end{pmatrix} \times \begin{pmatrix} r'\sin\varphi' \\ r'\cos\varphi' \\ z' \end{pmatrix} \right] \right| \\
&\qquad \times \, \delta\left(R_{\mathrm{D}} - \sqrt{r'^2 + z'^2}\right) \, \delta\left(z'\right) \Theta(R_{\mathrm{D}} - |(r'\sin\varphi', r'\cos\varphi' - r, z' - z)|) \\
&\qquad \times \, \delta\left( \begin{pmatrix} r'\sin\varphi' \\ r'\cos\varphi' - r \\ z' - z \end{pmatrix} \cdot \begin{pmatrix} \sqrt{1-\bar{z}^2}\sin\bar{\varphi} \\ \sqrt{1-\bar{z}^2}\cos\bar{\varphi} \\ \bar{z} \end{pmatrix} \right) r' \, \mathrm{d}r' \, \mathrm{d}z' \, \mathrm{d}\varphi'
\end{aligned} \tag{6.24}$$

$$
\begin{aligned}
&= \frac{R_{\mathrm{D}}}{2} \int_0^{2\pi} \left| \begin{pmatrix} \sin\varphi' \\ \cos\varphi' \\ 0 \end{pmatrix} \cdot \begin{pmatrix} -\sqrt{1-\bar{z}^2}\cos\bar{\varphi} \\ \sqrt{1-\bar{z}^2}\sin\bar{\varphi} \\ 0 \end{pmatrix} \right| \\
&\quad \times \Theta(R_{\mathrm{D}} - |(R_{\mathrm{D}}\sin\varphi', R_{\mathrm{D}}\cos\varphi' - r, -z)|) \\
&\quad \times \delta\left( \begin{pmatrix} R_{\mathrm{D}}\sin\varphi' \\ R_{\mathrm{D}}\cos\varphi' - r \\ -z \end{pmatrix} \cdot \begin{pmatrix} \sqrt{1-\bar{z}^2}\sin\bar{\varphi} \\ \sqrt{1-\bar{z}^2}\cos\bar{\varphi} \\ \bar{z} \end{pmatrix} \right) \mathrm{d}\varphi'
\end{aligned} \tag{6.25}
$$

$$
\begin{aligned}
&= \frac{R_{\mathrm{D}}}{2} \int_0^{2\pi} \left| \sqrt{1-\bar{z}^2}\cos\varphi'\sin\bar{\varphi} - \sqrt{1-\bar{z}^2}\sin\varphi'\cos\bar{\varphi} \right| \\
&\quad \times \Theta\Big( R_{\mathrm{D}} - \sqrt{R_{\mathrm{D}}^2 + r^2 + z^2 - 2rR_{\mathrm{D}}\cos\varphi'} \Big) \\
&\quad \times \delta\left( (r - R_{\mathrm{D}}\cos\varphi')\sqrt{1-\bar{z}^2}\cos\bar{\varphi} - R_{\mathrm{D}}\sqrt{1-\bar{z}^2}\sin\varphi'\sin\bar{\varphi} + z\bar{z} \right) \mathrm{d}\varphi'
\end{aligned} \tag{6.26}
$$

$$
\begin{aligned}
&= \frac{R_{\mathrm{D}}}{2} \int_0^{2\pi} \left| \sqrt{1-\bar{z}^2}\sin(\bar{\varphi} - \varphi') \right| \Theta\big(2rR_{\mathrm{D}}\cos\varphi' - r^2 - z^2\big) \\
&\quad \times \delta\left( r\sqrt{1-\bar{z}^2}\cos\bar{\varphi} - R_{\mathrm{D}}\sqrt{1-\bar{z}^2}\cos(\varphi' - \bar{\varphi}) + z\bar{z} \right) \mathrm{d}\varphi'
\end{aligned} \tag{6.27}
$$

$$
\begin{aligned}
&= \frac{1}{2}\Bigg[ \Theta\Bigg( 2rR_{\mathrm{D}}\cos\left( \arccos\frac{r\sqrt{1-\bar{z}^2}\cos\bar{\varphi} + z\bar{z}}{R_{\mathrm{D}}\sqrt{1-\bar{z}^2}} + \bar{\varphi} \right) - r^2 - z^2 \Bigg) \\
&\quad + \Theta\Bigg( 2rR_{\mathrm{D}}\cos\left( 2\pi - \arccos\frac{r\sqrt{1-\bar{z}^2}\cos\bar{\varphi} + z\bar{z}}{R_{\mathrm{D}}\sqrt{1-\bar{z}^2}} + \bar{\varphi} \right) - r^2 - z^2 \Bigg) \Bigg] \\
&\quad \times \Theta\Big( R_{\mathrm{D}}\sqrt{1-\bar{z}^2} - \left| r\sqrt{1-\bar{z}^2}\cos\bar{\varphi} + z\bar{z} \right| \Big)
\end{aligned} \tag{6.28}
$$

$$
\begin{aligned}
&= \frac{1}{2}\sum_{\pm} \Theta\Bigg( 2rR_{\mathrm{D}}\cos\left( \bar{\varphi} \pm \arccos\frac{r\sqrt{1-\bar{z}^2}\cos\bar{\varphi} + z\bar{z}}{R_{\mathrm{D}}\sqrt{1-\bar{z}^2}} \right) - r^2 - z^2 \Bigg) \\
&\quad \times \Theta\Big( R_{\mathrm{D}}\sqrt{1-\bar{z}^2} - \left| r\sqrt{1-\bar{z}^2}\cos\bar{\varphi} + z\bar{z} \right| \Big)
\end{aligned} \tag{6.29}
$$

The integrals in Eq. (6.24) over $z'$ and $r'$ can be calculated in a straightforward manner. From (6.26) to (6.27), we rewrote the argument of the Dirac delta in such a way that $\varphi'$ appears only once, using the identity $\sin\varphi'\sin\bar{\varphi} + \cos\varphi'\cos\bar{\varphi} = \cos(\varphi' - \bar{\varphi})$.

Given the complexity of the overlap condition between two arbitrarily oriented platelets in three dimensions, it is not surprising that Eq. (6.29) is an

involved expression. It can be viewed as counting the number of intersections between the platelet $D'$ and the rim of platelet $D$ [1].

**3.4. The platelet-needle Mayer bond.** In order to obtain the platelet-needle Mayer bond, $f_{\mathrm{DN}}$, we define a "mixed" weight function for the platelets that is non-vanishing on the platelet surface (with surface normal $\mathbf{\Omega}_{\mathrm{D}}$), but carries an additional dependence on the rod orientation $\mathbf{\Omega}_{\mathrm{N}}$,

$$w_2^{\mathrm{DN}}(\mathbf{r}, \mathbf{\Omega}_{\mathrm{D}}; \mathbf{\Omega}_{\mathrm{N}}) = |\mathbf{\Omega}_{\mathrm{D}} \cdot \mathbf{\Omega}_{\mathrm{N}}| w_2^{\mathrm{D}}(\mathbf{r}, \mathbf{\Omega}_{\mathrm{D}}). \tag{6.30}$$

This allows us to obtain the Mayer bond between platelet and needle via

$$-f_{\mathrm{DN}}(\mathbf{r}, \mathbf{\Omega}_{\mathrm{D}}; \mathbf{\Omega}_{\mathrm{N}}) = w_2^{\mathrm{DN}}(\mathbf{r}, \mathbf{\Omega}_{\mathrm{D}}; \mathbf{\Omega}_{\mathrm{N}}) * w_1^{\mathrm{N}}(\mathbf{r}, \mathbf{\Omega}_{\mathrm{N}}). \tag{6.31}$$

Employing cylindrical coordinates, put the platelet on the $y$-axis, its orientation vector being $\mathbf{e}_z$. Position the needle in such a way that its intersection with the $x$–$y$-plane is the origin (cf. Figure 4).

The needle is described by

$$\begin{aligned} \mathbf{r}_{\mathrm{N}} &= (z_{\mathrm{N}}/\bar{z}\sqrt{1-\bar{z}^2}\sin\bar{\varphi}, z_{\mathrm{N}}/\bar{z}\sqrt{1-\bar{z}^2}\cos\bar{\varphi}, z_{\mathrm{N}}) \\ \mathbf{\Omega}_{\mathrm{N}} &= (\sqrt{1-\bar{z}^2}\sin\bar{\varphi}, \sqrt{1-\bar{z}^2}\cos\bar{\varphi}, \bar{z}). \end{aligned}$$

The coordinates of the platelet are $\mathbf{r}_{\mathrm{D}} = (0, r_{\mathrm{D}}, 0)$ and $\mathbf{\Omega}_{\mathrm{D}} = (0, 0, 1)$; the integration variable is $\mathbf{x} = (x'\sin\varphi', x'\cos\varphi', z')$.

With the weight function

$$w_2^{\mathrm{DN}}(\mathbf{r}, \mathbf{\Omega}_{\mathrm{D}}; \mathbf{\Omega}_{\mathrm{N}}) = 4\Theta(R_{\mathrm{D}} - |\mathbf{r}|)\ \delta(\mathbf{r} \cdot \mathbf{\Omega}_{\mathrm{D}})\, |\mathbf{\Omega}_{\mathrm{D}} \cdot \mathbf{\Omega}_{\mathrm{N}}|\,, \tag{6.32}$$

we obtain:

[1] We use $D$ and $D'$ to refer both to the platelets and the points of their origins. Consider the triangle $\Delta$ between the centre of platelet $D$, the intersection $I$ of platelet $D'$ with the rim of $D$, and the centre of $D'$ projected onto the $x$–$y$ plane (call this point $A$). This triangle has by construction two known sides, $R_{\mathrm{D}}$ and $r$. The length of the third side of $\Delta$ can be calculated by the cosine theorem from the angle $\angle ADI$. Using the Pythagorean theorem on the triangle between $I$ and the real and projected centres of $D'$, the length $|\overline{D'I}|$ can be calculated and compared to the radius of $D'$, $R_{\mathrm{D}}$. This is accomplished by the first step function. In order to calculate the angle needed for the cosine theorem, consider $\Delta$ and the right-angled triangle $\Delta'$ that is obtained by continuing $\overline{AI}$ over $I$ to form a right angle at the new point $B$. Then, $|\overline{AB}| = |r\cos\bar{\varphi}|$ and $|\overline{AI}| = z\bar{z}/\sqrt{1-\bar{z}^2}$. Therefore, the arccos equals the angle $\angle DIB$, and we obtain the angle $\angle ADI$ by adding $\bar{\varphi}$. The second step function in Eq. (6.29) checks if the plane defined by $D'$ intersects with the rim of $D$.

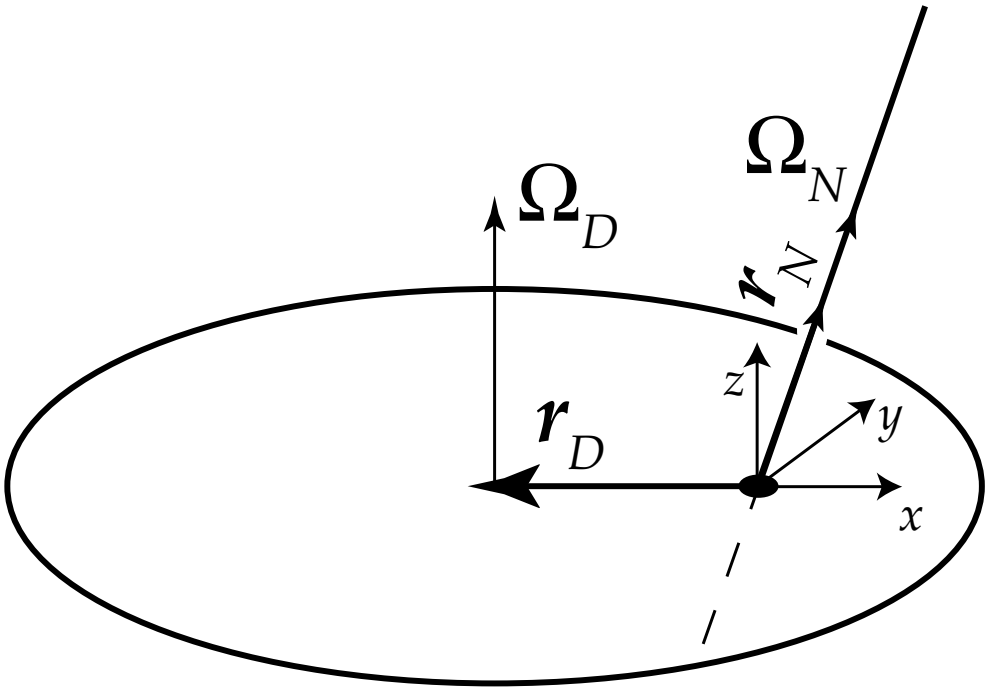


FIGURE 4. Setup for the calculation of the platelet–needle Mayer bond. The needle is located at $\mathbf{r}_{\mathrm{N}}$ in such a way that it points at the origin. The platelet is located at $\mathbf{r}_{\mathrm{D}}$.

$$-f_{\mathrm{DN}}(\mathbf{r},\boldsymbol{\Omega}_{\mathrm{D}};\boldsymbol{\Omega}_{\mathrm{N}}) = \int w_1^{\mathrm{N}}(\mathbf{x}-\mathbf{r}_{\mathrm{N}},\boldsymbol{\Omega}_{\mathrm{N}}) w_2^{\mathrm{DN}}(\mathbf{x}-\mathbf{r}_{\mathrm{D}},\boldsymbol{\Omega}_{\mathrm{D}};\boldsymbol{\Omega}_{\mathrm{N}})\,\mathrm{d}^3x \tag{6.33}$$

$$\begin{aligned}
&= \int_{-\infty}^{\infty}\int_{0}^{2\pi}\int_{0}^{\infty}\int_{-L/2}^{L/2} \delta\left(x'\sin\varphi' - z_{\mathrm{N}}/\bar{z}\sqrt{1-\bar{z}^2}\sin\bar{\varphi} + l\sqrt{1-\bar{z}^2}\sin\bar{\varphi}\right) \\
&\quad\times\ \delta\left(x'\cos\varphi' - z_{\mathrm{N}}/\bar{z}\sqrt{1-\bar{z}^2}\cos\bar{\varphi} + l\sqrt{1-\bar{z}^2}\cos\bar{\varphi}\right) \\
&\quad\times \delta(z'-z_{\mathrm{N}}+l\bar{z})\Theta(R_{\mathrm{D}}-|(x'\sin\varphi', x'\cos\varphi'-r_{\mathrm{D}}, z')|) \\
&\quad\times |\bar{z}|\delta(z')\,\mathrm{d}l\,x'\,\mathrm{d}x'\,\mathrm{d}\varphi'\,\mathrm{d}z'
\end{aligned} \tag{6.34}$$

$$\begin{aligned}
&= \int_{0}^{2\pi}\int_{0}^{\infty} \delta\left(x'\sin\varphi'\right)\,\delta\left(x'\cos\varphi'\right) \\
&\quad\times \Theta(R_{\mathrm{D}}-|(x'\sin\varphi', x'\cos\varphi'-r_{\mathrm{D}})|)\,\Theta\!\left(\frac{L}{2}|\bar{z}|-|z_{\mathrm{N}}|\right)\,x'\,\mathrm{d}x'\,\mathrm{d}\varphi'
\end{aligned} \tag{6.35}$$

$$= \Theta(R_{\mathrm{D}}-r_{\mathrm{D}})\,\Theta\!\left(\frac{L}{2}|\bar{z}|-|z_{\mathrm{N}}|\right) \tag{6.36}$$

The integrals over $z'$ and $l$ are straightforward. In Eq. (6.35), the integral over $\varphi'$ is performed first, rendering the $x'$-integral trivial.

The result (6.36) is indeed the Mayer bond between platelet and needle: due to the set-up, an overlap must occur only at the origin. The first step function checks whether the origin is inside the platelet while the second step function checks whether the needle intersects the origin.

**3.5. The sphere-platelet Mayer bond.** The treatment of the sphere–platelet Mayer bond leads to the most involved geometry in the present ternary mixture. It turns out that for its exact deconvolution the deconvolution of the Mayer bond of the *two-dimensional* hard disk model is a prerequisite. It is known that the Rosenfeld functional gives only an approximate representation in this case. Still the DFT for hard disks is a reasonably accurate theory, see e.g. [149] for a recent study. In the present study we propose an approximate deconvolution that is on the same level of approximation as the 2d Rosenfeld case. Its advantage is that the resulting weight functions are single-particle quantities. We introduce the weight functions

$$\mathbf{w}_{\mathrm{v2}}^{\mathrm{SD}}(\mathbf{r},\mathbf{\Omega}) = \frac{4}{\pi}\frac{\mathbf{r}-(\mathbf{r}\cdot\mathbf{\Omega})\mathbf{\Omega}}{R}w_2^{\mathrm{S}}(\mathbf{r}), \tag{6.37}$$

$$w_2^{\mathrm{SD}}(\mathbf{r},\mathbf{\Omega}) = \frac{4}{\pi}\sqrt{1-(\mathbf{r}\cdot\mathbf{\Omega}/R)^2}\,w_2^{\mathrm{S}}(\mathbf{r}), \tag{6.38}$$

$$\mathbf{w}_{\mathrm{v1}}^{\mathrm{D}}(\mathbf{r},\mathbf{\Omega}) = \frac{\mathbf{r}}{R_{\mathrm{D}}}w_1^{\mathrm{D}}(\mathbf{r},\mathbf{\Omega}). \tag{6.39}$$

Eq. (6.37) describes a vector field tied to the surface of the sphere (with radius $R$). In contrast to the "radial hedgehog" of the classic vector weight function $\mathbf{w}_{\mathrm{v2}}^{\mathrm{S}}$, as given in Eq. (6.3), the direction of the vector field is radial with respect to the $\mathbf{\Omega}$ direction and its magnitude decreases towards either pole – a configuration one could refer to as a "cylindrical hedgehog". Note further that $w_2^{\mathrm{SD}} = |\mathbf{w}_{\mathrm{v2}}^{\mathrm{SD}}|$. The crown-like vector-field of Eq. (6.39) is the straightforward generalisation of the corresponding 2d hard disk weight function. These functions allow us to approximate $f_{\mathrm{SD}} \approx f_{\mathrm{SD}}^*$ with

$$\begin{aligned}-f_{\mathrm{SD}}^*(\mathbf{r},\mathbf{\Omega}) = {}& w_3^{\mathrm{S}}(\mathbf{r}) * w_0^{\mathrm{D}}(\mathbf{r},\mathbf{\Omega}) + w_1^{\mathrm{S}}(\mathbf{r}) * w_2^{\mathrm{D}}(\mathbf{r},\mathbf{\Omega}) \\ & + w_2^{\mathrm{SD}}(\mathbf{r},\mathbf{\Omega}) * w_1^{\mathrm{D}}(\mathbf{r},\mathbf{\Omega}) - \mathbf{w}_{\mathrm{v2}}^{\mathrm{SD}}(\mathbf{x},\mathbf{\Omega}) * \mathbf{w}_{\mathrm{v1}}^{\mathrm{D}}(\mathbf{r},\mathbf{\Omega}).\end{aligned} \tag{6.40}$$

where again the convolution implies a scalar product between vectors.

The deconvolution of the sphere–platelet Mayer bond consists of three parts. One is the arc that the rim of the platelet traces inside the sphere (Figure 5); secondly, the arc that the sphere traces on the platelet (Figure 6); thirdly, an additional contribution of the cusps where the two arcs meet.

We put the platelet into the $x$–$y$-plane with its centre at the origin. The sphere is located in the $y$–$z$-plane, see Fig 5, hence the coordinates are $\mathbf{r} = (0, r, z)$, $\mathbf{\Omega} = (0, 0, 1)$, $\mathbf{x} = (r'\sin\varphi', r'\cos\varphi', z')$.

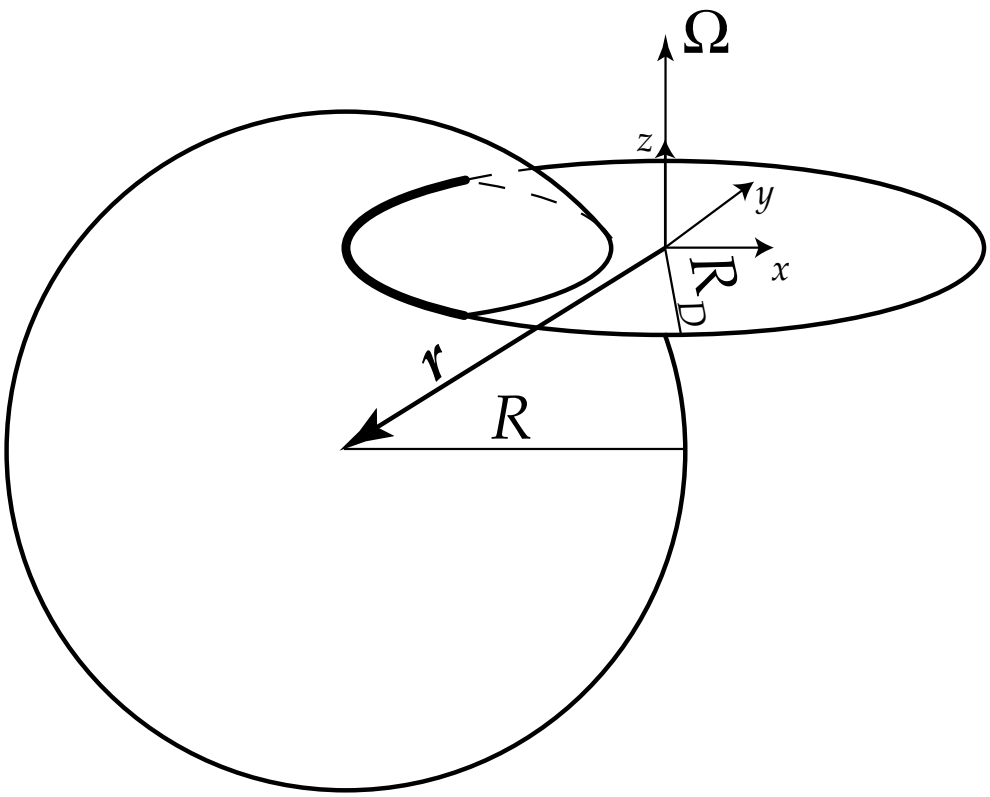


FIGURE 5. Setup for the calculation of the sphere–platelet Mayer bond. The platelet is located at the origin. The convolution $w_0^{\mathrm{D}} * w_3^{\mathrm{S}}$ is equal to the angle under which the arc shown in bold appears.

Explicitly, the relevant weight functions are

$$\mathbf{w}_{\mathrm{v2}}^{\mathrm{SD}}(\mathbf{r},\boldsymbol{\Omega}) = \frac{4}{\pi}\,\delta\left(R-|\mathbf{r}|\right)\frac{\mathbf{r}-(\mathbf{r}\cdot\boldsymbol{\Omega})\boldsymbol{\Omega}}{R} \text{ and} \tag{6.41}$$

$$\mathbf{w}_{\mathrm{v1}}^{\mathrm{D}}(\mathbf{r},\boldsymbol{\Omega}) = \frac{\mathbf{r}}{8R_{\mathrm{D}}}\,\delta\left(R_{\mathrm{D}}-|\mathbf{r}|\right)\,\delta\left(\mathbf{r}\cdot\boldsymbol{\Omega}\right), \tag{6.42}$$

and we obtain for the first part:

$$\begin{aligned}
&\int w_0^{\mathrm{D}}(\mathbf{x},\boldsymbol{\Omega}) w_3^{\mathrm{S}}(\mathbf{x}-\mathbf{r})\,\mathrm{d}^3x \\
&\quad= \frac{1}{2\pi R_{\mathrm{D}}}\int_0^{2\pi}\int_{-\infty}^{\infty}\int_0^{\infty}\delta\left(R_{\mathrm{D}}-\sqrt{r'^2+z'^2}\right)\,\delta\left(\mathbf{x}\cdot\boldsymbol{\Omega}\right) \\
&\qquad\times\Theta(R-|\mathbf{x}-\mathbf{r}|)\;r'\,\mathrm{d}r'\,\mathrm{d}z'\,\mathrm{d}\varphi' \qquad (6.43)\\
&\quad= \frac{1}{2\pi}\int_0^{2\pi}\Theta\Big(R-\sqrt{R_{\mathrm{D}}^2+r^2+z^2-rR_{\mathrm{D}}\cos\varphi'}\Big)\;\mathrm{d}\varphi' \qquad (6.44)
\end{aligned}$$

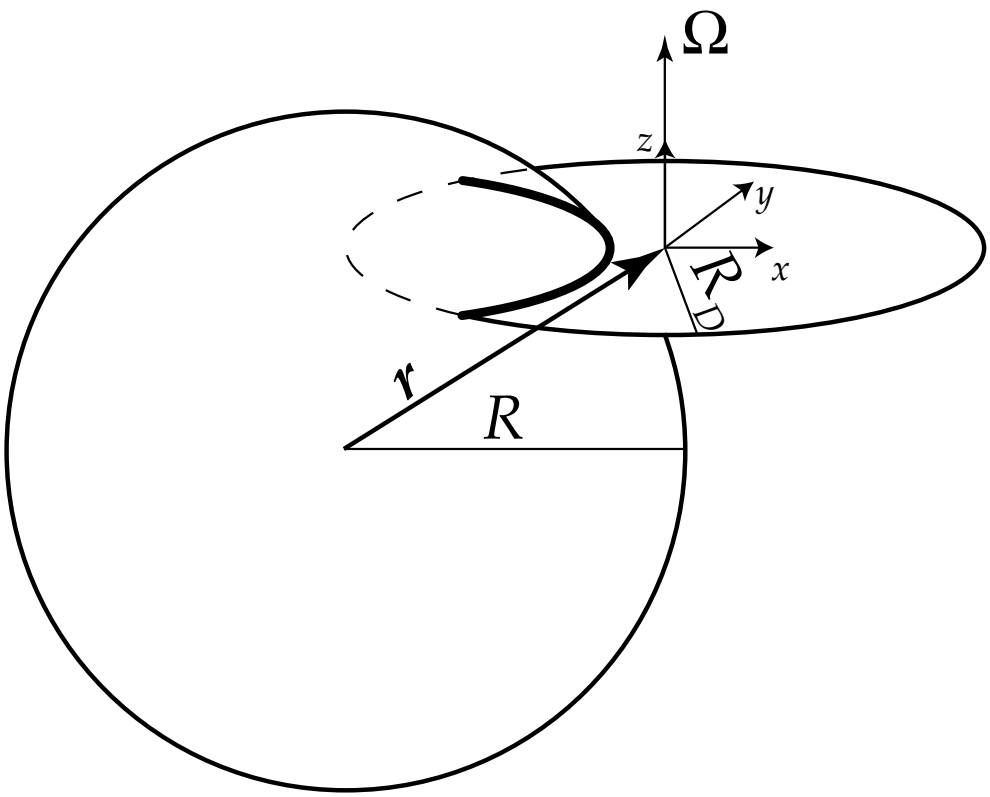


FIGURE 6. Setup for the calculation of the sphere–platelet Mayer bond. The platelet is located at the origin. The convolution $w_1^{\mathrm{S}} * w_2^{\mathrm{D}}$ is equal to the angle under which the arc shown in bold appears.

$$= \frac{1}{\pi} \arccos\Big(\frac{r^2 + R_{\mathrm{D}}^2 + z^2 - R^2}{2rR_{\mathrm{D}}}\Big) \Theta\big(2rR_{\mathrm{D}} - \big|r^2 + R_{\mathrm{D}}^2 + z^2 - R^2\big|\big) \qquad (6.45)$$

We take into account that $R^2 - z^2$ is the squared radius of the circle that the platelet cuts out of the sphere and note that by the cosine theorem, this is equal (up to a factor of $2\pi$) to the length of the arc which the rim of the disc traces inside the sphere, see Eq. (6.14).

For the second part:

$$\begin{aligned}
&\int w_1^{\mathrm{S}}(\mathbf{x}) w_2^{\mathrm{D}}(\mathbf{x}-\mathbf{r},\boldsymbol{\Omega})\,\mathrm{d}^3x \\
&\quad= \frac{1}{4\pi R}\int_{-\infty}^{\infty}\int_{0}^{2\pi}\int_{0}^{\infty} \delta\left(R-\sqrt{r'^2+z'^2}\right) \\
&\qquad\times 2\Theta\Big(R_{\mathrm{D}}-\sqrt{r^2+r'^2+(z'-z)^2-2rr'\cos\varphi'}\Big) \\
&\qquad\times\ \delta\left(z'-z\right)\ r'\,\mathrm{d}r'\,\mathrm{d}\varphi'\,\mathrm{d}z' \qquad (6.46)\\
&\quad= \frac{1}{2\pi R}\iint \delta\left(R-\sqrt{r'^2+z^2}\right)\Theta\Big(R_{\mathrm{D}}-\sqrt{r^2+r'^2-2rr'\cos\varphi'}\Big)\,r'\,\mathrm{d}r'\,\mathrm{d}\varphi' \qquad (6.47)\\
&\quad= \frac{1}{2\pi}\int_{0}^{2\pi}\Theta(R-|z|)\,\Theta\left(R_{\mathrm{D}}-\sqrt{r^2+R^2-z^2-2r\sqrt{R^2-z^2}\cos\varphi'}\right)\mathrm{d}\varphi' \qquad (6.48)\\
&\quad= \frac{1}{\pi}\arccos\Big(\frac{r^2+R^2-z^2-R_{\mathrm{D}}^2}{2r\sqrt{R^2-z^2}}\Big)\Theta\Big(2r\sqrt{R^2-z^2}-\left|r^2+R^2-z^2-R_{\mathrm{D}}^2\right|\Big) \qquad (6.49)
\end{aligned}$$

This is indeed the length of the arc that the sphere traces on the platelet divided by $2\pi$, see Eq. (6.14).

The remaining term to recover the approximate sphere–platelet Mayer bond is:

$$\begin{aligned}
&\int w_2^{\mathrm{SD}}(\mathbf{x}) w_1^{\mathrm{D}}(\mathbf{x}-\mathbf{r}) - \mathbf{w}_{\mathrm{v}2}^{\mathrm{SD}}(\mathbf{x})\mathbf{w}_{\mathrm{v}1}^{\mathrm{D}}(\mathbf{x}-\mathbf{r})\,\mathrm{d}^3x \\
&\quad= \frac{1}{2\pi}\int\Bigg(\delta\left(R-|\mathbf{x}|\right)\,\delta\left(R_{\mathrm{D}}-|\mathbf{x}-\mathbf{r}|\right)\,\delta\left(\boldsymbol{\Omega}\cdot(\mathbf{x}-\mathbf{r})\right)\frac{\mathbf{x}\cdot\boldsymbol{\Omega}}{|\mathbf{x}|} \\
&\qquad-\ \delta\left(R-|\mathbf{x}|\right)\,\delta\left(R_{\mathrm{D}}-|\mathbf{x}-\mathbf{r}|\right)\,\delta\left(\boldsymbol{\Omega}\cdot(\mathbf{x}-\mathbf{r})\right) \qquad (6.50)\\
&\qquad\times\frac{\mathbf{x}-(\mathbf{x}\cdot\boldsymbol{\Omega})\boldsymbol{\Omega}}{|\mathbf{x}|}\cdot\frac{\mathbf{x}-\mathbf{r}}{R_{\mathrm{D}}}\Bigg)\,\mathrm{d}^3x
\end{aligned}$$

$$= \frac{1}{2\pi} \int_0^{2\pi} \int_0^{\infty} \int_{-\infty}^{\infty} \delta\left(R - \sqrt{r'^2 + z'^2}\right) \times \delta\left(R_{\mathrm{D}} - \sqrt{r^2 + r'^2 - 2rr'\cos\varphi' + (z'-z)^2}\right) \times \delta(z'-z) \left( \frac{r'}{\sqrt{r'^2+z'^2}} - \frac{\begin{pmatrix} r'\sin\varphi' \\ r'\cos\varphi' \\ 0 \end{pmatrix} \cdot \begin{pmatrix} r'\sin\varphi' \\ r'\cos\varphi' - r \\ z'-z \end{pmatrix}}{R_{\mathrm{D}}\sqrt{r'^2+z'^2}} \right) \mathrm{d}z'\, r'\, \mathrm{d}r'\, \mathrm{d}\varphi' \tag{6.51}$$

$$= \frac{1}{2\pi} \int_0^{2\pi} \int_0^{\infty} \delta\left(R - \sqrt{r'^2+z^2}\right) \delta\left(R_{\mathrm{D}} - \sqrt{r^2 + r'^2 - 2rr'\cos\varphi'}\right) \times \left( \frac{r'}{\sqrt{r'^2+z^2}} - \frac{r'^2 - rr'\cos\varphi'}{R_{\mathrm{D}}\sqrt{r'^2+z^2}} \right) r'\, \mathrm{d}r'\, \mathrm{d}\varphi' \tag{6.52}$$

$$= \frac{R}{2\pi} \int_0^{2\pi} \delta\left(R_{\mathrm{D}} - \sqrt{r^2 + R^2 - z^2 - 2r\sqrt{R^2-z^2}\cos\varphi'}\right) \times \frac{\sqrt{R^2-z^2}}{R} \left(1 - \frac{\sqrt{R^2-z^2} - r\cos\varphi'}{R_{\mathrm{D}}}\right) \Theta(R - |z|)\, \mathrm{d}\varphi' \tag{6.53}$$

$$= \frac{1}{\pi} \Theta\Big(2r\sqrt{R^2-z^2} - |r^2 + R^2 - z^2 - R_{\mathrm{D}}^2|\Big)\, \Theta(R-|z|) \times \frac{R^2 - (\sqrt{R^2-z^2} - R_{\mathrm{D}})^2}{\sqrt{4r^2(R^2-z^2) - (r^2+R^2-z^2-R_{\mathrm{D}}^2)^2}} \tag{6.54}$$

Considering again that $R^2 - z^2$ is the squared radius of the circle that the plane of the platelet cuts out of the sphere, we recover the Rosenfeld (approximate) Mayer bond of hard disks in two dimensions, see Eq. (6.16).

## 4. Weighted densities

The weight functions are used to build weighted densities via convolutions with the bare density profiles. Again starting with spheres and needles, the procedures are

$$n_\nu^{\mathrm{S}}(\mathbf{r}) = w_\nu^{\mathrm{S}}(\mathbf{r}) * \rho_{\mathrm{S}}(\mathbf{r}), \quad \nu = 0,1,2,3, \tag{6.55}$$

$$\mathbf{n}_{\mathrm{v}\nu}^{\mathrm{S}}(\mathbf{r}) = \mathbf{w}_{\mathrm{v}\nu}^{\mathrm{S}}(\mathbf{r}) * \rho_{\mathrm{S}}(\mathbf{r}), \quad \nu = 1,2, \tag{6.56}$$

$$n_\nu^{\mathrm{N}}(\mathbf{r},\boldsymbol{\Omega}) = w_\nu^{\mathrm{N}}(\mathbf{r},\boldsymbol{\Omega}) * \rho_{\mathrm{N}}(\mathbf{r},\boldsymbol{\Omega}), \quad \nu = 0,1, \tag{6.57}$$

$$n_2^{\mathrm{SN}}(\mathbf{r},\boldsymbol{\Omega}) = w_2^{\mathrm{SN}}(\mathbf{r},\boldsymbol{\Omega}) * \rho_{\mathrm{S}}(\mathbf{r}). \tag{6.58}$$

To treat the degrees of freedom of the platelets, we introduce corresponding weighted densities as

$$n_\nu^{\mathrm{D}}(\mathbf{r},\mathbf{\Omega}) = w_\nu^{\mathrm{D}}(\mathbf{r},\mathbf{\Omega}) * \rho_{\mathrm{D}}(\mathbf{r},\mathbf{\Omega}), \quad \nu = 0,1,2, \tag{6.59}$$

$$n_1^{\mathrm{DD}}(\mathbf{r},\mathbf{\Omega}') = \frac{1}{4\pi}\int w_1^{\mathrm{DD}}(\mathbf{r},\mathbf{\Omega};\mathbf{\Omega}') * \rho_{\mathrm{D}}(\mathbf{r},\mathbf{\Omega})\,\mathrm{d}^2\Omega. \tag{6.60}$$

Furthermore there is a mixed weighted density,

$$n_2^{\mathrm{DN}}(\mathbf{r},\mathbf{\Omega}') = \frac{1}{4\pi}\int w_2^{\mathrm{DN}}(\mathbf{r},\mathbf{\Omega};\mathbf{\Omega}') * \rho_{\mathrm{D}}(\mathbf{r},\mathbf{\Omega})\,\mathrm{d}^2\Omega, \tag{6.61}$$

and the vectorial weighted densities,

$$\mathbf{n}_{\mathrm{v}1}^{\mathrm{D}}(\mathbf{r},\mathbf{\Omega}) = \mathbf{w}_{\mathrm{v}1}^{\mathrm{D}}(\mathbf{r},\mathbf{\Omega}) * \rho_{\mathrm{D}}(\mathbf{r},\mathbf{\Omega}), \tag{6.62}$$

$$\mathbf{n}_{\mathrm{v}2}^{\mathrm{SD}}(\mathbf{r},\mathbf{\Omega}) = \mathbf{w}_{\mathrm{v}2}^{\mathrm{SD}}(\mathbf{r},\mathbf{\Omega}) * \rho_{\mathrm{S}}(\mathbf{r}). \tag{6.63}$$

## 5. Free energy functional

Following Ref. [105] we express the excess Helmholtz free energy functional for particles with rotational degrees of freedom not only as a spatial integral (as was proposed in Refs. [101,122]), but also as an integral over the director space,

$$\beta F_{\mathrm{exc}} = \frac{1}{4\pi}\iint \Phi(\{n_\nu^i\})\,\mathrm{d}^3r\,\mathrm{d}^2\Omega, \tag{6.64}$$

where the (reduced) free energy density, $\Phi$, is a function of the set of weighted densities, $\{n_\nu^i\}$, where $i$ labels the species and $\mu$ labels the type of weight function.

For hard spheres $\Phi = \Phi_{\mathrm{S}}$ where

$$\begin{aligned}\Phi_{\mathrm{S}} = &- n_0^{\mathrm{S}}\ln(1-n_3^{\mathrm{S}}) + \frac{n_1^{\mathrm{S}}n_2^{\mathrm{S}} - \mathbf{n}_{\mathrm{v}1}^{\mathrm{S}}\cdot\mathbf{n}_{\mathrm{v}2}^{\mathrm{S}}}{1-n_3^{\mathrm{S}}} \\ &+ \frac{(n_2^{\mathrm{S}})^3/3 - n_2^{\mathrm{S}}\mathbf{n}_{\mathrm{v}2}^{\mathrm{S}}\cdot\mathbf{n}_{\mathrm{v}2}^{\mathrm{S}}}{8\pi(1-n_3^{\mathrm{S}})^2},\end{aligned} \tag{6.65}$$

is the original Rosenfeld form [96] that yields, for bulk fluids, the (reduced) free energy density as obtained by the Percus-Yevick compressibility (or scaled-particle) route. Improved versions that feature exact dimensional crossover have been developed [98, 100]. In Ref. [151] a version is given that is adopted to the Carnahan-Starling equation of state.

For binary mixtures of spheres and needles the reduced free energy density is $\Phi = \Phi_{\mathrm{S}} + \Phi_{\mathrm{SN}}$, where $\Phi_{\mathrm{S}}$ is given in (6.65), and $\Phi_{\mathrm{SN}}$ describes the effect of needle-sphere interactions [105], given as

$$\Phi_{\mathrm{SN}} = -n_0^{\mathrm{N}}\ln(1-n_3^{\mathrm{S}}) + \frac{n_1^{\mathrm{N}}n_2^{\mathrm{SN}}}{1-n_3^{\mathrm{S}}}. \tag{6.66}$$

The free energy for bulk fluid states is the same as that obtained from a thermodynamic (free volume like) perturbation theory [86], that results in a fluid-fluid demixing binodal that compares well with results from simulations.

For a system of pure platelets $\Phi = \Phi_{\rm D}$, with

$$\Phi_{\rm D} = n_1^{\rm DD} n_2^{\rm D} + A(n_2^{\rm D})^3. \tag{6.67}$$

where according to Rosenfeld $A = 1/(24\pi) = 0.01326$. Scaled-particle theory [117] gives a slightly different constant, $A = \pi/192 = 0.01636$. Eq. (6.67) is the simplest form of a free energy density that features the correct second virial level and a similar free energy for bulk isotropic fluid states as scaled-particle theory, where the third order contribution to the excess free energy density (per volume) is expressed in terms of fundamental measures as $(\xi_1^{\rm D}\xi_2^{\rm D})^2\rho_{\rm D}^3/6$.

The free energy density of a binary platelet–needle mixture is $\Phi = \Phi_{\rm D} + \Phi_{\rm DN}$, with only the simple second-order contribution

$$\Phi_{\rm DN} = n_2^{\rm DN} n_1^{\rm N}. \tag{6.68}$$

For binary sphere-platelet mixtures we obtain $\Phi = \Phi_{\rm S} + \Phi_{\rm SD}$ with

$$\begin{aligned}\Phi_{\rm SD} = &- n_0^{\rm D}\ln(1-n_3^{\rm S}) \\ &+ \frac{n_1^{\rm DD}n_2^{\rm D} + n_1^{\rm S}n_2^{\rm D} + n_2^{\rm S}n_1^{\rm D} + \mathbf{n}_{\rm v1}^{\rm SD}\cdot\mathbf{n}_{\rm v2}^{\rm D}}{1-n_3^{\rm S}} \\ &+ \frac{(n_2^{\rm S}+n_2^{\rm D})^3/3 - \mathbf{n}_{\rm v2}^{\rm S}\cdot\mathbf{n}_{\rm v2}^{\rm S}(n_2^{\rm S}+n_2^{\rm D})}{8\pi(1-n_3^{\rm S})^2}.\end{aligned} \tag{6.69}$$

Finally for ternary sphere-platelet-needle mixtures the free energy density is

$$\Phi = \Phi_{\rm S} + \Phi_{\rm SN} + \Phi_{\rm SD} + \frac{n_1^{\rm N} n_2^{\rm DN}}{1-n_3^{\rm S}}. \tag{6.70}$$

The terms that couple spheres and needles are hence the same as in Ref. [105] and we have restricted ourselves to the case of vanishingly thin needles throughout.

## 6. Planar geometry

In many practical situations of inhomogeneous fluids one is faced with inhomogeneities that depend only on a single (Cartesian) coordinate, say the $z$-axis, while being translationally invariant in the two remaining directions. A smooth planar wall, where the fluid density profile(s) only depend on the perpendicular distance from the wall is a primary example. For rotators an additional simplification constitutes (cylindrical) rotational symmetry around the $z$-axis. Hence such problems are characterised solely by $z$, and the tilt angle $\vartheta$ between the particle orientation and the $z$-axis. We assume $\vartheta \in [0, \pi]$. We give in the following explicit expressions for (reduced) weight functions appropriate for efficient numerical treatment of such situations.

The weighted densities, Eqs. (6.59)-(6.63), can then be written as

$$n_\nu^{\mathrm{D}}(z,\vartheta) = \int_{-\infty}^{\infty} w_\nu^{\mathrm{D}}(z'-z,\vartheta)\rho_{\mathrm{D}}(z',\vartheta)\,\mathrm{d}z', \quad \nu = 0,1,2, \tag{6.71}$$

$$n_1^{\mathrm{DD}}(z,\vartheta') = \frac{1}{2}\int_{-\infty}^{\infty}\int_{0}^{\pi} w_1^{\mathrm{DD}}(z'-z,\vartheta;\vartheta')\rho_{\mathrm{D}}(z',\vartheta)\sin\vartheta\,\mathrm{d}\vartheta\,\mathrm{d}z', \tag{6.72}$$

$$n_2^{\mathrm{DN}}(z,\vartheta') = \frac{1}{2}\int_{-\infty}^{\infty}\int_{0}^{\pi} w_2^{\mathrm{DN}}(z'-z,\vartheta;\vartheta')\rho_{\mathrm{D}}(z',\vartheta)\sin\vartheta\,\mathrm{d}\vartheta\,\mathrm{d}z', \tag{6.73}$$

$$\mathbf{n}_{\mathrm{v1}}^{\mathrm{D}}(z,\vartheta) = \int_{-\infty}^{\infty} \mathbf{w}_{\mathrm{v1}}^{\mathrm{D}}(z'-z,\vartheta)\rho_{\mathrm{D}}(z',\vartheta)\,\mathrm{d}z', \tag{6.74}$$

$$\mathbf{n}_{\mathrm{v2}}^{\mathrm{SD}}(z,\vartheta) = \int_{-\infty}^{\infty} \mathbf{w}_{\mathrm{v2}}^{\mathrm{SD}}(z'-z,\vartheta)\rho_{\mathrm{S}}(z')\,\mathrm{d}z'. \tag{6.75}$$

The effective one-dimensional weight functions are obtained by integrating over the lateral coordinates:

$$w_\nu^{\mathrm{D}}(z,\vartheta) = \iint w_\nu^{\mathrm{D}}(\mathbf{r},\boldsymbol{\Omega})\;\mathrm{d}x\,\mathrm{d}y \qquad \nu = 0,1,2 \tag{6.76}$$

where $\mathbf{r} = (x,y,z)$ and $\boldsymbol{\Omega} = (\vartheta,\varphi)$.

They turn out to be:

$$w_2^{\mathrm{D}}(z,\vartheta) = \frac{4\sqrt{R_{\mathrm{D}}^2 - z^2/\sin^2\vartheta}}{\sin\vartheta}\Theta(R_{\mathrm{D}}\sin\vartheta - |z|) \tag{6.77}$$

$$w_1^{\mathrm{D}}(z,\vartheta) = \frac{R_{\mathrm{D}}\Theta(R_{\mathrm{D}}\sin\vartheta - |z|)}{4\sqrt{R_{\mathrm{D}}^2\sin\vartheta^2 - z^2}} \tag{6.78}$$

$$w_0^{\mathrm{D}}(z,\vartheta) = \frac{\Theta(R_{\mathrm{D}}\sin\vartheta - |z|)}{\pi\sqrt{R_{\mathrm{D}}^2\sin\vartheta^2 - z^2}} \tag{6.79}$$

Note that these are not piecewise constant functions of $z$, and hence differ from Eqs. (15) and (16) in Ref. [150].

For the vector and mixed weight functions, we define

$$\mathbf{w}_{\mathrm{v2}}^{\mathrm{SD}}(z,\vartheta) = \frac{1}{2\pi}\iiint \mathbf{w}_{\mathrm{v2}}^{\mathrm{SD}}(\mathbf{r},\mathbf{\Omega})\,\mathrm{d}\varphi\,\mathrm{d}x\,\mathrm{d}y \tag{6.80}$$

$$\mathbf{w}_{\mathrm{v1}}^{\mathrm{D}}(z,\vartheta) = \frac{1}{2\pi}\iiint \mathbf{w}_{\mathrm{v1}}^{\mathrm{D}}(\mathbf{r},\mathbf{\Omega})\,\mathrm{d}\varphi\,\mathrm{d}x\,\mathrm{d}y \tag{6.81}$$

$$w_2^{\mathrm{DN}}(z,\vartheta_{\mathrm{D}};\vartheta_{\mathrm{N}}) = \frac{1}{2\pi}\iiint w_2^{\mathrm{DN}}(\mathbf{r},\mathbf{\Omega}_{\mathrm{D}};\mathbf{\Omega}_{\mathrm{N}})\,\mathrm{d}\varphi_{\mathrm{D}}\,\mathrm{d}x\,\mathrm{d}y \tag{6.82}$$

$$w_1^{\mathrm{DD}}(z,\vartheta;\vartheta') = \frac{1}{2\pi}\iiint w_1^{\mathrm{DD}}(\mathbf{r},\mathbf{\Omega};\mathbf{\Omega}')\,\mathrm{d}\varphi\,\mathrm{d}x\,\mathrm{d}y \tag{6.83}$$

and obtain

$$\mathbf{w}_{\mathrm{v2}}^{\mathrm{SD}}(z,\vartheta) = \frac{8\pi}{R_{\mathrm{D}}} z\sin^2\vartheta\sqrt{R_{\mathrm{D}}^2 - z^2}\,\mathbf{e}_z \tag{6.84}$$

$$\mathbf{w}_{\mathrm{v1}}^{\mathrm{D}}(z,\vartheta) = \frac{z}{8R_{\mathrm{D}}\sin^2\vartheta}\sqrt{\frac{R_{\mathrm{D}}^2\sin^2\vartheta - z^2}{R_{\mathrm{D}}^2 - z^2}} \tag{6.85}$$

$$w_2^{\mathrm{DN}}(z,\vartheta_{\mathrm{D}};\vartheta_{\mathrm{N}}) = \frac{4\cot\vartheta_{\mathrm{D}}\cos\vartheta_{\mathrm{N}}\sqrt{R_{\mathrm{D}}^2 - z^2}}{R_{\mathrm{D}}^2 - z^2/\sin^2\vartheta_{\mathrm{D}}}\Theta(R_{\mathrm{D}}\sin\vartheta_{\mathrm{D}} - |z|) \tag{6.86}$$

$$\begin{aligned} w_2^{\mathrm{SD}}(z,\vartheta) = {} & \frac{2}{\pi^2}\Theta(R - |z|) \\ & \times \int_0^{2\pi} \sqrt{R^2 - \big((R^2 - z^2)\cos\varphi\sin\vartheta + z\cos\vartheta\big)^2}\,\mathrm{d}\varphi \end{aligned} \tag{6.87}$$

$$w_1^{\mathrm{DD}}(z,\vartheta;\vartheta') = \begin{cases} 0 & \text{if } p^2 < 0 \\ \frac{1}{2}\cos\vartheta' & \text{if } p^2\sin(\vartheta - \vartheta')\sin(\vartheta + \vartheta') > z^2\sin^2\vartheta' \\ \frac{1}{\pi p}\Big(\sqrt{(z^2 + p^2)\frac{\sin^2\vartheta'}{\sin^2\vartheta} - p^2} & \\ \quad + p|\cos\vartheta'|\arcsin\frac{p|\cot\vartheta'|}{\sqrt{z^2 + R_{\mathrm{D}}^2\cos^2\vartheta}}\Big) & \text{else,} \end{cases} \tag{6.88}$$

where $p = \sqrt{R_{\mathrm{D}}^2\sin^2\vartheta - z^2}$.

The integral in Eq. (6.87) has to be solved numerically.

## 7. Conclusions

In conclusion we have derived a geometry-based density functional theory for hard body mixtures of spheres, platelets and needles. Both the needles and the (circular) platelets possess vanishing thickness and hence constitute the simplest examples of prolate and oblate model particles, respectively. Our treatment of the mixture is based on the so-called deconvolution of the Mayer function into single-particle functions which vanish beyond the extent of the particle. The Mayer bonds are recovered upon convolution of the single-particle functions. In order to facilitate future applications, like wetting of planar walls or capillary

phenomena in planar slits, we have given explicit simplified expressions for the relevant quantities in planar geometry.

In a recent contribution Harnau and Dietrich propose and apply a DFT for binary platelet-sphere mixtures [150]. They obtain a platelet-sphere functional by starting from the rod-sphere functional of Refs. [105, 116], and in particular from the explicit expressions for the needle weight functions in planar and uniaxial geometry, Eqs. (22) and (23) in [116]. Modifying the definition of the relevant angle between the particle orientation and the $z$-axis they take the rod weight functions to play the role of platelet weight functions. The excess free energy functional that they obtain is linear in the platelet density, limiting the theory to small densities of platelets. Recall that for binary mixtures where one component (the depletant) is ideal, the absence of higher than linear order terms in the density distribution of this component is a good approximation. Examples are the above rod-sphere mixture and the Asakura-Oosawa model of colloid-polymer mixtures, where the polymers are described as non-interacting spheres. While in these cases the pure depletant system is an ideal gas, pure platelets constitute an interacting system. Hence higher than linear order terms in the platelet density should only be irrelevant at low platelet densities.

In the present work we have shown explicitly how our DFT for the sphere-platelet mixture reduces to the correct low-density limit. We have treated the full three-dimensional problem and have, up to a technical difficulty already present for two-dimensional hard disks, obtained the deconvolution of the sphere-platelet Mayer bond and hence the appropriate platelet weight functions. Projecting those to planar and uniaxial symmetry (appropriate for fluid states at a planar smooth wall, like those investigated in Ref. [150]) reveals that the expressions differ markedly from those for sphere-rod mixtures. This might come as no surprise given the fact that the genuine shapes of the particles are one of the building blocks of the geometry-based DFT. An immediate consequence is that the platelet weight functions we obtain also differ from the expressions used in Ref. [150].

Ref. [150] ignores disk-disk repulsion, a good approximation provided the disk density is low. In the DFT framework this is formally due to the lack terms of higher than linear order in the platelet density profile. From the dimensional analysis it is clear that there should also be third order terms. Higher order terms are absent as the platelets carry vanishing volume. In order to obtain the correct coefficients for the third order terms, three-body overlap configurations have to be examined. Even for pure hard spheres this was only solved a decade after the Rosenfeld's original publication, and its generalisation to binary mixtures of spheres is a mathematical tour de force.

Possible future applications of our theory include capillary and wetting phenomena, influence of gravity or other external fields, and the study of free interfaces between demixed (and possibly liquid crystalline) phases.

CHAPTER 7

# Summary and Outlook

In Part 1 of this work, we have used both Monte-Carlo computer simulations and Poisson-Boltzmann theory to study the segregation of a system of charged particles under the influence of an external field. In Chapter 2, the influence of gravitation upon a binary colloidal mixture has been considered. It turned out that in such a system, sedimentation is controlled by the ratio of particle mass to charge rather than by mass alone. Thus, the species with the lower mass-per-charge ratio will sediment on top, even if its mass is larger than that of the other species. We have shown that the extent of segregation depends on the individual mass-per-charge ratios. As long as these differ only slightly, our simulations show barometric height profiles for both species. The decay lengths of these profiles are determined by the mass-per-charge ratios. If, however, the mass-per-charge ratios are considerably different, we found that one of the components will form a layer on top of the other component.

It will be a challenging task to check these results in real-space experiments. In order to check the density profiles, a broad range of densities must be measured while distinguishing between the species. Moreover, the gravitational lengths can easily be on the order of a few centimetres. Thus, keeping the cell at equilibrium to prevent convections of the solvent will be difficult. If such experiments prove successful, possible applications such as demixing in a centrifuge should be researched.

The authors of [54] have generalised our theory to encompass more than two species and even polydisperse colloids. They report that for these systems, sedimentation is still controlled by the ratio of mass and charge. They have also used a better minimisation method to show that the density functional completely describes our simulation data.

In Chapter 3, we have shown that for a symmetric liquid in a capacitor, there exists a distinct transition between a localised and a delocalised ion distribution. Taking the average distance $\langle h \rangle$ of one species of ions from the oppositely charged capacitor plate as an order parameter, we have employed Poisson-Boltzmann theory to determine the divergence of $\langle h \rangle$ as a function of the voltage applied across the capacitor. This turns out to be logarithmic. We have confirmed both the ion density profiles and the divergence of the order parameter $\langle h \rangle$ by computer simulations.

It would be interesting to see whether this effect can be used in microfluidic switching devices.

From the theoretical point of view, a generalisation to asymmetric electrolytes is perhaps the most immediate problem to address. Moreover, it would be interesting to combine gravity and an electric field in one system and study their interplay. In particular, if one considers a large electric field, gravitation can be neglected, and sedimentation will be controlled by the particles' charge only. It will then be interesting to see how the transition from charge-per-mass to charge-only as the important parameter happens.

In Part 2 of this work, we have presented a density functional theory that draws upon the hard sphere DFT by Rosenfeld and generalises it to anisotropic particles. In particular, we have considered ternary mixtures of spheres, and rods and platelets of vanishing thickness; and binary mixtures of thin rods in the Onsager limit with spheres. We have calculated explicit expressions of the functional in simple geometries, thereby showing that the number of parameters for these geometries is small enough to allow for a free minimisation of the density functional. These expressions are also intended as a reference for future applications. For future research, a calculation of the bulk phase diagrams for rods in the Onsager limit and for a system of thin platelets would be an interesting starting point. Once the bulk behaviour has been established, one could turn to the investigation of inhomogeneous systems, e.g. near a hard wall.

We have shown that a systematic extension of fundamental measure functionals to different anisotropic particles is possible. However, it has also become clear that the complexity of the weight functions needed to recover the particle–particle Mayer bonds rises rapidly as the particle shapes deviate from the very simple: rods of vanishing thickness, and spheres. While a fundamental measure functional for anisotropic particles with finite volume would be highly desirable, both the theoretical formulation and the numerical calculations will certainly be very involved and thus pose a challenge to future researchers. Considering the success of geometry-based density functionals [152], an extension to charged systems is also very desirable. Indeed, progress has been made in the development of fundamental measure functionals for soft interactions [153–155]. However, potentials that contain attractions or are long-ranged seem to pose considerable problems for this formalism.

# Bibliography


[1] T. Graham, *Philosophical Transactions of the Royal Society of London* **151**, 183 (1861).
[2] H.-A. Kurzhals and H. Reuter, *Chemie Ingenieur Technik* **45**, 491 (1973).
[3] P. F. W. Strengers, editor, *Blut*, Spektrum, 1996.
[4] J. Perrin, *J. Physique Théorique et appliquée* **9**, 5 (1910).
[5] M. Heni, *Surface Induced Effects in Hard Sphere Systems*, Dissertation, Heinrich-Heine-Universität Düsseldorf, 2001.
[6] S. Herminghaus, *J. Phys.: Condensed Matter* **17**, S261 (2005), and references therein.
[7] P. Debye, *Physikalische Zeitschrift* **21**, 178 (1920).
[8] K. Autumn, Y. A. Liang, S. T. Hsieh, W. Zesch, W. P. Chan, T. W. Kenny, R. Fearing, and R. J. Full, *Nature* **405**, 681 (2000).
[9] B. V. Derjaguin and L. Landau, *Acta Physicochimica (URSS)* **14**, 633 (1941).
[10] E. J. Verwey and J. T. G. Overbeek, *Theory of the Stability of Lyophobic Colloids*, Elsevier, 1948.
[11] H. Löwen, *J. Phys.: Condensed Matter* **13**, R415 (2001).
[12] P.-G. de Gennes, *Nature* **412**, 385 (2001).
[13] K. Lin, J. C. Crocker, A. C. Zeri, and A. G. Yodh, *Phys. Rev. Lett.* **87**, 088301 (2001).
[14] K. Lin, J. C. Crocker, A. C. Zeri, and A. G. Yodh, *Phys. Rev. Lett.* **87**, 269902 (2001).
[15] D. Marvin and E. J. Wachtel, *Nature* **253**, 19 (1975).
[16] R. A. Crowther, *Nature* **286**, 440 (1980).
[17] M. A. Bates and D. Frenkel, *J. Chem. Phys.* **110**, 6553 (1999).
[18] M. A. Bates and D. Frenkel, *Phys. Rev. E* **62**, 5225 (2000).
[19] S. D. Zhang, P. A. Reynolds, and J. S. van Duijneveldt, *J. Chem. Phys.* **117**, 9947 (2002).
[20] S. D. Zhang, P. A. Reynolds, and J. S. van Duijneveldt, *Molecular Physics* **100**, 3041 (2002).
[21] L. Harnau and S. Dietrich, *Phys. Rev. E* **66**, 051702 (2002).
[22] L. Harnau, D. Rowan, and J.-P. Hansen, *J. Chem. Phys.* **117**, 11359 (2002).
[23] M. Bier, L. Harnau, and S. Dietrich, *Phys. Rev. E* **69**, 021506 (2004).
[24] D. van der Beek and H. N. W. Lekkerkerker, *Langmuir* **20**, 8582 (2004).
[25] D. van der Beek, T. Schilling, and H. N. W. Lekkerkerker, *J. Chem. Phys.* **121**, 5423 (2004).
[26] D. van der Beek and H. N. W. Lekkerkerker, *Europhys. Lett.* **61**, 702 (2003).
[27] I. Langmuir, *J. Chem. Phys.* **6**, 873 (1938).
[28] S. Meyer, P. Levitz, and A. Deville, *Journal of Physical Chemistry B* **105**, 9595 (2001).
[29] I. Bihannic, L. J. Michot, B. S. Lartiges, D. Vantelon, J. Labille, F. Thomas, J. Susini, M. Salome, and B. Fayard, *Langmuir* **17**, 4144 (2001).
[30] J. C. Williams, *Powder Technol.* **15**, 245 (1976).

[31] A. Rosato, K. J. Strandburg, F. Prinz, and R. H. Swendsen, *Phys. Rev. Lett.* **58**, 1038 (1987).
[32] T. Shinbrot and F. J. Muzzio, *Phys. Rev. Lett.* **81**, 4365 (1998).
[33] D. C. Hong, P. V. Quinn, and S. Luding, *Phys. Rev. Lett.* **86**, 3423 (2001).
[34] J. A. Both and D. C. Hong, *Phys. Rev. Lett.* **88**, 124301 (2002).
[35] A. P. J. Breu, H.-M. Ensner, C. A. Kruelle, and I. Rehberg, *Phys. Rev. Lett.* **90**, 014302 (2003).
[36] V. Lobaskin, A. Lyubartsev, and P. Linse, *Phys. Rev. E* **63**, 020401 (2001).
[37] A. Esztermann and H. Löwen, *Europhys. Lett.* **68**, 120 (2004).
[38] R. Piazza, T. Bellini, and V. Degiorgio, *Phys. Rev. Lett.* **71**, 4267 (1993).
[39] M. A. Rutgers, J. H. Dunsmuir, J. H. Xue, W. B. Russel, and P. M. Chaikin, *Phys. Rev. B* **53**, 5043 (1996).
[40] A. P. Philipse and G. H. Koenderink, *Adv. Coll. Interf. Sci.* **100**, 613 (2003).
[41] A. Einstein, *Annalen der Physik* **4. F. 17**, 549 (1905).
[42] A. Einstein, *Annalen der Physik* **4. F. 19**, 371 (1906).
[43] T. Biben and J.-P. Hansen, *J. Phys.: Condens. Matter* **6**, A345 (1994).
[44] J.-P. Simonin, *J. Phys. Chem.* **99**, 1577 (1995).
[45] H. Löwen, *J. Phys.: Condens. Matter* **10**, L479 (1998).
[46] G. Tellez and T. Biben, *Europhys. J. E* **2**, 137 (2000).
[47] R. van Roij, *J. Phys.: Condens. Matter* **15**, S3569 (2003).
[48] J. Lekner, *Physica A* **176**, 485 (1991).
[49] H. Walliser, *Phys. Rev. Lett.* **89**, 189603 (2002).
[50] A.-P. Hynninen, R. van Roij, and M. Dijkstra, *Europhys. Lett.* **65**, 719 (2004).
[51] C. P. Royall, M. E. Leunissen, and A. van Blaaderen, *J. Phys.: Condens. Matter* **15**, S3581 (2003).
[52] L. Bellier-Castella and H. Xu, *J. Phys.: Condens. Matter* **15**, 5417 (2003).
[53] S. E. Harding, A. J. Rowe, and J. C. Norton, editors, *Analytical Ultracentrifugation in Biochemistry and Polymer Science*, The Royal Society of Chemistry, Cambridge, 1992.
[54] J. Zwanikken and R. van Roij, The sediment of mixtures of charged colloids: segregation an inhomogeneous electric fields, to be published, 2005.
[55] G. Gouy, *J. Phys. (France)* **IX**, 457 (1910).
[56] D. L. Chapman, *Philos. Mag.* **25**, 475 (1913).
[57] V. A. Parsegian and D. Gingell, *Biophysical Journal* **12**, 1192 (1972).
[58] D. McCormack, S. L. Carnie, and D. Y. C. Chan, *Journal of Colloid and Interface Science* **169**, 177 (1995).
[59] J.-P. Hansen and H. Löwen, *Annual Reviews of Physical Chemistry* **51**, 209 (2000).
[60] R. R. Netz, *J. Phys.: Condens. Matter* **16**, S2353 (2004).
[61] A. A. Meier-Koll, C. C. Fleck, and H. H. von Grünberg, *J. Phys.: Condens. Matter* **16**, 6041 (2004).
[62] N. G. Green, A. Ramos, A. Gonzalez, H. Morgan, and A. Castellanos, *Phys. Rev. E* **61**, 4011 (2000).
[63] A. Gonzalez, A. Ramos, N. G. Green, A. Castellanos, and H. Morgan, *Phys. Rev. E* **61**, 4019 (2000).
[64] U. K. Sur, F. Marken, N. Rees, B. A. Coles, R. G. Compton, and R. Seager, *Journal of Electroanalytical Chemistry* **573**, 175 (2004).
[65] S. W. Chen, R. S. Ingram, M. J. Hostetler, J. J. Pietron, R. W. Murray, T. G. Schaaff, J. T. Khoury, M. M. Alvarez, and R. L. Whetten, *Science* **280**, 2098 (1998).
[66] B. B. Katemann and T. Schuhmann, *Electroanalysis* **14**, 22 (2002).

[67] M. Deserno and C. Holm, Cell model and Poisson-Boltzmann theory: A brief introduction, in *Electrostatic Effects in Soft Matter and Biophysics*, edited by C. Holm, P. Kékicheff, and R. Podgornik, volume 46 of *NATO Science Series*, Kluwer, 2001.
[68] D. Andelman, Electrostatic Properties of Membranes: The Poisson-Boltzmann Theory, in *Handbook of Biological Physics*, edited by R. Lipowsky and E. Sackmann, volume 1, chapter 12, Elsevier, 1995.
[69] S. L. Carnie and G. M. Torrie, *Advances in Chemical Physics* **56**, 141 (1984).
[70] T. O. White and J. P. Hansen, *J. Phys.: Condens. Matter* **14**, 7649 (2002).
[71] D. B. Lukatsky, S. A. Safran, A. W. C. Lau, and P. Pincus, *Europhys. Lett.* **58**, 785 (2002).
[72] G. Tellez and E. Trizac, *Phys. Rev. E* **68**, 061401 (2003).
[73] I. Rouzina and V. A. Bloomfield, *J. Phys. Chem.* **100**, 9977 (1996).
[74] J. F. Callan, A. P. da Silva, J. Ferguson, A. J. M. Huxley, and A. M. O'Brien, *Tetrahedron* **60**, 11125 (2004).
[75] J. Hua and Y. G. Wang, *Chem. Letters* **34**, 98 (2005).
[76] J. F. Dufreche, J. P. Simonin, and P. Turq, *J. Mol. Liquids* **79**, 137 (1999).
[77] J. F. Dufreche, O. Bernard, P. Turq, A. Mukherjee, and B. Bagchi, *Phys. Rev. Lett.* **88**, 095902 (2002).
[78] M. Rasa and A. P. Philipse, *Nature* **429**, 857 (2004).
[79] M. Adams, Z. Dogic, S. L. Keller, and S. Fraden, *Nature (London)* **393**, 349 (1998).
[80] G. A. Vliegenthart and H. N. W. Lekkerkerker, *J. Chem. Phys.* **111**, 4153 (1999).
[81] G. H. Koenderink, G. A. Vliegenthart, S. G. J. M. Kluijtmans, A. van Blaaderen, A. P. Philipse, and H. N. W. Lekkerkerker, *Langmuir* **15**, 4693 (1999).
[82] M. Elbaum, D. K. Fygenson, and A. Libchaber, *Phys. Rev. Lett.* **76**, 4078 (1996).
[83] D. K. Fygenson, M. Elbaum, B. Shraiman, and A. Libchaber, *Phys. Rev. E* **55**, 850 (1997).
[84] S. G. J. M. Kluijtmans, G. H. Koenderink, and A. P. Philipse, *Phys. Rev. E* **61**, 626 (2000).
[85] G. A. Vliegenthart, *Phase transitions of atomic fluids and colloidal suspensions*, Dissertation, Utrecht University, 1999.
[86] P. Bolhuis and D. Frenkel, *J. Chem. Phys.* **101**, 9869 (1994).
[87] S. Asakura and F. Oosawa, *J. Chem. Phys.* **22**, 1255 (1954).
[88] A. Vrij, *Pure and Appl. Chem.* **48**, 471 (1976).
[89] H. N. W. Lekkerkerker, W. C. K. Poon, P. N. Pusey, A. Stroobants, and P. B. Warren, *Europhys. Lett.* **20**, 559 (1992).
[90] K. Yaman, C. Jeppesen, and C. M. Marques, *Europhys. Lett.* **42**, 221 (1998).
[91] Y. Mao, M. E. Cates, and H. N. W. Lekkerkerker, *Phys. Rev. Lett.* **75**, 4548 (1995).
[92] Y. Mao, M. E. Cates, and H. N. W. Lekkerkerker, *J. Chem. Phys.* **106**, 3721 (1997).
[93] Z. Dogic, D. Frenkel, and S. Fraden, *Phys. Rev. E* **62**, 3925 (2000).
[94] R. Evans, *Adv. Phys.* **28**, 143 (1979).
[95] R. Evans, Density Functionals in the Theory of Nonuniform Fluids, in *Fundamentals of Inhomogeneous Fluids*, edited by D. Henderson, chapter 3, p. 85, Dekker, New York, 1992.
[96] Y. Rosenfeld, *Phys. Rev. Lett.* **63**, 980 (1989).
[97] Y. Rosenfeld, M. Schmidt, H. Löwen, and P. Tarazona, *J. Phys. Cond. Matter* **8**, L577 (1996).

[98] Y. Rosenfeld, M. Schmidt, H. Löwen, and P. Tarazona, *Phys. Rev. E* **55**, 4245 (1997).
[99] P. Tarazona and Y. Rosenfeld, *Phys. Rev. E* **55**, R4873 (1997).
[100] P. Tarazona, *Phys. Rev. Lett.* **84**, 694 (2000).
[101] Y. Rosenfeld, *Phys. Rev. E* **50**, R3318 (1994).
[102] A. Chamoux and A. Perera, *J. Chem. Phys.* **104**, 1493 (1996).
[103] A. Chamoux and A. Perera, *Phys. Rev. E* **58**, 1933 (1998).
[104] A. Chamoux and A. Perera, *Mol. Phys.* **93**, 649 (1998).
[105] M. Schmidt, *Phys. Rev. E* **63**, 050201(R) (2001).
[106] M. Schmidt and C. von Ferber, *Phys. Rev. E* **64**, 051115 (2001).
[107] M. Schmidt and A. R. Denton, *Phys. Rev. E* **65**, 021508 (2002).
[108] R. Roth, R. van Roij, D. Andrienko, K. R. Mecke, and S. Dietrich, *Phys. Rev. Lett.* **89**, 088301 (2002).
[109] K. Shundyak and R. van Roij, *J. Phys.: Condens. Matter* **13**, 4789 (2001).
[110] M. E. Fisher and B. Widom, *J. Chem. Phys.* **50**, 3756 (1969).
[111] R. Evans, J. R. Henderson, D. C. Hoyle, A. O. Parry, and Z. A. Sabeur, *Mol. Phys.* **80**, 755 (1993).
[112] R. Evans, R. J. F. Leote de Carvalho, J. R. Henderson, and D. C. Hoyle, *J. Chem. Phys.* **100**, 591 (1994).
[113] M. Dijkstra and R. Evans, *J. Chem. Phys.* **112**, 1449 (2000).
[114] J. M. Brader, M. Dijkstra, and R. Evans, *Phys. Rev. E* **63**, 041405 (2001).
[115] J. M. Brader, R. Evans, M. Schmidt, and H. Löwen, *J. Phys.: Condensed Matter* **14**, L1 (2002).
[116] J. M. Brader, A. Esztermann, and M. Schmidt, *Phys. Rev. E* **66**, 031401 (2002).
[117] J. A. Barker and D. Henderson, *Rev. Mod. Phys.* **48**, 587 (1976).
[118] R. van Roij, M. Dijkstra, and R. Evans, *Europhys. Lett.* **49**, 350 (2000).
[119] A. J. Archer and R. Evans, *Phys. Rev. E* **64**, 041501 (2001).
[120] G. H. Koenderink, D. G. A. L. Aarts, V. W. A. de Villeneuve, A. P. Philipse, R. Tuinier, and H. N. W. Lekkerkerker, *Biomacromolecules* **4**, 129 (2003).
[121] L. Helden, R. Roth, G. H. Koenderink, P. Leiderer, and C. Bechinger, *Phys. Rev. Lett.* **90**, 048301 (2003).
[122] Y. Rosenfeld, *Mol. Phys.* **86**, 637 (1995).
[123] P. G. Bolhuis, J. M. Brader, and M. Schmidt, *J. Phys.: Condensed Matter* **48**, S3421 (2003).
[124] R. Roth, J. M. Brader, and M. Schmidt, *Europhys. Lett.* **63**, 549 (2003).
[125] R. Roth, *J. Phys.: Condensed Matter* **15**, S277 (2003).
[126] Y. X. Yu and J. Wu, *J. Chem. Phys.* **117**, 2368 (2002).
[127] P. Bryk, *Phys. Rev. E* **68**, 062501 (2004).
[128] K. R. Mecke, unpublished.
[129] L. Onsager, *Ann. N. Y. Acad. Sci.* **51**, 627 (1949).
[130] K. Shundyak and R. van Roij, *Phys. Rev. Lett.* **88**, 205501 (2002).
[131] K. Shundyak and R. van Roij, *Phys. Rev. E* **68**, 061703 (2003).
[132] G. Cinacchi and F. Schmid, *J. Phys.: Condensed Matter* **14**, 12223 (2002).
[133] H. Löwen, *Phys. Rev. E* **50**, 2821 (1994).
[134] M. Dijkstra, J. P. Hansen, and P. A. Madden, *Phys. Rev. Lett.* **51**, 5891 (1995).
[135] M. Dijkstra, J. P. Hansen, and P. A. Madden, *Phys. Rev. E* **55**, 3044 (1997).
[136] D. van der Beek, A. V. Petukhov, S. M. Oversteegen, G. J. Vroege, and H. N. W. Lekkerkerker, *Eur. Phys. J. E* **16**, 253 (2005).
[137] S. M. Oversteegen, J. G. E. J. Wijnhoven, and H. N. W. Lekkerkerker, *J. Phys. Chem. B* **108**, 18158 (2004).
[138] T. G. Mason, *Phys. Rev. E* **66**, 060402(R) (2002).

[139] L. Harnau and S. Dietrich, *Phys. Rev. E* **65**, 021505 (2002).
[140] L. Harnau, D. Costa, and J. P. Hansen, *Europhys. Lett.* **53**, 729 (2001).
[141] L. Harnau, F. Penna, and S. Dietrich, *Phys. Rev. E* **70**, 021505 (2004).
[142] S. M. Oversteegen and H. N. W. Lekkerkerker, *J. Chem. Phys.* **120**, 2470 (2004).
[143] S. M. Oversteegen and H. N. W. Lekkerkerker, *Physica A* **341**, 23 (2004).
[144] L. Harnau and S. Dietrich, *Phys. Rev. E* **69**, 051501 (2004).
[145] H. H. Wensink and H. N. W. Lekkerkerker, *Europhys. Lett.* **66**, 125 (2004).
[146] A. Esztermann and M. Schmidt, *Phys. Rev. E* **70**, 022501 (2004).
[147] M. Schmidt and J. M. Brader, *J. Chem. Phys.* **119**, 3495 (2003).
[148] M. Schmidt and M. Dijkstra, *J. Chem. Phys.* **121**, 12067 (2004).
[149] L. L. Rasmussen and D. W. Oxtoby, *J. Phys.: Condensed Matter* **14**, 12021 (2002).
[150] L. Harnau and S. Dietrich, *Phys. Rev. E* **71**, 011504 (2004).
[151] R. Roth, R. Evans, A. Lang, and G. Kahl, *J. Phys.: Condensed Matter* **14**, 12063 (2002).
[152] M. Schmidt, *Geometry-based density-functional theory: Construction and applications to soft matter*, Habilitation thesis, Heinrich-Heine-Universität Düsseldorf, 2004.
[153] M. Schmidt, *Phys. Rev. E* **60**, R6291 (1999).
[154] M. Schmidt, *Phys. Rev. E* **62**, 4976 (2000).
[155] M. Sweatman, *J. Phys.: Condensed Matter* **14**, 11921 (2002).

## Acknowledgement

I would like to express my gratitude to Hartmut Löwen and Matthias Schmidt for providing support, encouragement, and the opportunity to work with them.

Thanks to Joseph M. Brader and the ThPhy2 group Now&Then: Elshad Allahyarov, Ronald Blaak, Joachim Dzubiella, Christian von Ferber, Vladimir Froltsov, Ingo Götze, Martin Heni, Norman Hoffmann, Arben Jusufi, Heike Kaminski, Cord Kielhorn, Raina Kirchhoff, Martin Konieczny, Christos Likos, Christian Mayer, Rene Messina, Dagmar Petry, Ralf Pierre, Eckhard Rebhan, Hendrik Reich, Martin Rex, Federica Lo Verso, Rik Wensink, Paul Wessels, Karin Wildhagen, and Adam Wysocki.

Thanks to Holger M. "600 m/h" Harreis and Christina Harreis; and to Jan Feller and Marja Kokkonen: *Paljon kiitoksia juhannusjuhlista!*

I gratefully acknowledge financial support from the *Deutsche Forschungsgemeinschaft*.

Very special thanks go to my parents and my brother for being there.